# PHASE BEHAVIOR OF HYDROCARBON FLUIDS IN SHALE RESERVOIRS:

# EFFECT OF THE PRESENCE OF KEROGEN AND CONFINEMENT

by

Manas Pathak

A dissertation submitted to the faculty of
The University of Utah
in partial fulfillment of the requirements for the degree of

Doctor of Philosophy

Department of Chemical Engineering

The University of Utah

May 2017

**The University of Utah Graduate School**

# STATEMENT OF DISSERTATION APPROVAL

The dissertation of **Manas Pathak**

has been approved by the following supervisory committee members:

| | | |
|---|---|---|
| **Milind Deo** | , Chair | **12/09/16** Date Approved |
| **John McLennan** | , Member | **12/12/16** Date Approved |
| **Eric Eddings** | , Member | **12/15/16** Date Approved |
| **Edward Trujillo** | , Member | **12/12/16** Date Approved |
| **Raymond Levey** | , Member | **12/09/16** Date Approved |
| **Jonathan Craig** | , Member | **12/21/16** Date Approved |
| **Ger Van Graas** | , Member | **01/03/17** Date Approved |

and by **Milind Deo** , Chair/Dean of

the Department/College/School of **Chemical Engineering**

and by David B. Kieda, Dean of The Graduate School.

## ABSTRACT

Shale plays have revolutionized oil and gas production in the United States. In the last decade, many shale gas and liquid plays have been explored and developed in the US and elsewhere. Prospective shales consist of a complex organic component known as kerogen which is a precursor to oil and gas. Shales have pores with dimensions in the range of nanometers in the organic and inorganic constituents. The presence of organic matter and nanometer pores affect the thermodynamic properties of fluids in these rocks. A hypothesis has been proposed and proved through modeling and experiments to account for the influence of kerogen on thermodynamic properties of hydrocarbon fluids. Kerogen preferentially absorbs hydrocarbons and subsequently swells in volume. This splits oil in liquid-rich shale plays into two phases – a retained phase and a free phase, both of which remain in equilibrium. The retained and free phases together form in-situ oil; equilibrium of in-situ oil with gas was studied to investigate the effect of kerogen on saturation pressures of oils in shales. Results indicate a bubble point suppression between ~ 4150 kPa and ~ 16350 kPa from an original value of 28025 kPa for produced Eagle Ford oil. This is attributed to the presence of kerogen. This suppression depends on the type and level of maturity of the kerogen. The confinement of hydrocarbon fluids in the nanometer pores present in shales also changes the behavior of these fluids. Pore-wall – fluid interactions become dominant at the nano-scale and conventional equations of state

(EOS) fail to include the effect of these confined state interactions. Gibbs Ensemble Monte Carlo simulations were performed in this work to investigate the thermodynamic properties of pure components and fluid mixtures in confined pores. Suppression of critical densities and critical temperature of confined decane, decane–methane, and decane–carbon-dioxide was observed from the bulk properties. This leads to changes in the saturation pressures of fluids in the confined state.

Experiments on kerogen isolated from a shale and oil were performed with a differential scanning calorimeter and a thermogravimetric analyzer. These experiments complimented the modeling results and thus, verified the effect of kerogen and hydrocarbon fluid confinement observed in the models. Finally, for gas-rich shales, a carbon dioxide injection as the most effective method was evaluated for enhanced production of gas sorbed in kerogen. Molecular modeling indicates that the carbon dioxide can replace methane sorbed in the kerogen and the kerogen matrix decreases in volume during this process. The carbon dioxide shows higher retention in the kerogen than methane, indicating the viability of enhanced gas recovery and carbon dioxide sequestration.

To my family and friends

## TABLE OF CONTENTS

## ACKNOWLEDGEMENTS

First of all, I am extremely grateful to my advisor, Professor Milind Deo, for his guidance and encouragement throughout this research work. I thank him for allowing me to nurture my intellectual faculties to their utmost levels. I would like to thank the members of the supervising committee, Dr. John McLennan, Dr. Raymond Levey, Dr. Eric Eddings, Dr. Edward Trujillo, Dr. Jonathan Craig, and Dr. Ger Van Graas, for their comments and suggestions. I am thankful to all the faculty and staff of the Chemical Engineering Department for their support in the graduate program. I would like to thank Dr. Hai Huang, Dr. Paul Meakin, and Dr. Keith Prisbrey for detailed discussions related to my research. I am grateful to the Energy & Geoscience Institute (EGI) for providing me financial support for my graduate study. I am also grateful to Idaho National Laboratory for providing me access to high performance computing resources. I thank my colleagues and classmates for making the workplace friendly and productive. Finally, I express my respect to my parents, brother, friends, and family members for their support, encouragement, and motivation. I would like to thank Sugandha Sharma for supporting me throughout this endeavor.

# CHAPTER 1

# INTRODUCTION

To increase the recoveries of hydrocarbons from shale plays beyond 20%, understanding the dynamics at a pore scale is required. Larger recoveries would help in efficient and environmentally friendly exploitation of oil and gas from shale.

## 1.1 Research Motivation

In the last decade, shale play resources have played a key role in increasing oil production in the United States. However, the average hydrocarbon recovery factors from many of these formations are usually less than 20% (less than 10% for oil and 20% for gas-rich shale plays). There is a considerable interest in understanding the production of liquids from shale rock plays such as the Eagle Ford Play in Texas. The sizes of pores in shales holding the oil are believed to be of the order of nanometers. The fluids present in such small nanopores and in contact with kerogen may have different properties compared to their properties measured in bulk. Correct prediction of thermodynamic properties of reservoir fluids in shales is critical for increasing recoveries from shale plays. “Shale” rocks are in most cases not “true” shales (i.e. having a high proportion of clay minerals) but fine-grained rocks – often carbonate- and/or silica-rich.

## 1.2 Objectives

In view of important requirements for improved recovery, the following research objectives have been proposed:

- Develop a thermodynamic model to account for the effect of kerogen on Pressure-Volume-Temperature (PVT) properties of fluids in shale reservoirs
- Develop a molecular scale model to understand the dynamics of kerogen and hydrocarbon fluids
- Develop a molecular scale model to understand the effect of confinement (in nanometer scale porosity) on fluid thermodynamic properties in shales
- Perform experiments to support and complement these models in order to understand the effect of kerogen and nanopores in shales on PVT properties of reservoir fluids.

## 1.3 Need for Understanding Dynamics at a Pore Scale

Fluid saturation pressures at in-situ temperatures – bubble points for oils and dew points for condensates in shale nanopores, are affected by the influence of the pore walls in the vicinity of the fluid molecules. Moreover, kerogen, a solid organic constituent of shale, behaves like a crosslinked polymer and preferentially absorbs a portion of the oil present in these rocks. Such interactions with kerogen also change the PVT properties of oil in association with the kerogen. Therefore, thermodynamic properties of those fluids change in the presence of crosslinked polymers (kerogen) and in confined spaces (nanopores in shales). Correct prediction of the deviation in these properties is valuable to many industries including the oil and gas industry. Approach to bubble point or dew point influences the proportion of liquid or gas produced from a given producing well,

and thus impacts the economic viability. Hence, an accurate measure of saturation pressures is important. Traditional equations of state fail to consider the complexity of pore wall interactions and kerogen swelling in the determination of thermodynamic properties of fluids in contact with kerogen and in confinement. It is important to understand how liquids are produced from ultra-low permeability rocks so that production rates and recovery can be optimized.

The current Ph.D. research work includes the study of thermodynamics of solvent (oil) – kerogen (polymer) interaction, Molecular Dynamics (MD) simulations for assessment of kerogen swelling, as well as Monte Carlo simulations in Gibbs Ensemble for understanding phase behavior of confined fluids. There are also experiments conducted on isolated kerogen and hydrocarbon fluids using Differential Scanning Calorimetry (DSC) and a Thermogravimetric Analyzer (TGA) to understand kerogen swelling and the associated effect on PVT properties of oil. Finally, MD simulations investigated the possibility of using $CO_2$ as enhanced production technology for gas-rich shales.

The results from Molecular Dynamics simulations in Chapter 2 show that kerogen interacts with hydrocarbons. The subsequent thermodynamic modeling in Chapter 2 demonstrates that kerogen-oil interaction suppresses the bubble point of oil in shales when compared to the bubble point of oil in the bulk.

Gibbs ensemble Monte Carlo (MC) simulations were used in Chapter 3 to understand the effect of confinement of fluid molecules on fluid density and phase behavior of the confined fluid. The traditional equations of state fail to consider the complexity of pore wall interaction in calculating thermodynamics properties of confined fluids. MC

simulations were performed for binary mixtures of decane-methane, decane-$CO_2$ at different molar ratios confined in a slit-graphite nanopore. The research has shown that confinement of fluids in nanopores leads to suppression of critical properties of these fluids mixtures.

Chapter 4 describes experiments performed with pure isolated kerogen to investigate the effect of kerogen and nanoporosity on the bubble point temperature of pure component and oil using a Differential Scanning Calorimeter (DSC) and a Thermogravimetric Analyser (TGA). The results indicate suppression in the bubble point temperatures of hydrocarbon fluids in the presence of kerogen with nanopores.

The possibility of enhanced oil recovery using $CO_2$ injection is studied in Chapter 5. The self-diffusivities of $CO_2$ were found to be on the order of $10^{-9}$ $m^2/s$ in kerogen. The current research demonstrates that $CO_2$ has more affinity for sorption in kerogen-like organic macromolecules compared to $CH_4$ and that $CO_2$ swells kerogen less than equal moles of $CH_4$.

# CHAPTER 2

# EFFECT OF THE PRESENCE OF ORGANIC MATTER ON BUBBLE POINTS OF OILS IN SHALES

## 2.1 Abstract

The relative amounts of oil and gas produced in prolific plays like the Eagle Ford are affected by the oil's bubble point. The oil and kerogen (organic matter) coexist and the oil may remain in contact with the kerogen. Bulk experiments and molecular simulations clearly show that kerogen preferentially absorbs hydrocarbons. The retained oil phase remains in multicomponent equilibrium with the expelled oil produced at the surface. Results from a model proposed to calculate the bubble points (at 400 K) of in-situ oils (retained + free) in the presence of kerogen indicate suppression of about 4150 kPa – 16350 kPa from the original value of 28025 kPa of a produced Eagle Ford oil. These calculations depend on the type and level of maturity of kerogen. Reliable prediction of accurate saturation pressures has key implications on recovery volumes and production rates from liquid-rich shales.

## 2.2 Introduction

Recent technological advances have made recovery of liquid hydrocarbons possible from the ultra-low permeability shales. However, recoveries from these liquid-rich shales

---

still tend to be low. It is believed that more than 90% of generated oil still remains in the formation[1]. Better understanding of fluid thermodynamic and transport properties is necessary to understand the cause of these low recoveries and subsequently improve production.

One of the reasons for poor recoveries is the large declines in liquid rates in the first few months of production that are usually associated with a larger fraction of gas production. Shales producing liquids are undergoing primary production. The physical production system is shown schematically in Figure 2.1. Figure 2.1 shows a shale sandwiched between other strata with a horizontal well landed in the shale formation. The shale is eventually hydraulically fractured to produce oil and gas. During production, the hydraulic fracture face and some portions of the horizontal well are maintained well below the bubble point of the reservoir fluid. However, in a low-permeability system, most of the reservoir remains above the bubble point. Interactions of oil in kerogen with free oil and their associated gas (Figure 2.1) present in shales are the theme of this chapter. These interactions occur at a pore scale and affect the saturation pressure of oil when it is in contact with kerogen. Saturation pressures are important operational parameters while drilling a well. The reservoir fluids stay in two phases below the saturation pressures of the oil, which may not be desirable during production.

Organic matter (kerogen) is a key component in liquid-rich shales. Kerogen is a carbonaceous material, which is believed to be the precursor of hydrocarbons. Kerogen is typically classified into four types, viz. type I, II, III, and IV. The classification is based on the source of the organic matter and the general depositional environment, as shown in Table 2.1. Sometimes, type II kerogen is sulfur rich and is then known as type IIS. Any

of the type I, II, and III kerogens can exist in the oil, dry gas, or wet gas windows depending on their maturity. A van Krevelen[2] diagram (Figure 2.2) shows these three maturity windows based on the Hydrogen to Carbon (H/C) and Oxygen to Carbon (O/C) ratios of the kerogen. The red dot in Figure 2.2 indicates a type of kerogen, whose model was used in molecular dynamics simulation, described later in the text. During catagenesis[3,4] of an oil prone type II kerogen, the kerogen transforms and converts into oil leaving behind residual kerogen matrix. A shale rich in such type II kerogen usually contains liquid hydrocarbons. The liquid hydrocarbons may or may not be associated with their gas components in the reservoir. When the reservoir pressure is above the bubble point pressure of the oil, the gas is dissolved in the oil. A part of the generated oil expels out of the residual kerogen matrix, and the rest is retained within the kerogen[5]. The expelled oil is also referred to as 'free oil' in the current work, while the oil retained within the residual kerogen matrix is referred to as 'retained' oil. The absorbed/retained oil is the sum of generated oil that is retained and expelled oil that is absorbed back into the matrix; however, it is difficult to differentiate between the two. Hence, the sum would be referred to as just 'retained oil' in this manuscript. Some portion of the retained or absorbed oil can also be referred to as bitumen which is soluble in organic matter. This is usually the heaviest portion of the oil. The free oil outside the kerogen matrix in a shale may remain in a multicomponent equilibrium with the retained oil[6,7] as shown in Figure 2.3. Water may be present and the phase behavior of water and hydrocarbons followed by multiphase expulsion of oil and water is important. The water may have a role in the generation of oil and gas[8,9]. However, for the purposes of this paper, it is assumed that water does not affect the free oil-retained oil equilibrium. Figure 2.3 shows crosslinked

kerogen with retained oil. The retained oil phase is in multicomponent equilibrium with the free oil immediately outside the kerogen matrix. The two oils together form oil present in the shales at in-situ state. It is the free oil that is produced at the surface.

### 2.3 Kerogen Swelling and Oil Partitioning

Previously, researchers have theoretically studied and experimentally demonstrated the swelling of kerogen in the presence of organic solvents[6,10–15]. These authors suggest that the organic solvents are absorbed into the kerogen matrix. Considering the crosslinked nature of kerogen, the equilibrium behavior between the retained oil in the kerogen matrix and the expelled free oil is studied using an extended Flory-Rehner Regular Solution (FRRS) theory model[6]. Similar volumetric swelling observed from experiments and calculated from extended Flory-Rehner Regular Solution (FRRS) theory indicates that absorbed solvent stays in dissolved form in the kerogen and remains in equilibrium with the solvent outside the matrix.

Further, Molecular Dynamics (MD) simulations have been used in the current chapter to demonstrate the swelling behavior of kerogen in the presence of organic solvents. The current work used xyz coordinates of atoms in the type II C kerogen model published by Ungerer et al. (2015)[16] and remodeled it by assigning parameters using the General Amber Force Field (GAFF) from Wang et al. (2004)[17]. A remodeled kerogen structure was then used to measure the bulk properties of kerogen by performing MD simulations. The type II C kerogen model corresponds to a type II kerogen from the Duvernay Formation (sample C in Kelemen et al., 2007[18]). The H/C and O/C ratios of this model unit are 0.905 and 0.054, respectively, and the kerogen model plots in the middle to end of the oil window as shown in the van Krevelen diagram (Figure 2.2).

A molecule of type II C kerogen in the protein data bank (PDB) format, rewritten for GAFF, was used to produce the bulk kerogen model. Ten such molecules were packed randomly into a simulation box using the Packmol[19] tool to form a bulk kerogen. The PDB of bulk kerogen was taken into the Visual Molecular Dynamics (VMD)[20] tool to write an input file for the Large-scale Atomic/Molecular Massively Parallel Simulator (LAMMPS) tool[21]. The Nose-Hoover style non-Hamiltonian equations of motion were used in a molecular simulator to generate positions and velocities sampled from the canonical (NVT) and isothermal-isobaric (NPT) ensembles. Simulated annealing was performed through a series of energy minimization steps. The density of the final kerogen structure was calculated at the end of simulated annealing. The density of annealed structure of modeled kerogen was around 1.15 g/cc at 300 K and 300 atm pressure. The density from simulations matches densities obtained from experiments (1.18-1.29 g/cc) in Okiongbo et al. (2005)[22], and simulations (1.13 g/cc) in Ungerer et al. (2005)[16]. The radial distribution function, g(r), gives the probability of finding a particle at a distance (r) from another particle, averaged over all of the particles in the system. The calculated radial pair distribution function with peaks at 1.35 Å and 1.55 Å corresponding to C-C aromatic and C-C aliphatic bond lengths, respectively, is in good agreement with the radial pair distribution function (calculated at 300 K and 0.98 atmosphere) of Ungerer et al. (2015)[16], who developed the original molecular structure model. The final annealed structure of bulk kerogen at minimum energy state would be used to further measure swelling of kerogen in presence of organic solvents.

To calculate swelling of kerogen in presence of organic solvents, the subsequent simulations in NPT ensemble and periodic boundary conditions 300 K and 30400 kPa

pressure were performed with 20% decane molecules by mass (10 molecules of kerogen simulated with 49 molecules of decane). With decane as a solvent, volumetric swelling ratio (swelled volume/original volume) of ~1.2 was obtained with the type II kerogen (Figure 2.4) at the end of simulations. Researchers have previously studied swelling of kerogen using theory and experiments[6,10–15] and obtained similar volumetric swelling ratio with different organic solvents including decane. Ertas et al. (2006)[6] obtained volumetric swelling ratio (swelled volume/original volume) of 1.22 for decane at 303.15 K temperature. The swelling behavior of kerogen observed by MD simulations again confirms that kerogen absorbs solvents including hydrocarbons and the hydrocarbons expelled from the kerogen structure during the catagenesis may remain in a multi-component equilibrium with the hydrocarbons absorbed/retained in the residual kerogen matrix[6,7]. The good match in the volumetric swelling of type II kerogen associated with absorption of solvents, from experiments, extended FRRS theory, and molecular simulations further confirms that kerogen behaves as a crosslinked elastomer with non-specific interactions (no hydrogen bonding) between kerogen and oil[6,7] and it fractionates oil into absorbed/retained and free oil phase.

The above discussion establishes that the oil generated by transformation of kerogen is partitioned into absorbed/retained and free oil phase by the residual kerogen matrix. All of the generated oil resides in either of the two forms – oil outside the kerogen matrix or oil inside the kerogen matrix. The oil inside the matrix could have been generated by a combination of retention of some of the generated oil during the transformation and absorption of some of the free oil after transformation, such that the oil inside and outside of kerogen eventually achieves equilibrium. It is difficult to differentiate between the

retained oil and the oil that was absorbed later from the free phase. To facilitate this differentiation, the oil inside the kerogen is termed retained oil. This retained oil inside the kerogen stays in the dissolved form within the kerogen matrix. Because of the absorption of oil, the kerogen swells in volume as shown in Figure 2.5. The oil retained in the kerogen matrix remains in multicomponent equilibrium with the free oil surrounding the kerogen matrix (Figure 2.3 and Figure 2.5). It is the free oil that is produced at the surface. The bubble point of Eagle Ford oil used in the conventional simulators or for other engineering purposes refers to the bubble point of this free oil. The retained and free oil together constitute the in-situ oil present in the shales. The phase transition to gas from an oil takes place in the reservoir – thus, the saturation pressure of the oil-gas mixture in the presence of kerogen is relevant. This oil-gas equilibrium in the reservoir is established between the in-situ oil and its gas component. Thus, all three phases, namely free oil, retained oil, and gas, achieve equilibrium (Figure 2.6). The following three phases that stay in equilibrium in the liquid-rich shales will be discussed in the rest of the text:

1. The retained oil (a) phase in kerogen (ker)
2. The free oil (f) phase
3. The gas (g) phase

The chemical potential of oil inside kerogen depends on total contribution from elastic entropy ($\Delta S_{el}$), entropy of mixing ($\Delta S_M$), and enthalpy of mixing ($\Delta H_M$)[23,]. The species move in the direction of least chemical potential to attain a lower energy state. The difference between chemical potential of any component of oil inside and outside the kerogen matrix ($\Delta\mu_i$) is given in Ertas et al. (2006)[6].

$$\frac{\Delta\mu_i}{k_B T} = \frac{1}{k_B T}\frac{\partial}{\partial n_i}\left[\Delta H_M - T\left(\Delta S_M + \Delta S_{el}\right)\right] = \ln v_i + \sum_j v_j\left(\frac{v_j - v_i}{v_j}\right) + v_i\left(\sum_{j\neq i} b_{ij} v_j - \sum_{j<k} b_{ik} v_j v_k\right) + v_o + v_i\left\{b_{io} v_o^2 + v_o \sum_j v_j (b_{io} - b_{jo}) + \frac{N_e}{V_o}\left(v_o^{1/3} v_{eq}^{2/3} - v_o\right)\right\} \quad (2.1)$$

where $\Delta\mu_i$ indicates change in chemical potential; $k_B$ is Boltzmann constant, $b_{ij} = \left(\delta_i - \delta_j\right)^2 / k_B T$, $\delta_i$ are Hildebrand solubility parameters for solvent species i given in Flory (1943); $v_i, v_j$ are molecular volumes of the solvents; $v_i$ , $v_j$ , $v_k$ are volume fractions of solvents; $n_i$ is total number of solvents i; $N_e$ is effective number of chain elements in a crosslinked network of kerogen; $v_o$ indicates swollen volume fraction of kerogen; $v_{eq}$ is native swelling volume fraction; and $\mu_i^a, \mu_i^f, \mu_i^g$ are chemical potentials of $i^{th}$ species in three phases – retained (a), free (f), and gas (g), respectively.

### 2.4 Phase Behavior Calculations

For the three phases to stay in a multicomponent equilibrium in a shale, the chemical potential of the $i^{th}$ component in all of the three phases must be equal.

$$\mu_i^a = \mu_i^f = \mu_i^g \quad (2.2)$$

The preference factors determined in Walter (2013) are the numerical values that provide the extent of partitioning of any $i^{th}$ component between retained and free oil phase. The preference factors were calculated by solving retained oil-free oil equilibrium and could be used to calculate the composition of retained oil according to the following relation:

$$y_i = P_i x_i / \Sigma(P_i x_i) \quad (2.3)$$

$$o_i = X x_i + Y y_i \quad (2.4)$$

where $P_i$ denotes preference factors from Walter et al. (2013) for i$^{th}$ specie, $x_i$ is mole fraction of i$^{th}$ component in the free oil phase, $y_i$ is mole fraction in retained oil phase, X is volume fraction of free oil, Y is volume fraction of retained oil, and $o_i$ is overall mole fraction of in-situ oil in the shale formation.

This i$^{th}$ component of in-situ oil stays in equilibrium with its gas component such that the chemical potentials of i$^{th}$ component in all three phase, viz. retained, free, and gas phase, are equal. The Peng Robinson equation of state[24] was used to solve the equilibrium between gas and in-situ oil (free and retained oil phases) (Figure 2.6):

$$P = \frac{RT}{\mathrm{v}-b_i} - \frac{a_i(T)}{\mathrm{v}(\mathrm{v}+b_i)+b_i(\mathrm{v}-b_i)} \tag{2.5}$$

$$K_i^{g-o} = \frac{\emptyset_i^o}{\emptyset_i^g} \tag{2.6}$$

where $\emptyset_i^o$ is fugacity coefficient of i$^{th}$ component in 'in-situ' oil (o) phase, $\emptyset_i^g$ is fugacity coefficient of i$^{th}$ component in gas (g) phase, $K_i^{g-o}$ is equilibrium coefficient between gas and in-situ oil phase, $a_i$ and $b_i$ are equation of state parameters, v is molar volume, P denotes pressure (kPa), R denotes ideal gas constant, and T denotes temperature (K). The subscript i refers to the total number of components in the oil (1, 2,3….n).

From here, the work was divided into two parts – calculation of the effect of kerogen maturity on the bubble point of free oils and the calculation of the bubble point of in-situ oil in the presence of kerogen of different maturities.

The first part replicates the geologic process of maturation of kerogen and aims to study the change in bubble points of produced free oils as the kerogen matures. From Walters et al. (2013)[25], the preference factors for type II/IIS kerogen with HI values of 50%, 75%, and 100% HI (HI = 650 mg HC/g TOC) were considered to calculate the

composition of free, retained, and in-situ oil in presence of kerogen of increasing maturity (Table 2.2). The HI values in Table 2.2 represent HI values of present-day kerogen after 100%, 75%, and 50% conversion from original HI value of 650 mg HC/g TOC HI and the maturity of kerogen increases from 50% to 100% conversion. Table 2.2 shows lumped oil fractions and corresponding preference factors for the three different maturity values of type II/IIS kerogen. It is shown in Table 2.2 that the preference factors in general increases from low maturity kerogen (50% conversion) to higher maturity kerogen (100% conversion). This signifies that kerogen retains higher amounts of oil as it matures in nature. In the Table 2.2, for a particular maturity, the preference factor usually increases from smaller chain compounds to larger chain compounds and from saturated to aromatics for compounds with the same number of carbon atoms. This reveals that kerogen tends to retain heavier and aromatic compounds and expels lighter and saturated compounds.

The second part of the chapter aims to replicate a more realistic present-day scenario. In the present day, the free and retained oil together form the in-situ oil in the shales. In shales, free oil would have different PVT properties than the in-situ oil. Therefore, calculations of rates and hydrocarbon recovery volumes that are based on PVT properties of the free oil alone will lead to different results. It is the in-situ oil whose PVT properties should be considered to estimate true rates and hydrocarbon recovery volumes. The properties based on free oil do not reflect the in-situ behavior of oil. The in-situ behavior of oil (calculated based on composition of in-situ oil and not free oil) is required to know the true PVT behavior of the reservoir fluids in the subsurface. The correct properties would allow the operators to operate the well at a lower bottom hotel pressures without

increasing production GOR significantly. In this work, the composition of in-situ oil was back-calculated from the compositions of produced free oil in order to estimate the bubble point of in-situ oil.

## 2.5 Results and Discussion

### 2.5.1 Effect of Maturity on Bubble Points

For the purpose of demonstration of the proposed model, an approximate Eagle Ford oil composition slightly modified from Whitson and Sunjerga (2012)[26] is used as the composition of oil generated by catagenesis of kerogen. This composition is shown in Table 2.3 (first and second columns). The kerogen fractionates this generated oil into free and retained oil phase. The composition of free oil was calculated by partitioning the Eagle Ford oil composition into free and retained oil by using the preference factors. The volumetric swelling and the expulsion efficiency of kerogen were assumed to be 1.6 and 0.9, respectively, in the calculation of the preference factors[25].

In this work, compositional lumping was performed on Whitson and Sunjerga (2012)[26] Eagle Ford compositions to match the compositions cited in Walters et al. (2013)[25] in order to use the latter's preference factors. Columns 3 and 4 of Table 2.3 show the lumped components and their compositions, respectively. The Lee-Kesler[27] mixing rules in the Winprop™ simulator (A commercial multiphase, multicomponent thermodynamic program from CMG– Computer Modeling Group) are used to calculate the critical properties of the lumped components. Further, the compositions of C6-C14 and C14+ were split into Aromatics (Aros) and Saturates (Sats) with an assumption that amount of saturated compounds is 1.8 times the amount of aromatics, as shown in Table 2.3. However, if this fraction was assumed to be 1.5 and 2, the compositions of the free

oil phase after partitioning were not significantly different. Columns 5 and 6 of Table 2.3 arithmetically combine the components in order to use the phase behavior calculation simulator (Winprop) to plot the PT graphs. The composition of free oil in the last two columns of Table 2.3 is used in Winprop to produce PT plots. Table 2.3 shows the lumping, splitting, and combining components of the original Eagle Ford oil as an exercise. In the case when oil is in contact with organic matter (kerogen), to account for the presence of kerogen, the free oil was fractionated in the columns 3 and 4 by using the preference factors cited in Walters et al. (2013)[25] before combining the components in the last two columns.

The composition of the free Eagle Ford oil is tabulated in Table 2.4 along with the compositions of the free oil phase after partitioning in different maturity type II kerogens. It can be observed from Table 2.4 that the amounts of lighter components decrease and the amounts of heavier components increase in the fractionated or partitioned free oil as the kerogen matures from 50% conversion to 100% conversion. This exercise was implemented in order to see the effect of the maturity of kerogen on saturation pressures of any oil – Eagle Ford oil as an example – which is fractionated into free and retained phases by kerogen. The trend in the saturation pressure of the different oil fractionated by a type II kerogen of different maturity (HI) was observed. Winprop generated the two-phase envelope in the P-T plot (Figure 2.7). The changes in bubble point pressure of free oil partitioned from Eagle Ford oil with the maturity of type II kerogen is shown in the Table 2.5 and Figure 2.7. It is evident from the Table 2.5 and Figure 2.7 that the bubble point pressure decreases with maturity of the present day kerogen. This contradicts observation by di Primio et al. (1998)[28] where they used sets of data collected from

experiments of artificial maturation of a Duvernay kerogen sample and composition of real oil samples. As mentioned in Walters et al. (2013)[25], the presence of polar-rich fluids in expelled free fraction at higher levels of thermal maturation is the reason for such a contrast. This, however, is not a flaw in the model; rather, it indicates that the composition of the primary expelled products is not fixed but keeps changing as the evolved polar compounds undergo secondary cracking reactions. During the maturation of kerogen, the crosslink density of kerogen increases[10]. The change in macromolecular structure of kerogen with maturity changes its behavior in absorbing oils. The bubble point of original Eagle Ford oil lies close to the bubble points of oil in presence of kerogen with maturity of 162.5 mg/g TOC (75% HI) (Table 2.5 and Figure 2.7).

The actual ratios of saturates to aromatics in the Eagle Ford oil[26] were not known. Three ratios of saturates to aromatic compounds (1.5, 1.8, and 2.0) were used to determine the sensitivity to this number, and the results are presented in Table 2.6. The composition of free oil does not change significantly when different ratios of saturates to aromatic compounds were used in the initial lumping of Eagle Ford oil. Therefore, all the calculations were performed with a saturates to aromatics ratio of 1.8 during the process of lumping for the remainder of the paper.

### 2.5.2 Bubble Points of In-situ Oils

A more realistic field-related analysis was performed for the Eagle Ford play in the second part of this chapter. The Eagle Ford oil composition was treated as free oil because the oil produced in the Eagle Ford play is actually the free oil phase present in the Eagle Ford shales. Previously it has been suggested that the kerogen found in the Eagle Ford shale is of type II[29,30]; however, some researchers[31,32] reported sulfur-rich,

Type IIS kerogen in Eagle Ford samples, with maturities ranging from 0-750 mg HC/g TOC hydrogen index[29,33]. The spread in the hydrogen index (HI) of Eagle Ford kerogen is shown in Figure 2.8; the sample data for Eagle Ford were taken from Romero (2014)[29]. The compositions of the 'in-situ' oil were back calculated from the free oil Eagle Ford compositions, again using the preference factors shown in Table 2.2 for Type II and IIS kerogen. For realistic assumptions, the preference factors for kerogen with HI values of 50%, 75%, and 100% HI (HI = 650 mg HC/g TOC)[25] were used in the calculation as they fall in the range of the HI observed for Eagle Ford kerogen as discussed earlier. Table 2.7 lists the compositions of the free Eagle Ford oil for a specific case of 162.5 mg HC/g TOC Type II kerogen that is produced and compositions of in-situ Eagle Ford oil that are actually proposed to be present in the formation. This in-situ oil (Figure 2.9a) partitions into free (Figure 2.9b) and retained oil (Figure 2.9c) phases. Figure 2.9 shows the compositions of the in-situ oil and the two phases (free and retained oil) that are partitioned from the in-situ oil. It is shown in Table 2.7 that the free oil phase has a larger amount of lighter and non-polar compounds while the in-situ oil is enriched in heavier and polar compounds. The composition of the free oil phase (Figure 2.9b) and the composition of retained oil in the absorbed phase (Figure 2.9c) indicate that the kerogen expels saturates more than aromatics and polar compounds, and thus tends to retain aromatics and heavier polar components. This observation is made for the particular case of Type II kerogen with 162.5 mg HC/g TOC HI; however, it has also been observed in previous studies[5,34,35]. The composition of retained oil matches well with general understanding of the composition of bitumen which is believed to be rich in aromatic and heavier polar compounds

The vapor-liquid phase equilibrium is studied for free and in-situ oil. The bubble point pressure of produced oil (free oil) was found to be different from the bubble point of in-situ oil that actually resides in the shale reservoir. To calculate the effect of the presence of kerogen on bubble points of oil, preference factors for both type II and type IIS (0-325 mg HC/g TOC HI) from Walters et al. (2013)[25] were used. It was observed that a suppression ranging from about 4150 kPa – 16350 kPa occurs in the bubble point pressure (at 400 K) for in-situ oil from the original bubble point 28025 kPa (at 400K) of produced 'free' oil in presence of type II/IIS kerogen. The calculations are performed for three values of expulsion efficiency – 0.7, 0.8, and 0.9. Expulsion efficiency is defined as proportion of expelled oil to retained or absorbed oil[25]. The P-T plots for three different expulsion efficiencies are given in Figure 2.10 (a, b, c) for type II/IIS kerogen. The bubble points of in-situ oils increase slightly as the expulsion efficiency increases. However, the bubble points of in-situ oils of all expulsion efficiencies were largely suppressed from the bubble point of free oil that is produced from Eagle Ford. Smaller suppressions in bubble points of oil were observed in presence of type IIS kerogen. The developed model applies well on any liquid rich shales with type II/IIS kerogen such as the Eagle Ford shale. Thus, it was found that the saturation pressures are different for produced Eagle Ford oil and in-situ Eagle Ford oil.

The presence of kerogen affects the fluid properties in shale reservoirs. The critical points of oils change in the presence of kerogen. Figure 2.11 shows that the critical pressures of in-situ oils were less than the critical pressures of free oil, while the opposite trend was seen for critical temperatures in the presence of type II/IIS kerogen at different levels of maturity (assuming expulsion efficiency= 0.9). The critical temperatures of in-

situ oils were higher than the critical temperatures of free oils. Figure 2.11 shows that the suppression in critical pressure and elevation in critical temperature increases with maturity of the type II/IIS kerogen. It can be observed in Figure 2.11 that the presence of type II kerogen causes larger deviations in critical points than type IIS kerogen from the original critical point of Eagle Ford oil. The deviated thermodynamic fluid properties have implications on predicted volumes and recoveries from the shale reservoirs, calculated by the conventional reservoir simulators.

## 2.6 Conclusions

The kerogen in shales partitions oil into retained and free phases. The importance of retained oil (in kerogen) in the calculation of bubble points of oils in shales has been discussed in the current work. The oil that is generated by the organic matter in shales partitions into a free oil phase and the retained oil which is retained by the kerogen. Compositions of the free and the retained oils are calculated using preference factors for specific types of kerogen. The compositions of in-situ oil in shales are used to calculate the actual bubble points of oil in shales. Retained oils are relatively enriched in aromatics and polar compounds and depleted in saturates and lighter compounds. As the maturities of kerogen increase, the bubble points of fractionated free oils decrease. The compositions of in-situ oil (combination of the free and the retained oil) and not the free oil is considered while calculating the saturation pressures of oils in liquid-rich shale plays. The bubble points of in-situ oils are lower by as much as 4150 – 16350 kPa at 400 K depending on the expulsion efficiency, and type and maturity of the kerogen. Type II kerogen causes larger suppression in bubble points of produced free Eagle Ford oil than type IIS kerogen. Lower bubble point pressures may help engineers operate wells at

lower pressures without risking excess gas production. This would help increase rates and economics of production.

Table 2.1. Different types of kerogen and their source and depositional settings. Modified from McCarthy et al., 2011)[36]

| Kerogen Type | Source Material | Depositional setting |
|---|---|---|
| I | Algae | Lacustrine |
| II | Plankton and some algae | Marine |
| III | Higher Plants | Terrestrial |
| IV | Reworked, oxidized material | Varied |

Table 2.2. Preference factors for Type II and IIS kerogen of varying maturity taken from Walters (2013). The original HI is 650 mg/g TOC and preference factors for 50% conversion (325), 75% conversion (162.5.5), and 100% conversion (no potential for further generation) are mentioned in the table. The preference factors increase from low maturity kerogen (50% conversion) to higher maturity kerogen (50% conversion). For a particular maturity, the preference factor usually increases from lighter components to heavier components and from saturated to aromatics for components with similar weights. Sats indicates fraction of saturated compounds, Aros indicates fraction of aromatic compounds and NSOs indicates fraction of polar compounds.

| | Type I | | | Type IIS | | |
|---|---|---|---|---|---|---|
| Lumped Components | Preference factor, $P_i$ (50% HI) | Preference factor, $P_i$ (75% HI) | Preference factor, $P_i$ (100% HI) | Preference factor, $P_i$ (50% HI) | Preference factor, $P_i$ (75% HI) | Preference factor, $P_i$ (100% HI) |
| Methane | 0.000567 | 0.00301 | 0.024565 | 0.002189 | 0.034156 | 0.06244 |
| Ethane | 0.000567 | 0.002658 | 0.017853 | 0.001979 | 0.02538 | 0.043657 |
| Propane | 0.000523 | 0.002171 | 0.012045 | 0.001662 | 0.017628 | 0.028588 |
| Butane | 0.000491 | 0.001801 | 0.008208 | 0.00142 | 0.012351 | 0.018848 |
| Pentane | 0.000566 | 0.001857 | 0.007037 | 0.0015 | 0.010667 | 0.01534 |
| C6-C14 Sats | 0.000879 | 0.001909 | 0.003116 | 0.001715 | 0.004847 | 0.005452 |
| C6-C14 Aros | 0.016487 | 0.06029 | 0.214116 | 0.046181 | 0.235041 | 0.304303 |
| C14+ Sats | 0.001184 | 0.001554 | 0.000849 | 0.001605 | 0.001415 | 0.001101 |
| C14+ Aros | 0.015535 | 0.045923 | 0.276071 | 0.033195 | 0.29098 | 0.305952 |
| C14+ NSOs | 1 | 1 | 1 | 1 | 1 | 1 |

Table 2.3. Systematic lumping of Whitson and Sunjrega (2012) oil composition to match Walters (2013) compositions for ease in using the latter's preference factors. The column 1 and 2 described the Eagle Ford oil composition from Whiston and Sunjrega (2012). Further, the C6-C14 and C14+ were splitted into Aromatics (Aros) and Saturated (Sats). The column 3 and 4 describes the systematic lumping using Lee-Kesler (1975) mixing rules. The column 5 and 6 describes the arithmetic re-lumping for use in Winprop to plot PT diagrams.

| Components from Whitson and Sunjrega, 2012 | Mole fractions from Whitson and Sunjrega, 2012 | Lumped Components to match components in Walters et al., 2013 | | Composition of Lumped Components (saturated=1.8 aromatics), mole fractions | Re-lumped components to produce PT plots | Compositions to produce PT plots ($x_i$, mol fractions) |
|---|---|---|---|---|---|---|
| H2S | 0.00 | | | | | |
| N2 | 0.13 | | | | Methane | 0.5091 |
| CO2 | 0.0195 | | | | Ethane | 0.0625 |
| C1 | 0.4885 | C1 | | 0.5091 | Propane | 0.0350 |
| C2 | 0.0625 | C2 | | 0.0625 | Butane | 0.0218 |
| C3 | 0.035 | C3 | | 0.0351 | Pentane | 0.0131 |
| I-C4 | 0.0081 | | | | C6-C14 | 0.2267 |
| N-C4 | 0.0137 | C4 | | 0.0218 | C14+ | 0.1186 |
| I-C5 | 0.0063 | | | | C14+ NSOs | 0.0132 |
| N-C5 | 0.0068 | C5 | | 0.0131 | Sum | 1 |
| C6 | 0.0096 | | | | | |
| C7 | 0.0389 | | | | | |
| C8 | 0.037 | C6-C14 | | 0.2267 | | |
| C9 | 0.0317 | C6-C14 | C6-C14 Sats | 0.1457 | | |
| C10 | 0.0279 | | C6-C14 Aros | 0.0809 | | |
| C11 | 0.0245 | | | | | |
| C12 | 0.0215 | | | | | |
| C13 | 0.0189 | | | | | |
| C14 | 0.0167 | | | | | |
| C15 | 0.0147 | C14+ | | 0.1186 | | |
| C16 | 0.0129 | C14+ | C14+ Sats | 0.0762 | | |
| C17 | 0.0114 | | C14+ Aros | 0.0423 | | |
| C18 | 0.0101 | C14+ NSOs | | 0.0132 | | |
| C19 | 0.00889 | | | | | |
| C20 | 0.00787 | | | | | |
| C21 | 0.00697 | | | | | |
| C22 | 0.00617 | | | | | |
| C23 | 0.00548 | | | | | |
| C24 | 0.00487 | | | | | |
| C25 | 0.00433 | | | | | |
| C26+ | 0.0381 | | | | | |

Table 2.4. Compositions of free oil in contact with type II kerogen of 325 mg HC/g TOC HI, 162.5 mg HC/g TOC HI, and 0 mg HC/g TOC HI, respectively. The column 1 shows the original Eagle Ford composition that was partitioned by kerogen as it matures from 50% conversion of kerogen to 100% conversion. The original HI is 650 mg/g TOC.

| Components | Original $x_i$ (Eagle Ford oil) | New $x_i$ partitioned from original $x_i$ with Type II (of 50% HI) kerogen | New $x_i$ partitioned from original $x_i$ with Type II (of 75% HI) kerogen | New $x_i$ partitioned from original $x_i$ with Type II (of 100% HI) kerogen |
|---|---|---|---|---|
| c1 | 0.5091 | 0.6251 | 0.5476 | 0.4400 |
| c2 | 0.0625 | 0.0767 | 0.0713 | 0.0644 |
| c3 | 0.0350 | 0.0444 | 0.0436 | 0.0433 |
| c4 | 0.0218 | 0.0284 | 0.0292 | 0.0311 |
| c5 | 0.0131 | 0.0161 | 0.0174 | 0.0196 |
| c6-c14 | 0.2267 | 0.1571 | 0.2046 | 0.2796 |
| c14+ | 0.1186 | 0.0522 | 0.0861 | 0.1206 |
| c14+ NSOs | 0.0132 | 0.0001 | 0.0003 | 0.0015 |

Table 2.5. Changes in bubble point pressure with maturity of kerogen (kerogen matures from 50% conversion to 100% conversion). The original HI is 650 mg/g TOC. The bubble point of original Eagle Ford oil lies in between the bubble point of oils in presence of kerogen of 100% conversion and 75% conversion.

| Case | Temperature (K) | Bubble point Pressure (Psia) |
|---|---|---|
| Original Eagle Ford (EF) Oil | 400 | 28025 |
| EF Oil with Type II Kerogen (50% conversion) | 400 | 31290 |
| EF Oil with Type II Kerogen (75% conversion) | 400 | 29550 |
| EF Oil with Type II Kerogen (100% conversion) | 400 | 20980 |

Table 2.6. Composition of free oil when different ratios of saturated to aromatic compounds was used in the initial lumping of Eagle Ford oil (Whitson, 2012) to match compositions of Walters (2013).

| | Scenario 1 | Scenario 2 | Scenario 3 |
|---|---|---|---|
| Components | Free oil composition (x) when saturates =2*aromatics | Free oil composition (x) when saturates=1.5*aromatics | Free oil composition (x) when saturates=1.8*aromatics |
| c1 | 0.61393 | 0.62505 | 0.62506 |
| c2 | 0.07537 | 0.07673 | 0.07673 |
| c3 | 0.04366 | 0.04441 | 0.04441 |
| c4 | 0.02789 | 0.02835 | 0.02835 |
| c5 | 0.01581 | 0.01609 | 0.01610 |
| c6-c14 | 0.15444 | 0.14447 | 0.15708 |
| c14+ | 0.06888 | 0.06486 | 0.05219 |
| c14+ NSOs | 0.00002 | 0.00002 | 0.00007 |

Table 2.7. Back calculated in-situ oil compositions from produced 'free' Eagle Ford oil when in presence of Type II kerogen of 162.5 mg HC/g TOC HI. The original value of HI is 650 mg/g TOC.

| Components | Free oil compositions of Eagle Ford (mole fractions) | In-situ oil compositions in presence of kerogen of Type II (75% HI), mole fractions |
|---|---|---|
| c1 | 0.5091 | 0.2774 |
| c2 | 0.0625 | 0.0335 |
| c3 | 0.0350 | 0.0184 |
| c4 | 0.0218 | 0.0113 |
| c5 | 0.0131 | 0.0068 |
| c6-c14 | 0.2267 | 0.2295 |
| c14+ | 0.1186 | 0.1050 |
| c14+ NSOs | 0.0132 | 0.3181 |

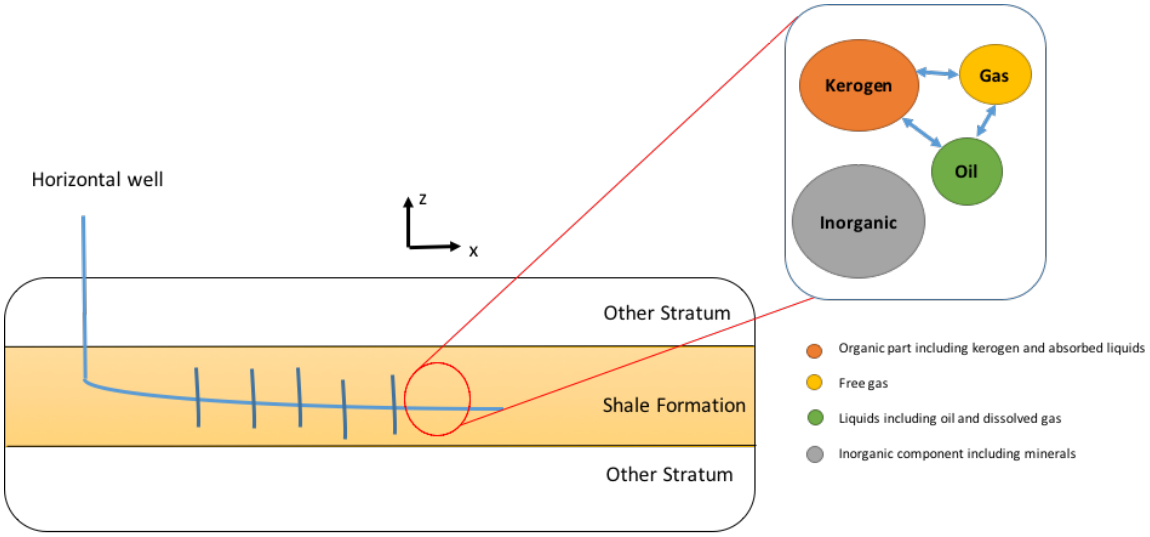


Figure 2.1. A schematic (X-Z cross section) of a multistage hydraulically fractured horizontal well used in hydrocarbon production from shales. The inset shows the fluid system – kerogen or organic matter in equilibrium with the retained oil and the expelled oil.

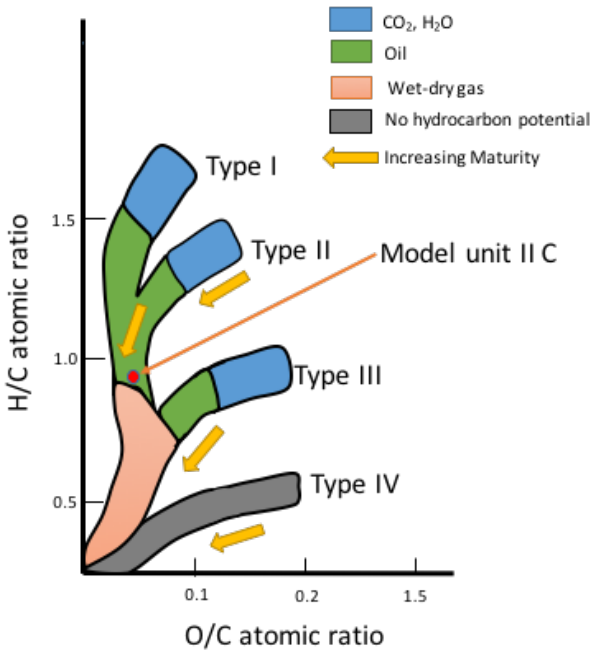


Figure 2.2. van Krevelen diagram, modified from McCarthy et al., (2011)[36]. The model unit used for molecular dynamic simulations is shown by the red dot. Type II kerogen was used in all of the thermodynamic representations.

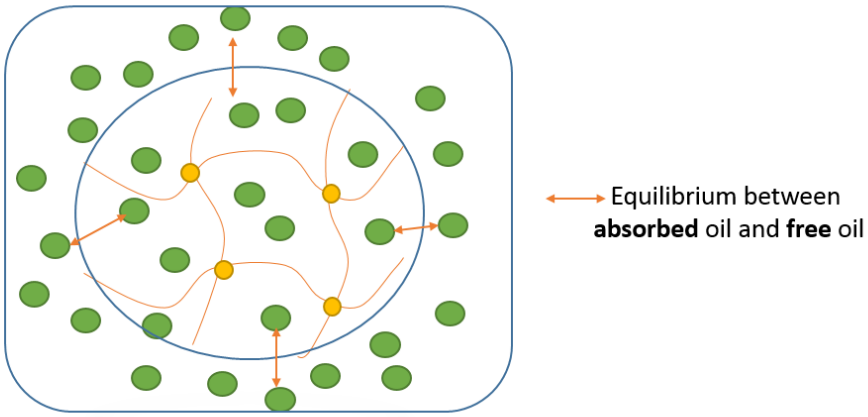


Figure 2.3. Multicomponent equilibrium between free oil and retained oil is shown schematically. The retained oil is staying inside the circular boundary of kerogen shown in the schematic. According to the hypothesis put forward in this work, it is the free oil that is produced at the surface. Kerogen is shown as a crosslinked polymer in golden color.

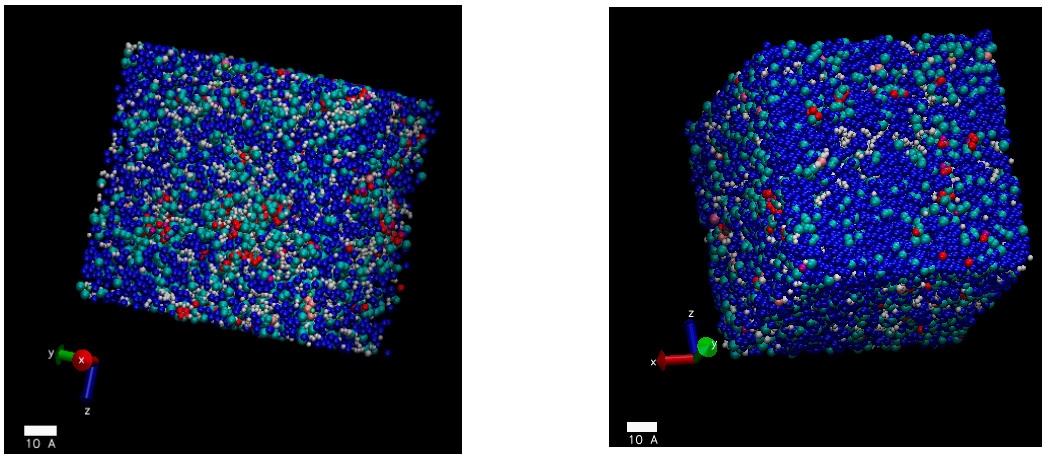


Original type II kerogen Kerogen swelled with decane (20% by mass)

Figure 2.4. Swelling of kerogen from molecular dynamics simulations. The figure on the left shows a bulk molecular model of kerogen and the figure at the right shows the same bulk kerogen swelled with dissolved decane in the matrix.

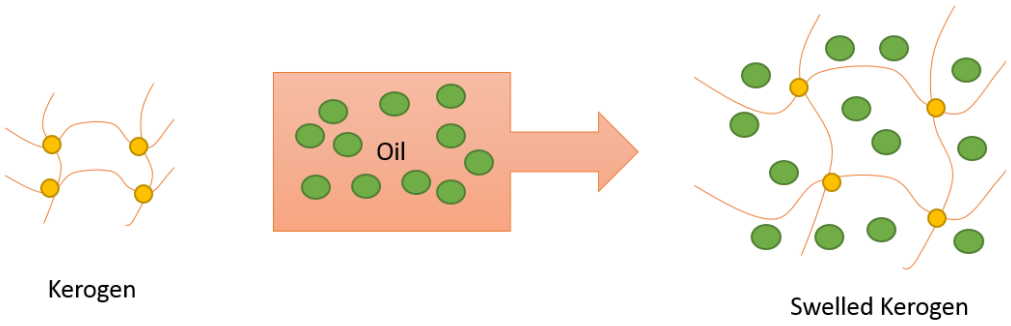


Figure 2.5. A schematic illustration of swelling of kerogen in the presence of solvent. The kerogen behaves as a crosslinked polymer that swells in presence of a solvent.

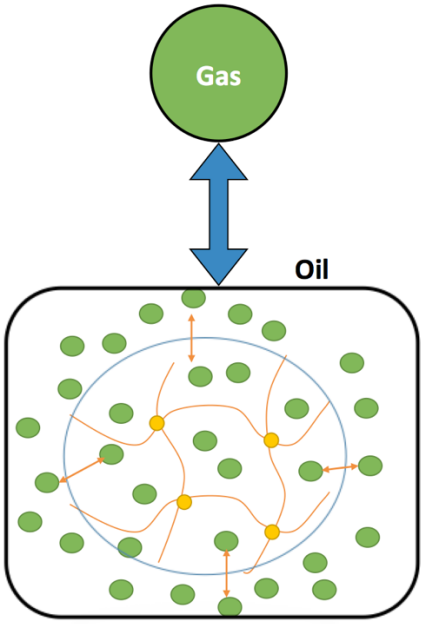


Figure 2.6. A schematic showing equilibrium between in-situ oil and gas. It is this vapor-liquid equilibrium that should be studied to calculate the true bubble point in shales. In-situ oil consists of retained and free oil. The retained and free oil phases are in multicomponent equilibrium

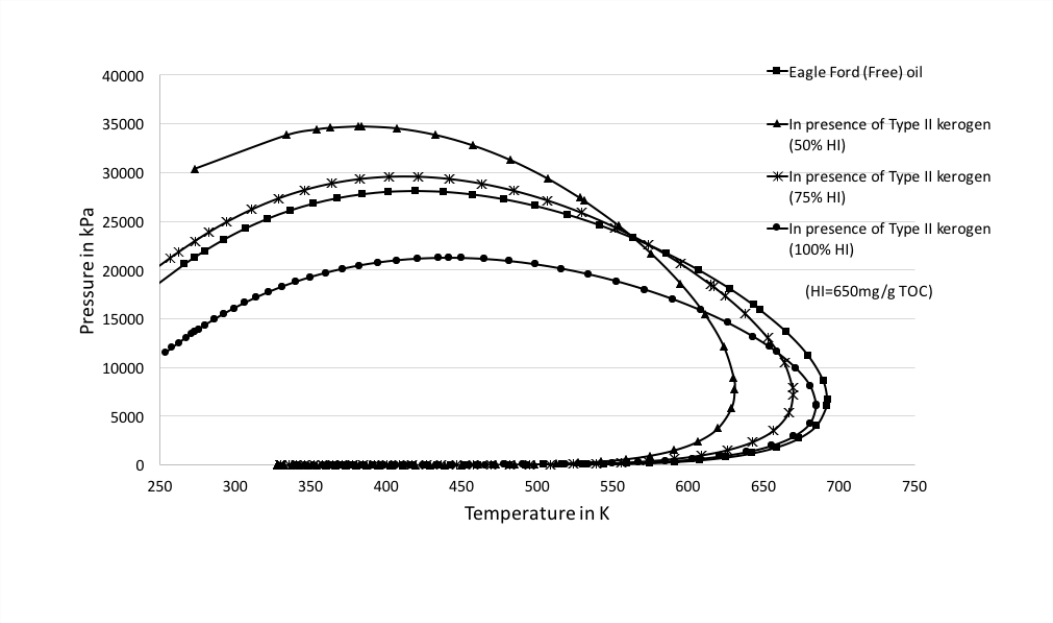


Figure 2.7. Phase envelopes (pressure-temperature bubble and dew point curves) with different maturities are shown for type II kerogen. The original HI value is 650 mg HC/g total organic content.

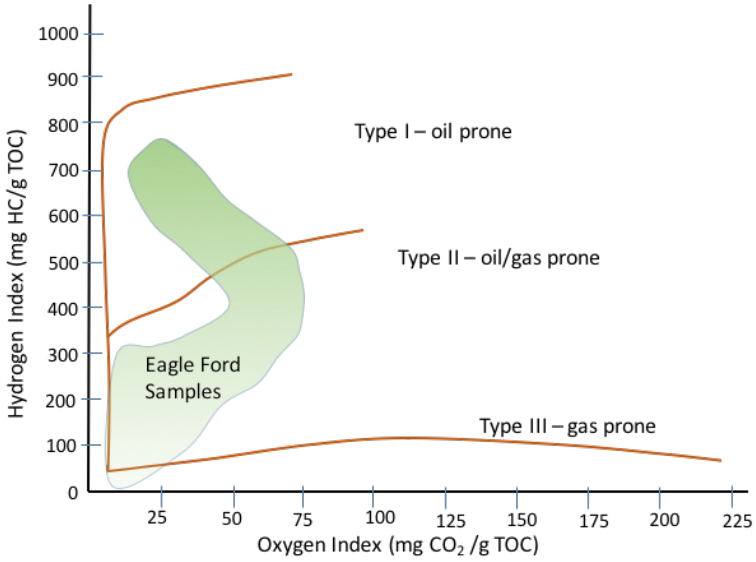


Figure 2.8. Modified Ven Krevelen diagram showing the spread of hydrogen index (HI) of kerogen for selected Eagle Ford samples (after Romero, 2014[30]). The kerogen in Eagle Ford varies in maturity ranging from 0-750 mg HC/g TOC hydrogen index.

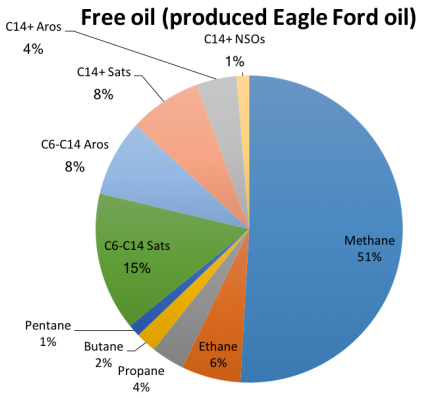


(a)

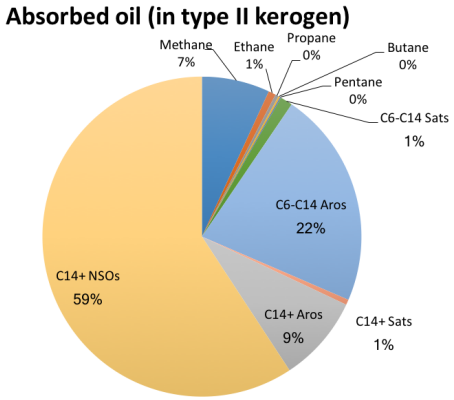


(b)

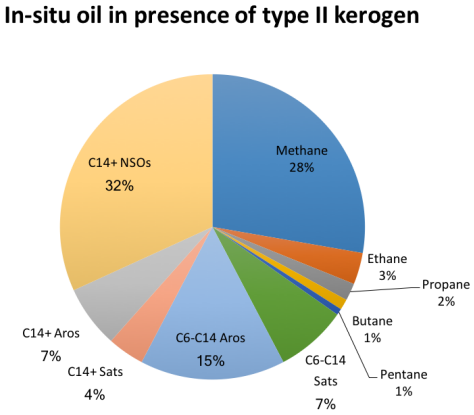


(c)

Figure 2.9. Compositions of in-situ, free and retained (absorbed) oil with Eagle Ford oil as example. The figure shows that polar and heavier components are preferentially retained in the kerogen.

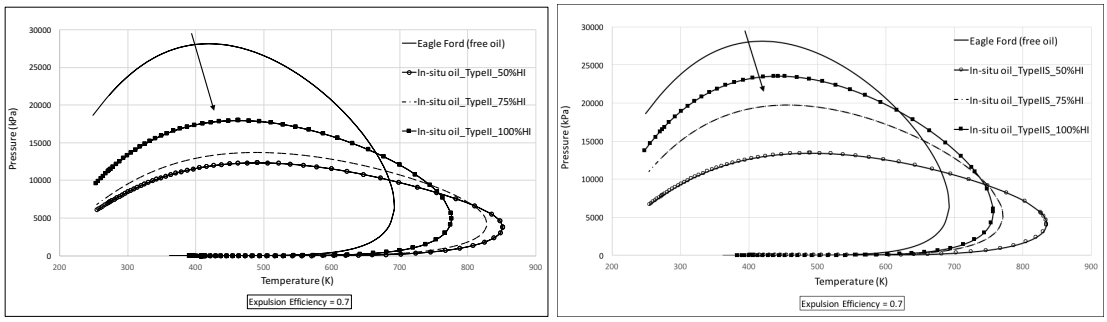


(a)

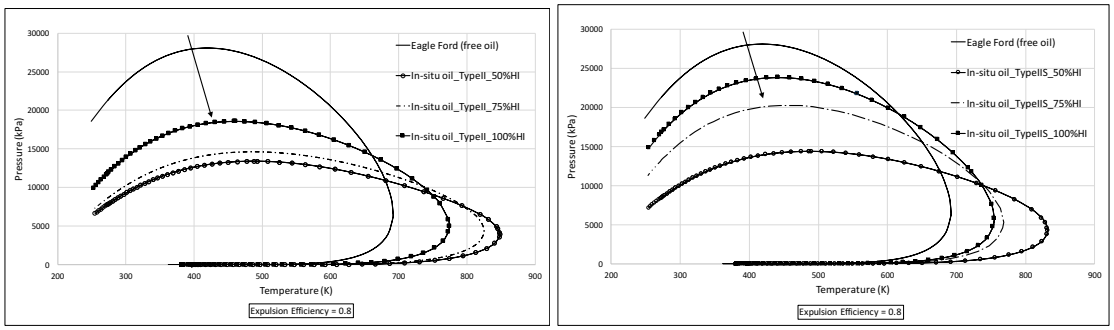


(b)

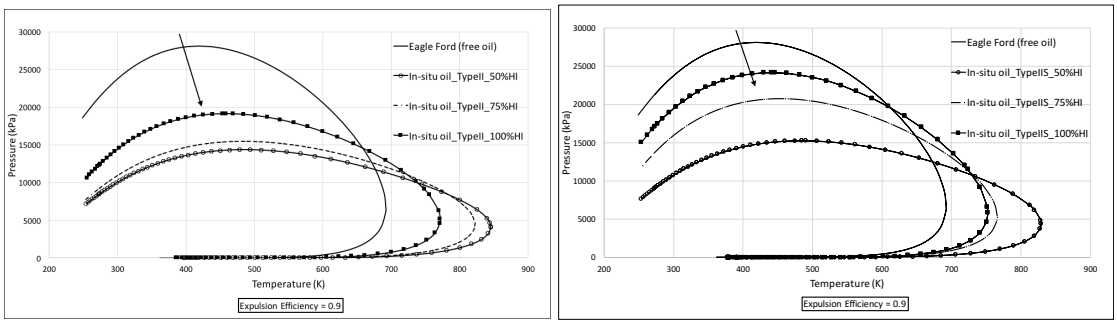


(c)

Figure 2.10. Difference in bubble point pressure of produced Eagle Ford oil and in-situ Eagle Ford oil shown in the pressure temperature plot, calculated for three values of expulsion efficiency in (a), (b), and (c). Each of (a), (b), (c) shows the PT plots for original Eagle Ford oil, in-situ oil in presence of Type II/IIS in maturity of 50, 75, 100 %HI. Arrows indicate the direction of increasing maturity of kerogen.

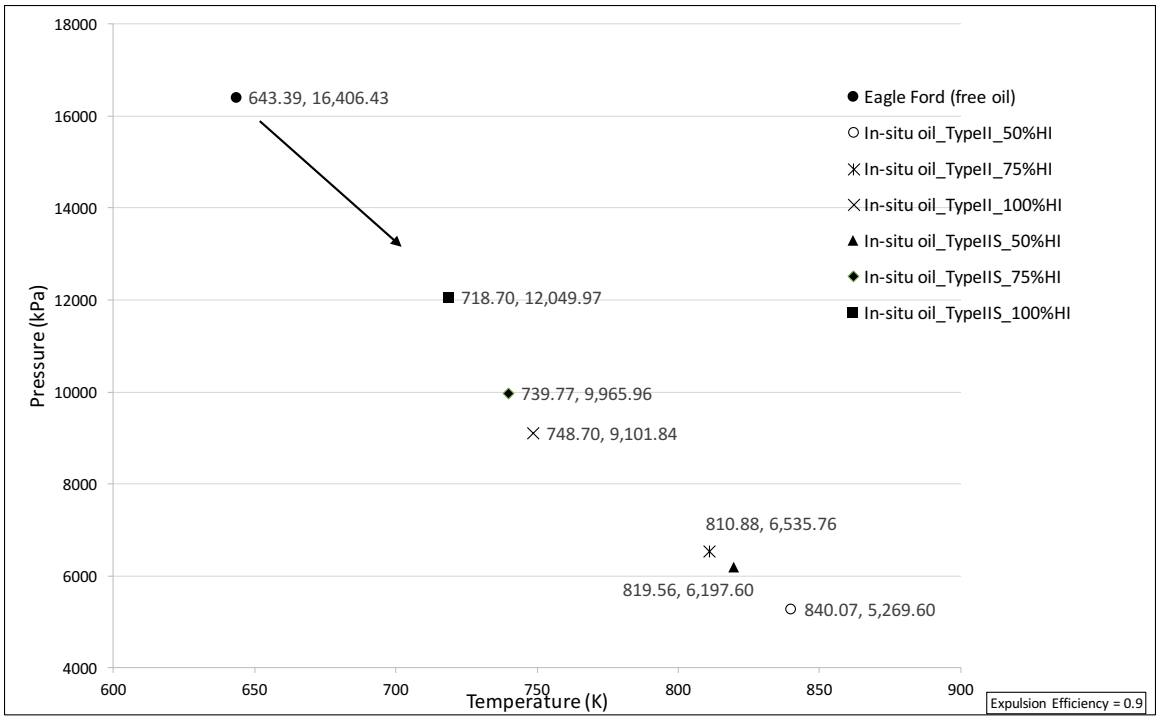


Figure 2.11. Changing critical points of oils because of interaction with kerogen of type II/IIS with maturity varying 50-100% HI at 0.9 expulsion efficiency is shown in this figure. The critical pressures of in-situ oils are less than critical pressures of free oils; however, opposite trend is observed for critical temperatures. The solid non-circular markers show the critical points of in-situ oils in presence of type IIS kerogen while the open markers show the critical points in presence of type II kerogen. It can be observed that type II kerogen causes larger suppression in critical pressures as well as larger elevation in critical temperatures of oil. However, for both kinds of kerogen, the deviations in critical properties decreases with the maturity of the kerogen. Each data label means - (temperature, pressure).

# CHAPTER 3

# KEROGEN SWELLING AND CONFINEMENT: EFFECT ON THERMODYNAMIC PROPERTIES OF HYDROCARBON FLUIDS

## 3.1 Abstract

Kerogen is organic matter found in shales which are the primary source of oil and gas deposits throughout the world. The kerogen is made up of heterogeneous complex polymer-like organic material and has been known to swell in the presence of organic solvents. The current work performs experiments and molecular simulations to understand swelling of kerogen and implications of swelling of kerogen on thermodynamic properties of hydrocarbon fluids. The effect of confinement of fluids in nanopores of kerogen was identified as well. Kerogen was isolated from whole shale samples and characterized using data from SEM, thermogravimetric analyzer (TGA), differential scanning calorimeter (DSC), and nitrogen adsorption experiments. The swelling behavior of this kerogen with decane was analyzed using simple test-tube swelling and dynamic light scattering experiments. The TGA and DSC were used to analyze the behavior of decane that was sorbed in the kerogen. Molecular Dynamic (MD) simulations were performed to assess swelling of kerogen with various solvents over a range of temperature and pressure conditions. The MD simulations reveal preferential

uptake of hydrocarbon fluids and variation in kerogen swelling in the presence of different solvents. DSC experiments were performed for oil and oil-laden kerogen to determine the effect of kerogen swelling on the oil's bubble point. The results from TGA and DSC show that kerogen suppresses the boiling point of decane due to the effect of confinement. However, the suppression is larger when oil (consider the oil as a multicomponent mixture) was used. This happened because of the effect of kerogen swelling (splitting of oil in retained and free phase and the effect of confinement combined). The experiments indicate that the kerogen changes the thermodynamic properties of fluids due to the effect of confinement and preferential uptake. This has implications on pressure-volume-temperature (PVT) properties of fluids in shale reservoirs.

## 3.2 Introduction

Kerogen is a complex, carbonaceous, heterogeneous compound, which is believed to be the precursor of oil and gas found in the subsurface. The kerogen plays a key role in storage and recovery of hydrocarbons from shale. Current techniques of exploitation of hydrocarbons from shales leave over 80% of generated hydrocarbons in the subsurface[37]. Based on the elemental H/C and O/C ratio, the kerogen is classified to be primarily of IV types with each of the type I-III being in the oil or gas window according to their maturity. Type IV designates an over-mature kerogen, resembles coal, and has minimum potential to generate hydrocarbons (Figure 3.1).

To perform experiments, a type I kerogen was isolated from Green River Formation Shale. This kerogen sample was then analyzed with a scanning electron microscope (SEM) and Thermogravimetric analyzer (TGA). The TGA data (Figure 3.2) show that the

isolated kerogen is over 75% organic matter based on the mass loss below 500 $^{o}$C. The pores found in isolated kerogen, as evident in its SEM image (Figure 3.3), have dimensions in the nanometer range as has also been observed by other authors[3]. The nitrogen isotherm (Figure 3.4a) of the isolated kerogen has a hysteresis throughout the relative pressure range of 0.1 to 1.0. The Brunauer–Emmett–Teller (BET)[38] specific surface area of the isolated kerogen is 13.37 m²/g, and the average pore size calculated by Barret-Joyner-Halenda (BJH)[39] method from desorption data is 17.69 nm (Figure 3.4b). These nanopores constitute organic porosity in shales. Hydrocarbon gases and liquids in the kerogen pores and adsorbed on the wall of kerogen may be absorbed in the kerogen leading to expansion in kerogen volume. Such swelling in kerogen is much like swelling of coal with the exception that kerogen swelling has nonspecific interactions. These sorbed hydrocarbons in the kerogen can be a potential hydrocarbon source that is still untapped. The swelling behavior of kerogen in the presence of hydrocarbons fluids, at reservoir conditions, was therefore thought to be of importance and studied in this work.

The experiments were designed for a binary mixture of kerogen and decane to understand the change in the thermodynamic properties of the sorbed decane. To do this, swollen kerogen samples were prepared by fully saturating kerogen in decane by keeping the two together for 24 hours. Twenty-four hours was chosen because no further swelling response was observed after 24 hours, as also pointed out in previous swelling studies[6,10–15,40,41]. A swelling ratio ($Q_v$) is defined as the ratio of the volume of swollen kerogen to the original volume of kerogen. The kerogen absorbed the decane and swelled in volume over 24 hours. Traditional test-tube swelling experiments were performed on this kerogen and decane by recording the height of the kerogen bed in a flat bottom test-tube before

and after swelling with decane. Dynamic Light Scattering (DLS) experiments were performed on kerogen particles before and after swelling (Figure 3.5).

MD simulations are useful since experiments are difficult to perform at the high pressures that are usually seen in the subsurface. Ungerer et al. (2015)[16] have developed realistic kerogen models that are used in this work to perform molecular dynamic simulations of kerogen with organic solvents. These simulations are performed at reservoir temperature and pressure on a model of type II kerogen to understand its swelling in presence of 17 organic solvents chosen in this study

TGA and DSC experiments were performed on sorbed decane and pure decane as well as on oil and sorbed oil to investigate the effect of kerogen sorption (and therefore its swelling) and effect of confinement on the thermodynamic properties of the fluids. The oil was collected from Dakota Formation in Clay Basin Field, Daggett County, Utah. The sorbed decane sample consisted of swollen decane-laden kerogen. The TGA and DSC for pure decane and sorbed decane were run in the temperature regime where kerogen is inert based on the TGA and DSC runs for kerogen performed earlier (refer to Figure 3.2 for TGA and the results section for DSC). The DSC runs were also performed for the oil and kerogen-oil binary mixture to understand the effect of preferential swelling of components by kerogen and its effect of the thermodynamic properties of the oil absorbed by kerogen. The MD simulations revealed preferential swelling of kerogen based on the hydrocarbon solvent used (Figure 3.6). Assuming oil as a mixture of multicomponent hydrocarbons, the preferential swelling of kerogen would change the composition of the absorbed phase, thereby changing the PVT behavior of the absorbed oil. The pure-decane and kerogen experiments revealed the effect of confinement.

However, the oil and oil-kerogen DSC experiments revealed the combined effect of preferential swelling of kerogen and effect of confinement.

## 3.3 Method

### 3.3.1 Experimental

Kerogen was isolated from the whole rock sample by series of acid treatments based on previous kerogen isolation work[42–47]. The kerogen was extracted from Green River Formation- skyline 16 core. The average organic matter in powdered oil shales were estimated to be 11.5% weight of the total oil shale[48]. Based on Elemental analysis[48], this kerogen falls in type I oil shale category on the van Krevelen classification diagram.

First, the carbonate minerals are removed by treating 2.5 grams of shale rock with 30 ml of 5N HCl for 48 hours. The remaining 1.0 g of the residual rock is treated with 10 ml of 12N HCl and washed with 10 ml of DI water. The residual rock was heated in a vacuum to 110 $^{o}$C and was ready for the next step which was removal of pyrite minerals. To remove the pyrite minerals, if any, from the residual rock, it was treated with 20% (wt) $HNO_3$ for 48 hours followed by wash with DI water and oven dry. The dry residual rock was then treated with 5N HCl followed by 25 ml of 48% (wt) HF for 48 hours. The residual was washed with DI water followed by oven drying. The weight of the rock at each step was documented. In order to calculate the amount of organic and inorganic matter left in the residual rock, thermogravimetric analysis (TGA) was performed on the residual rock sample. The TGA data revealed that over 75% of the residual sample (powder form) is organic. The experiments with kerogen and kerogen-decane binary mixture were designed using differential scanning calorimeter (DSC) and thermogravimetric analyzer (TGA) as shown in Figure 3.7 and Figure 3.8, respectively.

First, 60 mg of kerogen sample is dried at 105-110 °C for 1 hour in an oven and cooled overnight in a vacuum oven until shortly before the swelling experiments. Three samples of 10 mg kerogen each are treated with excess decane in a mini-centrifuge tube and three others are packed in airtight tubes. The tubes with kerogen-decane are centrifuged at 6000 rpm for 3 cycles of 5 min duration each. The mixture is kept in a flat bottom test tube. The initial height of kerogen (h1) in the tube is measured by a Vernier caliper after the third centrifuge cycle. The sample is left for 24 hours and the sample height is measured again (h2). Swelling of kerogen was calculated using the test tube method as $Q_v$ = h2/h1. The three swollen samples are then used for further experiments. Differential scanning calorimetry and thermogravimetric analysis are performed for the original kerogen and the swollen kerogen to measure the boiling point of sorbed decane. Dynamic Light Scattering for particle size analysis was performed using on original and swollen kerogen and the results were compared.

For the differential scanning calorimeter, excess solvent layer in tubes that is accumulated over the swollen kerogen bed is removed and the sample is transferred to DSC pans. Weight of each empty DSC pan is measured. Experiments were performed under atmospheric pressure with an inert gas (nitrogen) flow rate of 40 mL/min. Before each measurement, the DSC cell was purged with inert gas (nitrogen) for at least 10 min. Hermetically sealed and pierced samples were cooled to −120 °C at a rate of 5°C/min, equilibrated at −120 °C for 10 min, and then heated to 200°C. At 200 °C, the temperature remained constant for 10 min before stopping the run. This procedure was repeated to run DSC for pure decane (to compare with absorbed decane) as well as for Clay Basin oil (Figure 3.9). Similarly, the kerogen and kerogen-decane samples were analyzed in the

thermogravimetric analyzer. The samples were treated at a ramp-rate of 5°C/min and the weight of the samples decreased as the temperature was increased due to the loss of volatiles. A weight loss curve was obtained from the thermogravimetric data.

Each of the DSC runs discussed above were preceded by the 'Baseline' run. The baseline is the response with both crucibles empty in the DSC, yielding a signal bias inherent in the system[49]. This 'Baseline' allows removal of system bias from the data. Further, the DSC was calibrated using the standard procedure laid out in ISO 11357-1[50]. The uncertainties could be estimated to be not more than 0.3 K and 0.5% which are defined by ISO 11357-1 for temperature and sensitivity calibrations, respectively. The repeatability error is the smallest possible uncertainty of measurement of calorific measurements[51].

### 3.3.2 Modeling

The current modeling work involves using xyz coordinates of atoms in one of the published kerogen models[16] (Figure 3.10) and assigning parameters using the General Amber Force Field (GAFF)[17]. GAFF has been modified from the Amber Force Field to include organic molecules. A remodeled kerogen structure was then used to measure the bulk properties of kerogen, including swelling in presence of different organic solvents, by performing Molecular Dynamics (MD) simulations. A MD modeling workflow has been developed (discussed in supplementary information) to study kerogen-hydrocarbon interactions using the GAFF implemented in the Large-scale Atomic/Molecular Massively Parallel Simulator (LAMMPS)[21] tool. The density of kerogen and probability distribution function of the C-C bond lengths were calculated. Volumetric swelling of kerogen in the presence of organic solvents was studied to understand the interaction of

kerogen and fluids. The force field GAFF was originally developed to model organic molecules. The bulk kerogen model was created after a systematic simulated annealing procedure of 10 individual kerogen molecules. A relaxed bulk kerogen model in its native state was then used to determine properties like density of bulk kerogen, and swelling of kerogen with solvents.

Pair-wise radial distribution function (g(r)) and density of the relaxed structure were calculated to validate the kerogen model. A plot of radial distribution function (Figure 3.11) was produced after simulated annealing, during the process of production run at 300 K and 300 atmospheres which matched the radial distribution function for the same kerogen model in previous works[16,52]. The density of annealed structure of modeled kerogen was around 1.18 g/cc at 300 K and 300 atmospheres pressure. The density from simulations (Figure 3.12) matches densities obtained from experiments[22] (1.18-1.29 g/cc) and simulations[16] (1.13 g/cc).

Once the density and radial distribution function of the kerogen model used in this study are found to reasonably match with results from previous works, the kerogen model at its relaxed state could be used to measure extent of swelling of kerogen in presence of different organic solvents. To calculate volumetric swelling (swollen volume/native volume) of kerogen in presence of organic solvents, the kerogen was annealed together with the solvent molecules. The molecular dynamics simulations of the kerogen model in NPT ensemble and periodic boundary conditions were performed with 20% solvent saturation by mass of bulk kerogen (10 molecules of kerogen of molecular mass of 3465 Daltons each). The simulations were carried out in LAMMPS in a 100-Å cube with periodic boundary conditions in all directions. The simulated annealing was carried out

using the procedure mentioned in 'Simulated Annealing Procedure' section in the supplementary information of this chapter. The volume and energy of the system were reduced to the minimum at 300 K and 300 atm. To calculate the volumetric swelling, the final volume of the relaxed system of kerogen and solvent (Figure 3.13) at certain temperature and pressure was compared with that of a relaxed system of pure kerogen.

## 3.4 Results

The $Q_v$ for kerogen calculated from the test-tube swelling experiments with decane was 1.23. This is close to earlier test-tube kerogen swelling experiments performed with decane [6,10–15]. The DLS results also showed considerable kerogen swelling. The DLS works on the principle of finding particle diameter by the diffusion coefficient in the media (decane in this case) using Stokes Einstein's relation. The diffusion coefficient is calculated from the scattering of the light from the suspended particles. $Q_v$ for kerogen with decane calculated by DLS is higher than the test-tube experiments possibly because DLS measures hydrodynamic radius of the particles.

MD simulations were performed to assess the swelling of kerogen with different solvents. MD swelling ratio for decane (approx. = 1.23) matched well the swelling ratio obtained from test-tube swelling experiments performed by the author as well as other researchers on type II kerogen at room temperature and pressure. Different swelling ratios were observed based on the nature of solvent (aromatic or aliphatic, heavier or lighter). The swelling simulations allow the swelling of kerogen to be calculated with gases and at higher pressures which are difficult in a laboratory. The swelling of kerogen in high pressure (300 atm) resembles the in-situ shale reservoir conditions and most of the US shales that are generally over-pressured. The MD simulations reveal that the

swelling of kerogen slightly increases as the temperature and pressure of the kerogen-solvent system were increased. This would have implications on the original oil-in-place or gas-in-place depending upon different contributions from the absorbed hydrocarbon phase in the shale rocks.

Differential scanning calorimeter (DSC) results showed a different vaporization temperature for decane with and without swollen kerogen. The vaporization of decane (shown by the peaks in the heat flow rate in Figure 3.7) was suppressed by the kerogen matrix as indicated by suppressed onset temperatures for vaporization. The liquid decane in kerogen was vaporized at almost 7.8 $^{o}$C earlier than the temperature of vaporization of same decane without kerogen (Table 3.1). Similarly, melting and crystallization were suppressed by the presence of kerogen (Table 3.2). Decane present in nanometer pores also forms a fraction of the overall decane present in the swollen kerogen sample. However, there is no clear distinction between decane sorbed by the kerogen matrix and decane in pores that are large enough (nanometer scale) for some of the decane to behave like confined bulk decane. The kerogen with 17 nm avg. pore size gave results of suppression in bubble point temperature (7.8 K suppression) which are in between the suppressions seen by Luo et al. (2016) in CPG of 38.1 nm (1-4 K suppression) and 4.3 nm (15-25 K suppression) at room pressure conditions. The bubble point was assumed to be at the temperature of onset of the endothermic peak associated with vaporization and melting and onset of exothermic peak in crystallization. This onset was determined as the point of intersection of the tangent line at the point of greatest slope on the leading edge of the peak with the extrapolated baseline. Different weight loss curves were obtained for decane with and without kerogen in TGA. The TGA data showed that the decane sorbed

in kerogen was vaporized earlier than the pure decane as seen in the Figure 3.8. The swelling of kerogen has key implications on expulsion studies from kerogen as well as on the original-hydrocarbon-in-place. Kerogen is shown to swell by absorbing oil (which can be considered as a mixture of organic solvents). The absorbed oil fraction has important influence on pressure-volume-temperature (PVT) properties of oil in the kerogen-rich shales. From the preferential swelling of kerogen seen with different hydrocarbon components in Figure 3.6, it was hypothesized that the DSC conducted on oil (assume as multicomponent mixtures) and kerogen would largely change the bubble points of the absorbed oil as different components of oil will be absorbed in different amounts. This will lead to change in the composition of sorbed oil from the original composition of oil. To confirm this hypothesis, the test-tube swelling experiments and experiments with DSC were performed on oil and kerogen-oil binary mixture. Test-tube swelling experiments revealed that after over 24 hours, the kerogen swelled 1.6 times due to absorption of oil.

It was observed from the DSC experiments (Table 3.3) that a suppression of over 50$^{o}$C was seen in the bubble point temperature of the oil absorbed in kerogen compared to that of the pure oil. This suppression includes the effect of confinement and the effect of swelling of kerogen (splitting of phase by absorbing oil components selectively). Therefore, both confinement and kerogen swelling affect the bubble point of oils but to a different extent. Swelling of kerogen suppresses the bubble point to a greater extent than confinement. This is because swelling changes the composition of absorbed oil, while the pore wall proximity affect is because of dominant surface forces that are important but not as large as the effects due to changes in composition.

Accurate bubble points are essential in predicting the true rates and recoveries from shale plays. Shifts in the bubble points may delay gas production and would allow improvements in recovery of liquids.

## 3.5 Conclusions

The concept of preferential absorption of different solvents has been noted earlier[25] by Flory Rehner Theory, experiments[11–14,34,40,53,54], and by MD simulations in this work. This means that both type I and II kerogen preferentially uptakes some components of oil more than others and shows a bulk swelling that can be calculated in terms of $Q_v$. A $Q_v$ of 1.6 was observed in kerogen of type I swelled with Clay Basin oil. This fractionation of oil by kerogen splits oil into absorbed and free phase. The absorbed phase stays in the kerogen matrix while the free phase may stay in the nanopores of kerogen. Because of different compositions of free and observed phase, the absorbed oil behaves differently. The pore-wall – fluid interactions have another effect (effect of confinement[55–64]) on the fluid thermodynamic properties of the confined free fluid. Clay Basin oil absorbed in kerogen has a bubble point which is suppressed by around 50$^{o}$C from the original bubble point of pure oil (Figure 3.9). This suppression is due to combined effect of partitioning by kerogen and confinement of unabsorbed oil (confined free oil). A wider peak of kerogen-oil sample in DSC as opposed to sharper peak of pure oil also indicates that there are two effects that suppressed the bubble point of oil in Figure 3.9. The use of pure component such as decane in DSC, however, negated the effect of partitioning as there is just one component that cannot be partitioned based on the composition. Absorbed phase and free phase in this case are both pure decane. Hence, only the effect of confinement was present that caused the suppression of only around 7.8$^{o}$C in the boiling point of

decane when it was with kerogen compared to the boiling point of pure decane. Therefore, both kerogen partitioning and confinement changes the boiling point temperatures of hydrocarbon fluids; however, the effect of kerogen partitioning is more dominant. Swelling of kerogen suppresses the bubble point to a greater extent than confinement. This has implications on pressure-volume-temperature (PVT) properties of in-situ oil (sum of absorbed and free phase oil) in the kerogen-rich shales. The correct bubble points are essential in predicting the true rates and volumes of recoveries from shale plays and must be calculated by accounting for the two effects discussed here. Shifts in the bubble points may delay gas production and would allow improvements in liquid recovery.

## 3.6 Supplementary Information

### 3.6.1 Methodology for Molecular Dynamic Simulations

A method has been developed in current work to form molecular structure of bulk kerogen from a single molecule. A simulated annealing procedure was performed on a group of several kerogen molecules using the force field GAFF which was originally developed for molecular dynamics simulations of organic molecules[17]. In the current work, the application of GAFF has been extended from simpler organic molecules to complex organic mega-molecules like kerogen. The type II C kerogen model was chosen from Ungerer et al. (2015)[16]. The chemical formula of Model II C is $C_{242}H_{219}O_{13}N_5S_2$ with 481 total number of atoms in one molecule. The H/C and O/C ratios of this model unit are 0.905 and 0.054, respectively, and plots in the middle –end of the oil window as shown in Figure 3.1. The force field parameters for GAFF were chosen from Wang et al. 2004[17] and 'gaff.lt' file available in the Moletemplate[65] software distribution. The

Gasteiger-Marsili[66] charges were assigned to all the atoms using the Avogadro molecular modeling tool[67].

In order to perform MD simulations, a workflow was developed comprising a series of steps as shown in Figure 3.14. The steps are discussed below:

1. First, a molecule of type II C kerogen was converted from xyz format to protein data bank (PDB) format. A single kerogen model II C is shown in Figure 3.13.

2. An atomtype program of Ambertools[68] was used to convert the file into GAFF friendly PDB

3. Packmol (Martinez L, 2009) tool was used to randomly stuff 35 of these GAFF versions of PDB into a simulation box (Figure 3.10)

4. Visual Molecular Dynamics, VMD[20] tool to produce an input file for LAMMPS[21]

5. Manually enter the bond, angles, and dihedrals parameters for all the atoms from gaff.lt file from Moletemplate[65]

6. An instruction file for LAMMPS was written which included a series of simulated annealing steps

7. The simulations for simulated annealing, followed by production runs, were run in the LAMMPS in parallel with multiple processors of a super computer

8. Properties were calculated after simulated annealing of kerogen. Production simulations were run in relaxed kerogen structure to calculate swelling, radial distribution function, and density of kerogen

9. VMD was used to visualize the final relaxed structure of pure kerogen and kerogen with octane (Figure 3.13).

### 3.6.2 Simulated Annealing Procedure

In order to relax the system to minimum energy state, the bulk kerogen structure made up of 10 molecules systematically went through a series of energy minimization steps. The initial packing density of kerogen in a 100Å cube was 0.206 g/cc. First, the structure was simulated in canonical ensemble (NVT) with gradually increasing temperature until 2000K, for 0.2 ns. Following NVT ensemble, the system was simulated in isothermal-isobaric (NPT) ensemble steps for a total time of 1.4 ns, which consisted of 5 smaller steps of range 0.25-0.28 ns each. In these five steps, the system went through the highest temperature and pressure of 2000 K and 1000 atm, respectively, to minimum of 300 K and 300 atm towards the end of run in a step-wise reduction of temperatures and pressures. The final temperature was chosen close to reservoir conditions in order to replicate the realistic in-situ conditions for kerogen. A schematic of all the annealing steps is given in Figure 3.14. For any NPT or NVT cycle of over 0.2 ns, the time steps varied from 0.0001 to 0.01 ns. The Nose-Hoover style non-Hamiltonian equations of motion were used in the LAMMPS molecular simulator to generate positions and velocities sampled from the canonical (NVT) and isothermal-isobaric (NPT) ensembles with periodic boundary conditions in all directions. The density of the final kerogen structure was calculated at the end of simulated annealing. The final annealed structure of bulk kerogen at minimum energy state would be used to further measure swelling of kerogen in presence of organic solvents.

Table 3.1: Onset temperature of crystallization melting and vaporization of pure decane and decane in kerogen

| Sample | Onset of crystallization ($^{o}$C) | Onset of melting of solid ($^{o}$C) | Onset of vaporization ($^{o}$C) |
|---|---|---|---|
| **Pure decane** | -35.8 | -29.0 | 167.8 |
| **Pure decane in kerogen** | -39.9 | -30.2 | 160.0 |

Table 3.2: Peak temperature of crystallization melting and vaporization of pure decane and decane in kerogen

| Sample | Peak of crystallization ($^{o}$C) | Peak of melting of solid ($^{o}$C) | Peak of vaporization ($^{o}$C) |
|---|---|---|---|
| **Pure decane** | -38.9 | -24.5 | 171.6 |
| **Pure decane in kerogen** | -40.2 | -25.9 | 168.7 |

Table 3.3: Onset temperature of vaporization of Clay Basin oil and Clay Basin oil absorbed in kerogen

| **Sample** | **Onset of vaporization ($^{o}$C)** | **Peak of vaporization ($^{o}$C)** |
|---|---|---|
| **Oil** | 176.1 | 180.1 |
| **Oil in kerogen** | 122.4 | 143.9 |

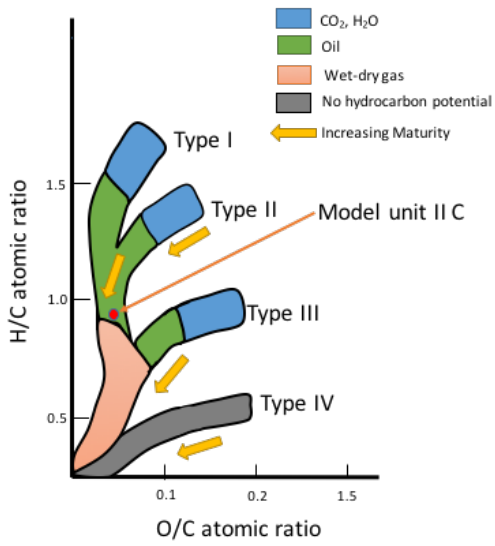


Figure 3.1. van Krevelen Diagram showing the IV types of kerogen. The kerogen can be classified into IV types based on their origin. Each class could generate hydrocarbons based on the maturity of the kerogen. The red dot shows the type of kerogen used for Molecular Dynamic simulations later in the text. The plot is redrawn after work of McCarthy et al. (2011)[36]

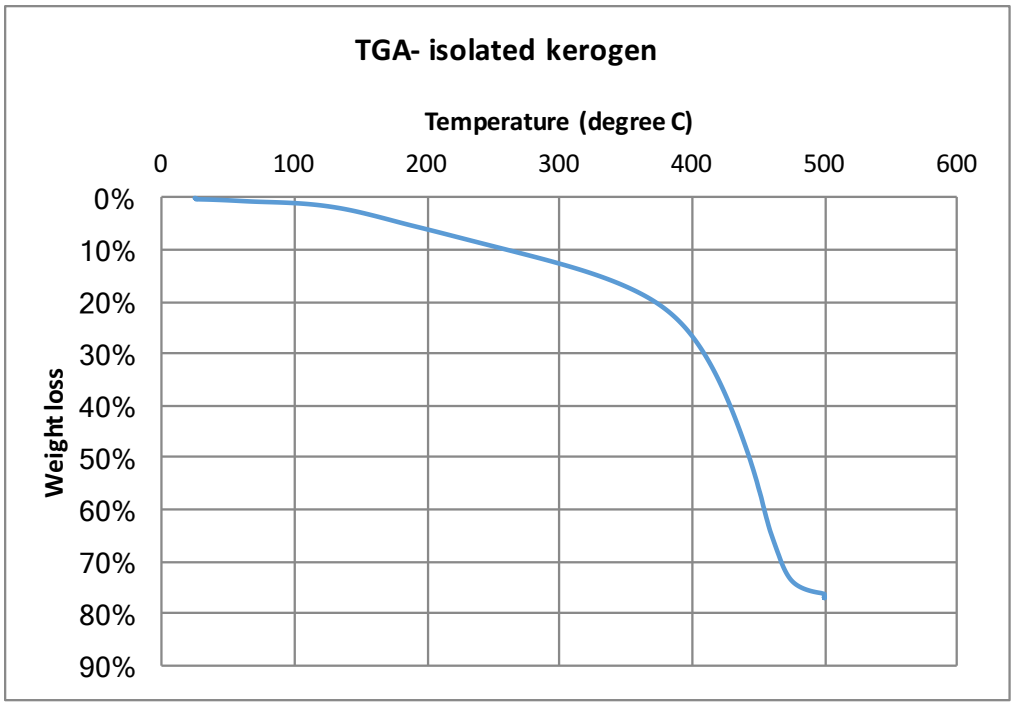


Figure 3.2: TGA data showing the weight loss curve of kerogen and that the isolated kerogen consists of over 75% organic matter

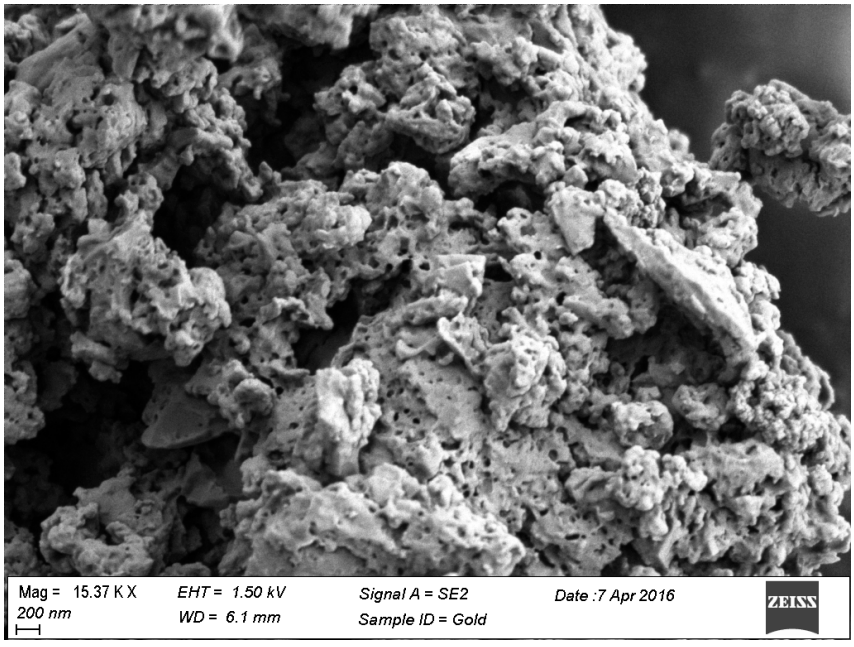


Figure 3.3: Scanning Electron Microscopy (SEM) image showing presence of sub-micron pores in isolated kerogen of original mesh size of 100 µm

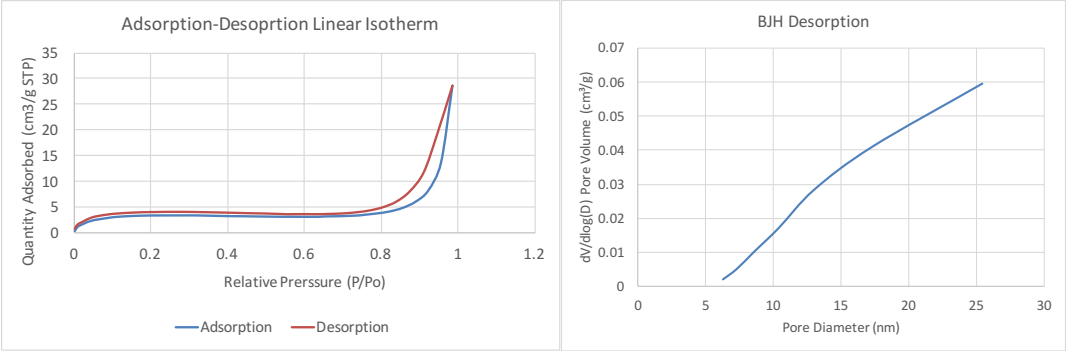


Figure 3.4: Nitrogen adsorption-desorption isotherm on the left shows a hysteresis loop throughout the relative pressure range. The graph on the right shows the average pore diameter of 17.691 nm (range 6-25nm) in the BJH desorption.

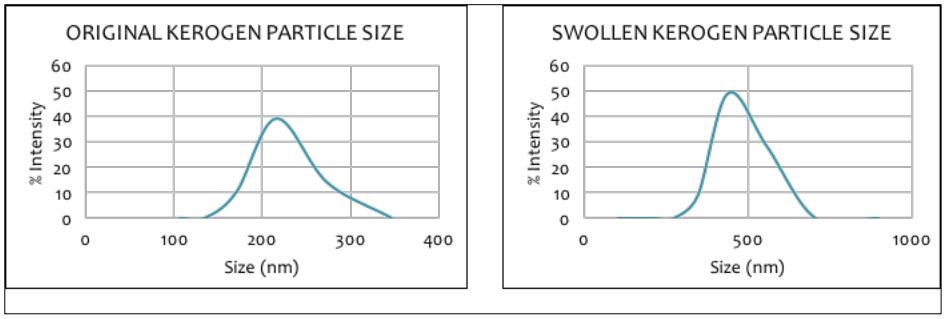


Figure 3.5: Swelling was seen in dynamic light scattering (DLS) in the kerogen particle kept with decane for 24 hours. The median raddi increased from 215.7 nm to 439.9 nm.

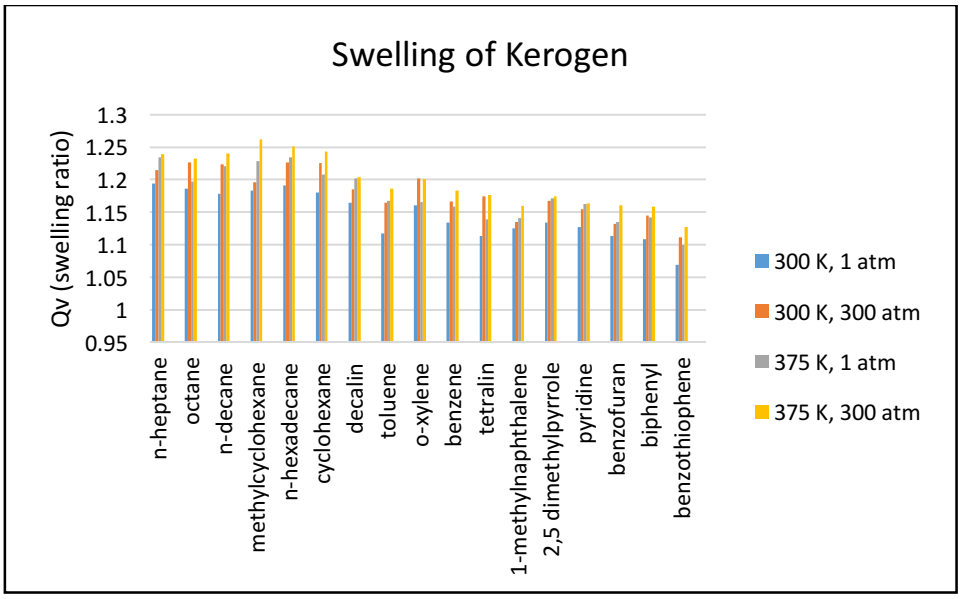


Figure 3.6: The annealed kerogen matrix swelled while performing NVT simulations with series of solvents as shown here. The swelling ratios of type II kerogen (medium to high maturity) in presence of 17 solvents at different temperatures and pressures is shown in the bar graph with number of solvents. The kerogen swells more at higher temperatures and pressures.

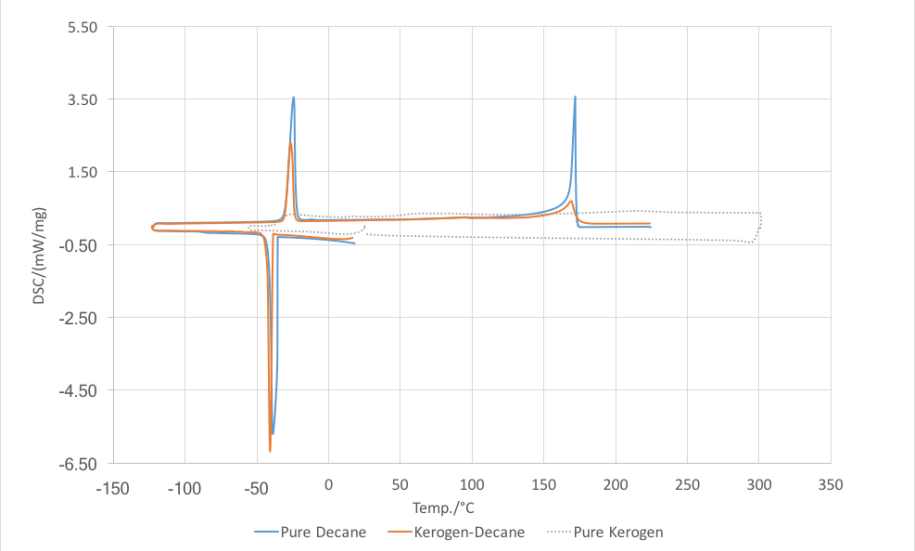


(a)

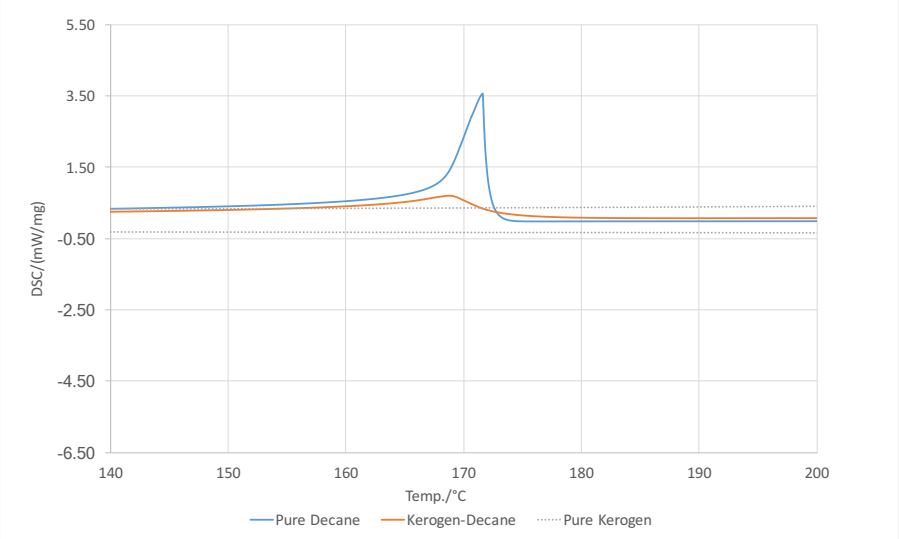


(b)

Figure 3.7: DSC results for kerogen and pure decane experiments. (a) DSC data show that the decane absorbed in kerogen boils, melts, and crystalizes at lower temperatures than decane in the bulk state. (b) Boiling point peak is enlarged to see the fine difference in the DSC peak of pure decane and decane absorbed in kerogen.

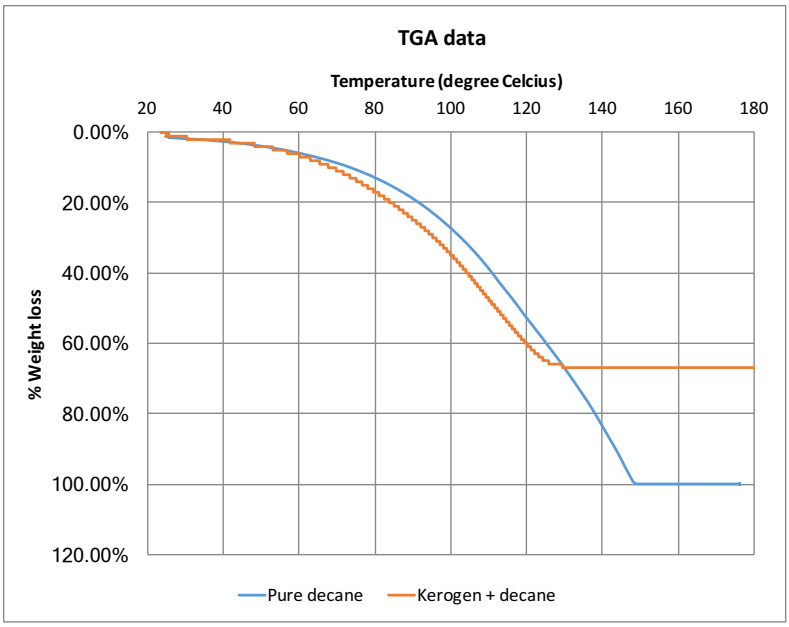


Figure 3.8: TGA data showing that kerogen interacts with decane and changes the boiling point of the decane in the presence of kerogen.

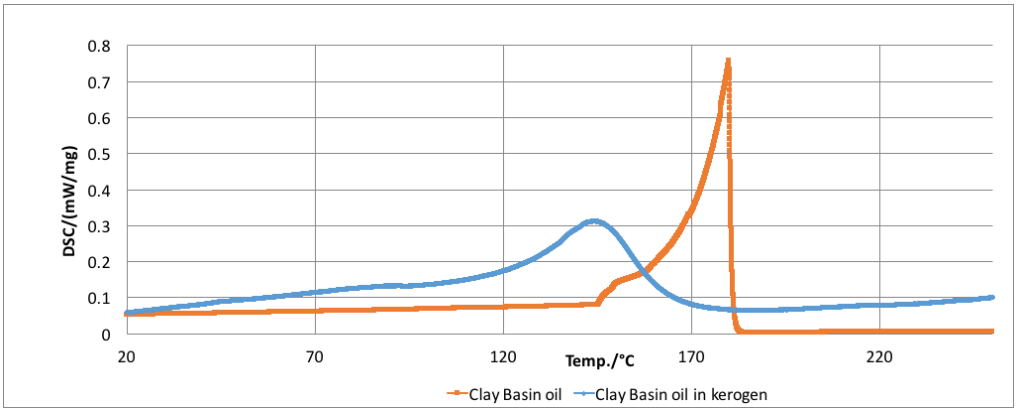


Figure 3.9: DSC data showing that kerogen absorbed oil and changed the bubble point of the absorbed oil

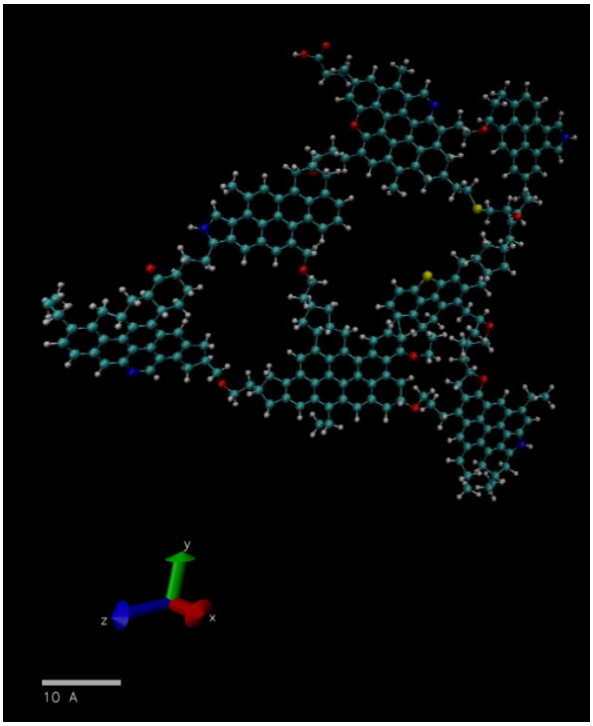


Figure 3.10: Single molecule of type II kerogen taken from Ungerer P. et al. (2015)

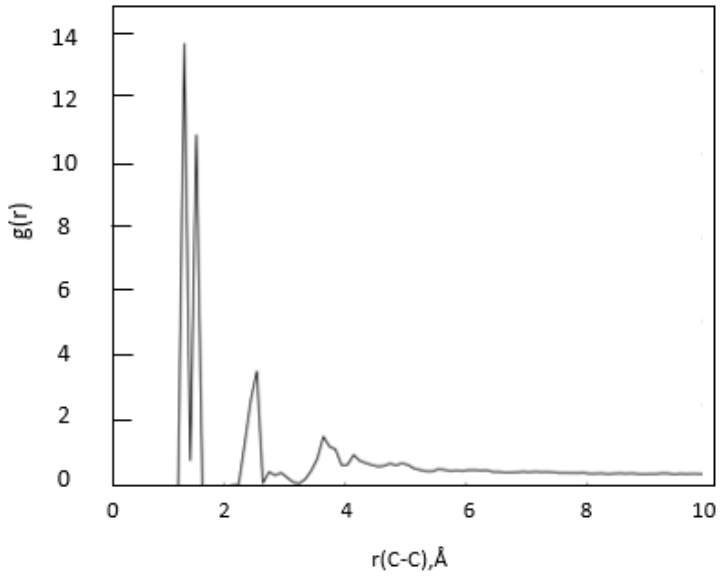


Figure 3.11: Plot of pair-wise radial distribution function

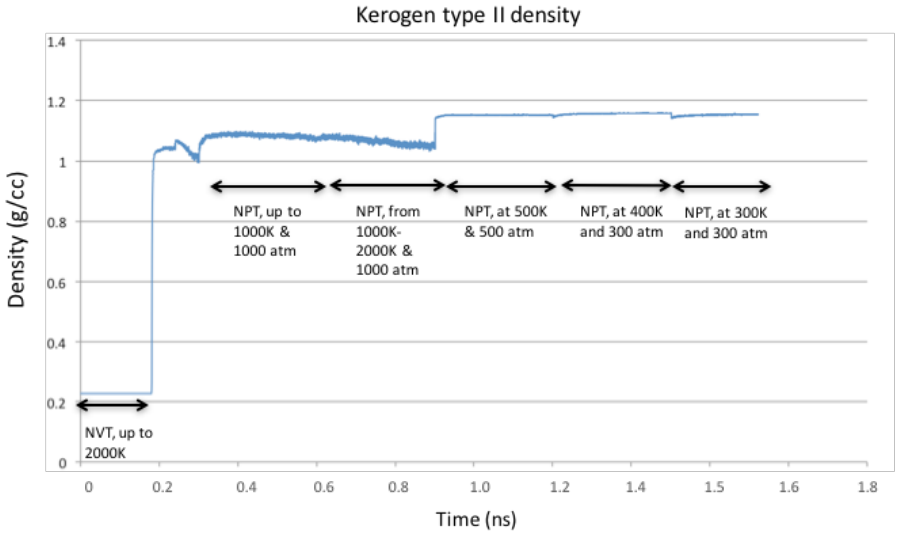


Figure 3.12: Density of kerogen calculated from Molecular Dynamics Simulations

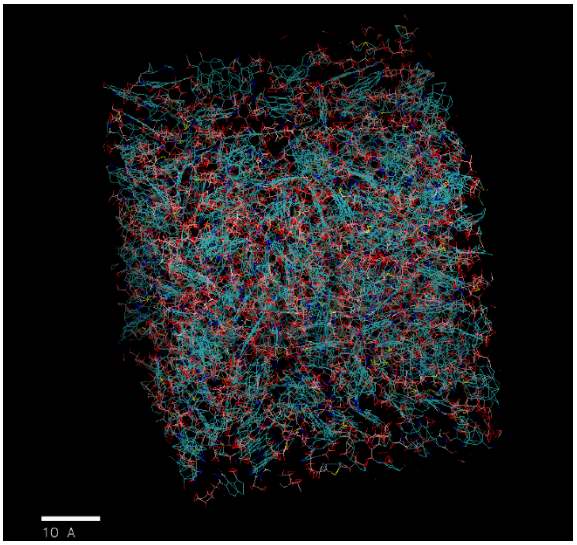


Figure 3.13: Relaxed structure of kerogen (blue color) and octane (red color) mixture after simulated annealing

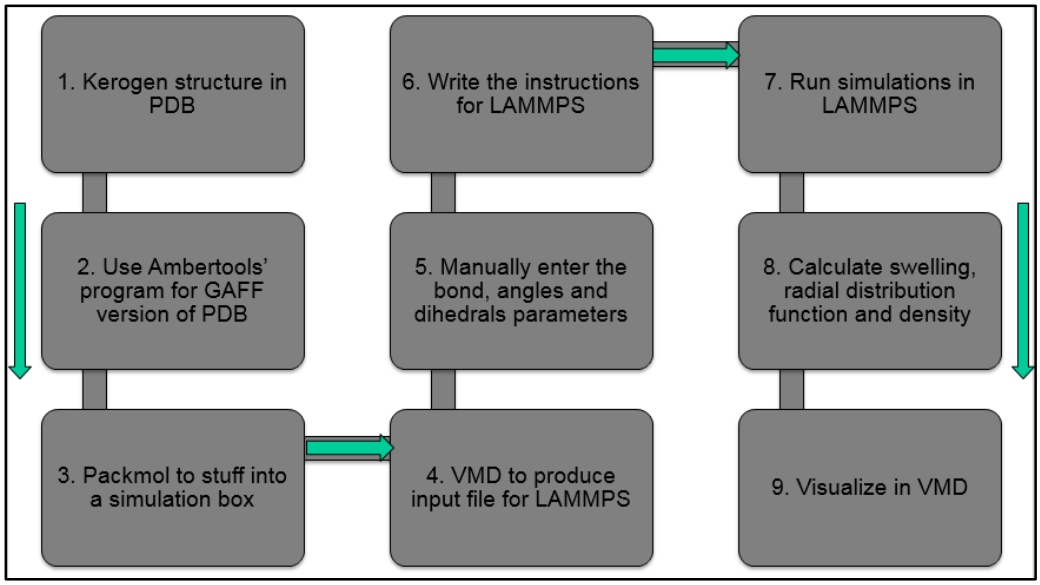


Figure 3.14: Workflow for modeling kerogen using GAFF

# CHAPTER 4

# MOLECULAR MODELING STUDY OF BUBBLE POINTS OF HYDROCARBON MIXTURES IN NANOPOROUS MEDIA

## 4.1 Abstract

Shale resources have played a key role in increasing oil production in the last decade in the United States. The sizes of pores in shales storing oil are believed to be of the order of nanometers. It is believed that the fluids present in such small nanometer scale pores have different properties compared to properties measured in the bulk. Fluid saturation pressures at given temperatures – bubble points for oils and dew points for condensates in the nanopores, are affected by pore walls in the vicinity of the fluid molecules. Approach to the bubble point or dew point influences the proportion of liquid or gas produced from a given well, and thus impacts the economic viability. Hence, an accurate measure of saturation pressures is important. In this paper, we describe experiments in well characterized synthesized mesoporous materials and present Gibbs Ensemble Monte Carlo (GEMC) simulations for understanding the possible reasons for observations made in the experiments.

The experimentally measured saturation pressures of a mixture of decane-methane in confined spaces of the mesoporous material are observed to be less than the oil saturation

---

pressure of mixture in the bulk state. The GEMC simulations were performed to investigate fluid phase equilibrium in confined pores and find possible reason(s) behind the suppression of bubble points in the confined spaces. The simulations show that reduction in critical properties of the nano-confined fluids leads to the suppression of bubble point pressures of the fluids mixtures in confined pores.

## 4.2 Introduction

The oil and gas production from shale plays have significantly increased the overall oil and gas production in the United States[69]. Of the total U.S. crude oil production in the year 2015, roughly 52% or about 4.5 million barrels per day of crude oil were produced directly from shale and other tight rock resources according to U.S. Energy Information Administration (EIA). Figures 4.1 and 4.2 show the recent total production from shale gas and tight oil (majorly shale oil) plays, respectively, in the U.S.

Even with successful shale exploitation in the U.S. in the last decade, there is still a constant challenge of increasing the recovery from the shale reservoirs. Much of the decades of understanding from conventional oil and gas exploration fails to increase primary recovery over 10% in shale oil[1,70] and 20% in shale gas plays. The shale rocks are also the source of oil and gas and contain organic matter, known as kerogen[71,72], in them. Kerogen is a complex organic matter which is a precursor to oil and gas found in shales. The nanometer scale pores (1-20 nm) in organic (kerogen) and non-organic parts of shales have been discussed earlier[73] and are referred to as ‘nanopores’ in the rest of this chapter. Such small pore dimensions add additional complexity to the behavior of fluids present in shales. Currently, there is still a huge gap in the understanding of storage and transport of hydrocarbons in shales. When the dimensions of pores are comparable to

the mean free path of the fluid molecules, collisions with the wall of the pores cannot be neglected. At the nanoscale, in the confined pores of shales, phase behavior of fluids not only depends on fluid-fluid interactions, as in the bulk state, but also depends on fluid - pore wall interactions[60,58]. The pore surface area per unit volume increases as pore dimensions decrease; therefore, the surface forces are not negligible at the nanoscale[74]. This interaction between fluid molecules and pore walls needs to be included in any calculation of thermodynamic fluid or transport properties in shales. Traditional equations of state fail to incorporate the complexity of pore wall interactions in calculating thermodynamics properties of confined fluids. The current work aims to study the effect of pore wall – fluid interaction on pressure-volume-temperature (PVT) properties of the fluids residing in nanopores of shales.

In recent years, there has been major interest among researchers in looking at fluid thermodynamic properties in confined pores[57–63,75–80]. The current work employs molecular modeling techniques to look at the equilibrium between co-existing vapor-liquid phases in the nanopores and comparing that to experiments conducted on artificially created meso- (~3.5 nm pore diameter) porous material. Sheng[59] has demonstrated through experimental work that there are two phases of fluids inside the nanometer scale pores: the free confined phase and the adsorbed phase. Such small pores are abundant in shales. However, to the author's knowledge, a fundamental understanding of the differences in thermodynamic properties between free confined fluid and bulk fluid has not been well characterized. In order to understand the phase behavior of confined fluids, this work studies the vapor-liquid equilibrium of confined fluid while ignoring other possible effects such as adsorption. The free but confined phase has

properties that are different from the bulk fluid because of interactions with pore walls. The free-confined fluid phase is different from the adsorbed phase; however, the two phases may remain in a thermodynamic equilibrium. The adsorbed fluids stay in the form of single to multiple layers of fluid molecules adsorbed on the walls inside of the pore. The vapor portion of the adsorbed fluid may condense depending on a threshold temperature and pressure. This condensed liquid phase is a manifestation of the confined capillary condensation phenomenon[63]. Such condensation usually happens at a temperature and pressure below the phase boundary of the bulk fluid. However, for the current research, the effect of adsorption and possible capillary condensation are ignored in order to focus on the effect of confinement on the behavior of free fluid phase in the nanopores[59]. Further, the effect of high capillary pressure in the smaller pores is also ignored in the current work. Each shale nanopore has its own vapor-liquid equilibrium established within the pore. Therefore, a series of Gibbs Ensemble Monte Carlo (GEMC)[81,82] simulations are performed to understand fluid phase equilibrium within a nanometer scale pore. The key PVT properties affected by the confinement of fluids include phase boundaries, phase compositions, and saturation pressures (bubble points and dew points), interfacial tensions, fluid viscosities, and fluid densities. For this work, the effect on densities, phase boundaries, and the bubble points are studied using a combination of experiments and molecular modeling. The experiments were conducted to measure the bubble points of the liquid hydrocarbon mixture (decane-methane in a 90-10% molar ratio) confined in nanometer sized pores. For the experimental part, synthesized mesoporous materials with perfectly calibrated nanometer sized pores were used to represent the porous system in shale reservoirs. Nitrogen adsorption/desorption

isotherms and transmission electron microscopy (TEM) were used to characterize the samples. Measurements show that the synthesized materials have a highly ordered hexagonal mesostructure and a narrow pore size distribution. Bubble point pressure measurements for decane-methane mixtures were performed in these mesoporous materials. The experimental results are complemented with the results from molecular simulations (GEMC) to understand the dynamics at a pore scale and to investigate reasons behind the suppression in bubble point pressure that was observed in the experiments.

## 4.3 Simulation Methodology

Gibbs Ensemble Monte Carlo (GEMC)[81,82] simulations are molecular-scale simulations that have been widely used by researchers to study vapor-liquid equilibrium in various scenarios, including in confined spaces[19–23]. There has not been wide application of GEMC simulations to study the effect of confinement in ultra-tight oil and gas formations such as shales. The GEMC simulations technique is used in the current work to understand the effect of confinement of fluid molecules in graphite slit pores, evaluating changes in the fluid density and phase behavior of the fluid mixture. GEMC simulations were performed for pure decane and a 90-10 % molar ratio binary mixture of decane-methane confined in 3.5 nm wide graphite slit pores. The 3.5 nm was specifically selected because the average pore size in the synthetic SBA-15 porous media on which experiments were performed was 3.5 nm.

The GEMC simulations establish phase co-existence between two regions in accordance with the following four thermodynamic criteria [81,82]:

1. The two regions should be in internal equilibrium,

2. The temperature in the two regions should be the same,
3. The pressure in the two regions should be the same, and,
4. Chemical potential of all components in the two regions should be the same.

Once the simulations are configured to be performed at a constant temperature, the following three Monte Carlo moves are performed in the Gibbs Ensemble in order to achieve thermodynamic equilibrium between the two co-existing phases:

1. Displacements of particles within each region to ensure equality of internal energy,
2. Fluctuations in the volume of the two regions to ensure equality of pressure, and,
3. Transfer of particles between the two regions to ensure equality of chemical potential

Figure 4.3 shows a schematic of the Gibbs Ensemble method and explains the three kinds of Monte Carlo moves indicated above.

In the current work, GEMC simulations were performed on pure decane (Figure 4.4) and a 90-10% molar ratio decane-methane binary mixture. The set-up of the GEMC simulations performed between the regions of the liquid and vapor phases of decane is shown in Figure 4.4. To include the effect of confinement, the GEMC simulations were performed on the fluid(s) confined in a slit pore geometry with graphite walls (Figure 4.4 and 4.5).

The molecular simulation methodology involved performing canonical (NVT) GEMC simulations at constant temperature. In canonical (NVT) ensemble, the number of molecules (n), volume of the system (v), and temperature of the system (t) are kept constant throughout the simulations. As the simulations are performed at different temperatures, phase equilibrium established between the liquid and vapor phases shifts.

This temperature-dependent equilibrium shift between the two phases is evidenced by the different mole fractions of each component in the two phases and by the different density of each phase as the temperature is changed. Using a series of simulations, vapor-liquid equilibrium was simulated at different temperatures. At every isothermal phase equilibrium simulation, densities and mole fraction of each component in the two phases are monitored.

The 12-6 Lennard-Jones[85] (L-J) potential was used to account for non-bonded interactions between the fluid molecules. The TraPPE-UA force field parameters were used in the L-J potential which is described as:

$$\emptyset(r) = 4\epsilon_{ij}\left[\left(\frac{\sigma_{ij}}{r_{ij}}\right)^{12} - \left(\frac{\sigma_{ij}}{r_{ij}}\right)^{6}\right] \tag{4.1}$$

where $\epsilon$ is the depth of the potential well, σ is the finite distance at which the inter-particle potential is zero, and r is the distance between the particles. The subscripts ij indicate the molecule i and molecule j. The Lorentz-Berthelot[86,87] combining rules are used for calculating the parameters for unlike molecules:

$$\sigma_{ij} = \left(\sigma_{ii} + \sigma_{jj}\right)^2 \tag{4.2}$$

$$\epsilon_{ij} = \sqrt{\epsilon_{ii}\epsilon_{jj}} \tag{4.3}$$

The pore wall-fluid interaction potential ($\phi_{fw}$) was calculated from the Steele Potential[88,89] (10-4 Lennard-Jones wall):

$$\phi_{fw}(z) = 2\pi\rho_w\epsilon_{fw}{\sigma_{fw}}^2\Delta\left[\frac{2}{5}\left(\frac{\sigma_{fw}}{z}\right)^{10} - \left(\frac{\sigma_{fw}}{z}\right)^{4} - \left(\frac{{\sigma_{fw}}^4}{3\Delta(z+0.61\Delta)^3}\right)\right] \tag{4.4}$$

where $\epsilon, \sigma, \Delta$ are the well depth of the potential, molecular diameter, and distance between layers of fluids (f) and graphite (w), respectively. For a given pore width (H), as shown in Figure 4.3, the total potential energy inside the pore is given as[83]:

$$\phi_{pore}(z) = \phi_{fw}(z) + \phi_{fw}(H - z) \tag{4.5}$$

where z is the coordinate axis perpendicular to the pore wall. The slit distance (H) is fixed at 3.5 nm (to complement the experiments performed with the manufactured material, SBA-15, that has a pore dimension of 3.5 nm). The values of $\epsilon_{ww}, \sigma_{ww}, \text{and } \Delta$ for graphite were taken to be 28.0 K($k_b$), 0.340 nm, and 0.335 nm, respectively, as inferred from earlier work on the Steele Potential[83,88,89]. The fluid parameters for methane and decane ($\epsilon_{ff}, \sigma_{ff}$) were chosen based on the TraPPE-UA force field developed by Martin and Siepmann[90]. The values of $\epsilon_{fw}$ $and$ $\sigma_{fw}$ were calculated using the combining rules discussed below.

$$\epsilon_{fw} = \sqrt{\epsilon_{ff}\epsilon_{ww}} \tag{4.6}$$

$$\sigma_{fw} = \left(\sigma_{ff} + \sigma_{ww}\right)^2 \tag{4.7}$$

## 4.4 Bubble Point Measurement

In preliminary work conducted by Hyeyoung Cho (based on personal communication with Hyeyoung Cho), two different mesoporous materials, with similar pore sizes, were used to observe the effect of pore morphology on hydrocarbon mixture phase behavior. SBA-15 and SBA-16 have highly ordered hexagonal and cubic mesoporous silica structures. SBA-15 was synthesized in the presence of triblock poly (ethylene oxide)–

poly(propylene oxide)–poly(ethylene oxide) (PEO–PPO–PEO) copolymers and SBA-16 was synthesized using a poly(alkylene oxide) triblock copolymer. The bubble point pressure of the 90:10 mole ratio methane and decane mixture in bulk (no porous medium confinement) was 374 psia at 100$^{o}$F (310K). In SBA-15 the equivalent bubble point was 242 psia at 100$^{o}$F (310K). Thus, the experimentally measured saturation pressure with SBA-15 was lower than the saturation pressure measured for the bulk fluid.

## 4.5 Result and Discussion

### 4.5.1 Simulations for Decane-Methane Mixture

To investigate the preliminary phase behavior data acquired by the experiments described earlier (suppression of 132 psia in bubble point pressure of 90-10 decane-methane mixture at 100$^{o}$F under the effect of confinement in 3.5 nm pores), GEMC simulations were performed for pure decane and a 90-10 % molar ratio binary mixture of decane-methane confined in 3.5 nm wide graphite slit pores. The 3.5 nm width was specially selected because the average pore diameter in the synthetic SBA-15 porous medium used in the experiments was 3.5 nm.

The GEMC simulations were performed for pure decane for a range of temperatures. A series of isothermal simulations were performed at different temperatures. In all of these simulations of decane (vap) – decane (liq) equilibrium, the density of each phase was monitored. The density for each phase was plotted against temperature to develop a temperature-density plot, as shown in Figure 4.9. The simulations were performed for two cases – one considering pore wall-fluid interaction, the other without the effect of pore wall-fluid interaction. The pore wall-fluid interaction was captured using Steele potential, as discussed in Section 4.3. The density plots were extrapolated from the near-

critical region to estimate the critical temperature of pure decane in bulk and confined states[58,90]. The critical temperature of decane was estimated at 705K (compared to the true critical point of 618K). A suppression of 125K in critical temperature was observed for the confined decane. This is close to the observations made by other researchers[80,91]. The difference between the two values (bulk and confined) is more relevant than the actual values.

The Antoine[92] equation was used to calculate the corresponding change in critical pressure of the confined fluid. This equation has applicability for wide range of temperatures[93] including near the critical region for decane. The Antoine equation (refer to Eq. 8) was used to calculate the suppression in the critical pressure of confined decane:

$$\ln(P) = A - \frac{B}{T+C} \tag{4.8}$$

where P and T are in kPa and $^{O}$C; A, B, and C are constants and their values are based primarily on data presented by Poling[94].

The pressure-temperature (PT) plot for pure decane is shown in Figure 4.10. The bulk values for the critical properties estimated from the GEMC model were used in this plot. A suppression in vapor pressure is observed for the confined decane. Such a suppression happened due to change in the critical properties of the pure decane confined in nanometer scale pores. This is a clear indication of changes in the thermodynamic properties of fluids confined in the nanopores. This changes the phase behaviour of free confined fluid compared to the same fluid in a bulk state. A potential reason for change in the fluid's thermodynamic properties and thus, phase behavior of confined fluid is the pore wall-fluid interactions that are dominant at a nanometer scale. These surface forces cannot be neglected at the nanometer scale because the surface area per unit volume is

very high at such a small scale.

GEMC simulations based on the workflow discussed earlier were again performed for the binary mixture of decane – methane (90-10% molar ratio) to complement the findings from the experiments. The motivation for these simulations was to understand the dynamics at a pore scale and to contribute to the fundamental understanding of phase behavior of fluids in confined spaces of shale rocks. The simulations helped in identifying a potential reason for suppression in the bubble point of the binary mixture of decane and methane that was observed from the experiments. This understanding can be utilized in the study of phase equilibria of other hydrocarbon mixtures confined in nanometer scale pores. The GEMC simulations were performed at different temperatures to simulate the phase equilibrium between vapor and a liquid decane-methane mixture. The densities at each isothermal step were monitored and plotted to develop a temperature-density plot for the binary mixture (Figure 4.11). The densities from the near-critical region were extrapolated with good $R^2$ values to estimate the critical temperature of the mixture. A suppression of about 85K in the critical temperature of the binary mixture is observed for the confined mixture compared to the bulk mixture. The critical density is also supressed by 0.55 g/mL in the confined mixture. This change in the fluid thermodynamic properties leads to the corresponding change in phase behaviour of the confined fluids. By performing the molecular modeling using GEMC simulations, it was observed that the fluids behave like a bulk fluid if the Steele pore wall potential was not used in simulating the phase behavior. This indicates that pore wall-fluid interaction is a primary reason for suppression of the critical properties and vapor pressure of the confined fluids.

### 4.5.2 Simulations for a Decane-$CO_2$ Mixture

The phase behavior of a confined decane-carbon dioxide mixture is important in the study of minimum miscibility pressures of carbon dioxide ($CO_2$) in confined spaces. GEMC simulations were performed on 90-10% molar ratio binary mixture of decane and carbon dioxide. To include the effect of confinement, the GEMC simulations were performed on the fluid(s) confined in the slit pore geometry made up of graphite walls. The molecular simulation methodology involved performing canonical (NVT) GEMC simulations at constant temperature. In canonical (NVT) ensemble, the number of molecules (n), volume of the system (v), and temperature of the system (t) are kept constant throughout the simulations. The simulations were performed at different temperatures. Phase equilibrium established between the liquid and vapor phases shifts. This temperature-dependent equilibrium shift between two phases is evidenced by the different mole fractions of each component in the two phases and the different density of each phase as the temperature is changed. Using a series of simulations, vapor-liquid equilibria were simulated at different temperatures in this work. Densities and mole fraction of each component in the two phases were monitored for every isothermal phase equilibrium simulation.

The GEMC simulations were performed for decane-$CO_2$ for a range of temperatures. As before, again in this part, each isothermal simulation of decane-$CO_2$ (vap.) – decane-$CO_2$ (liq.) equilibrium, the density of each phase was monitored. The density for each phase is plotted against temperature in Figure 4.12. The simulations were performed for two cases – one considering pore wall-fluid interaction to represent a confined state, the other without the effect of pore wall-fluid interaction to represent the bulk state. The pore

wall-fluid interaction was captured using the Steele potential discussed above. The density plots were extrapolated from the near-critical region to estimate the critical temperature and critical density of decane-$CO_2$ in bulk (no pore-wall – fluid interaction) and a confined state (with pore-wall-fluid interaction)[58,90]. The critical temperature of the bulk decane-$CO_2$ binary mixture determined from GEMC was found to be 660K (compared to the true critical point of 615K predicted by a commercial PVT simulator). The critical temperature in a confined mixture in the presence of pore-wall-fluid interaction was found to be 675 K, as shown in Figure 4.12. GEMC indicated that the critical density of the confined mixture was suppressed by 0.15 g/mL from the bulk critical density of 0.38 g/mL. The difference between the two values (bulk and confined) may be more relevant than the actual values.

## 4.6 Conclusions

The bubble point pressures in the bulk were found to be higher than the bubble points of the same fluids confined in nanometer scale pores in synthetic mesoporous material. GEMC simulations were performed to diagnose this bubble point suppression for confined fluids. The GEMC simulations indicated that the pore wall-fluid interactions are dominant at the nanometer scale and suppress the critical properties of fluids confined in nanometer scale pores. A suppression in the critical point of a confined decane-$CO_2$ mixture is also observed. This has implications in the calculation of minimum miscibility pressure of $CO_2$. The estimation of correct fluid thermodynamic properties, including pressure-volume-temperature (PVT) properties, is essential to for better prediction of reserves and the rates of recovery of these reserves from shale plays. Conventional PVT simulators do not account for pore wall-fluid interaction and fail to capture the

suppression of the critical properties of these confined fluids. Conventional PVT simulators should be updated with models like the one proposed here in order to capture the dynamics at a pore scale.

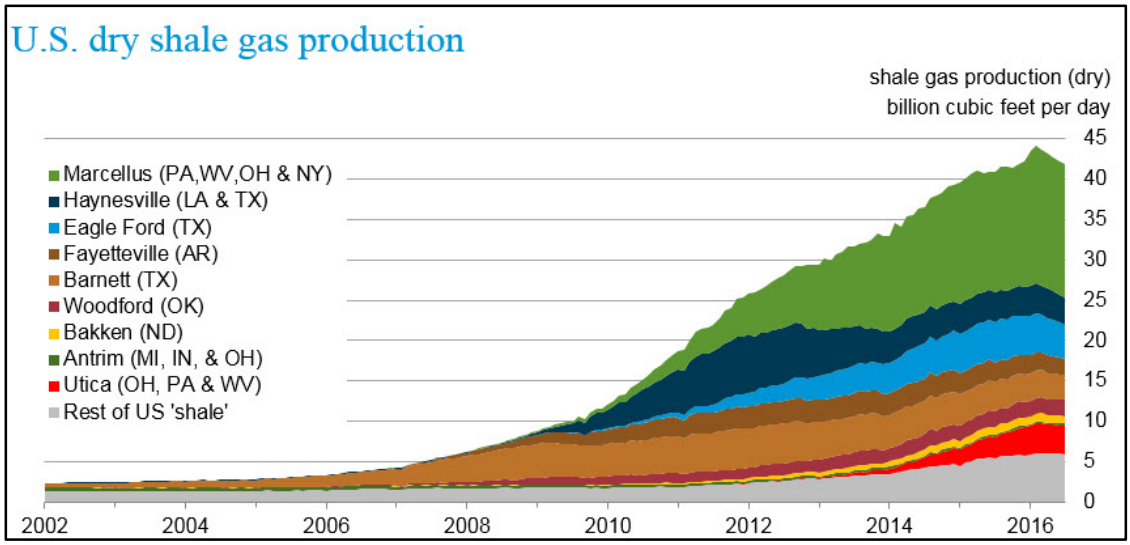


Figure 4.1: U.S. Energy Information Administration (EIA) official shale gas production data through July 2016. The figure shows current gas production of over 40 BCF of gas per day from US Shale gas plays. The gas production has increased in the past decade due to increased exploration and drilling activities in shale gas plays; however, the recovery from individual shale gas wells is still no more than 20% on average. Source: US Energy Information Administration (EIA) web-article [95].

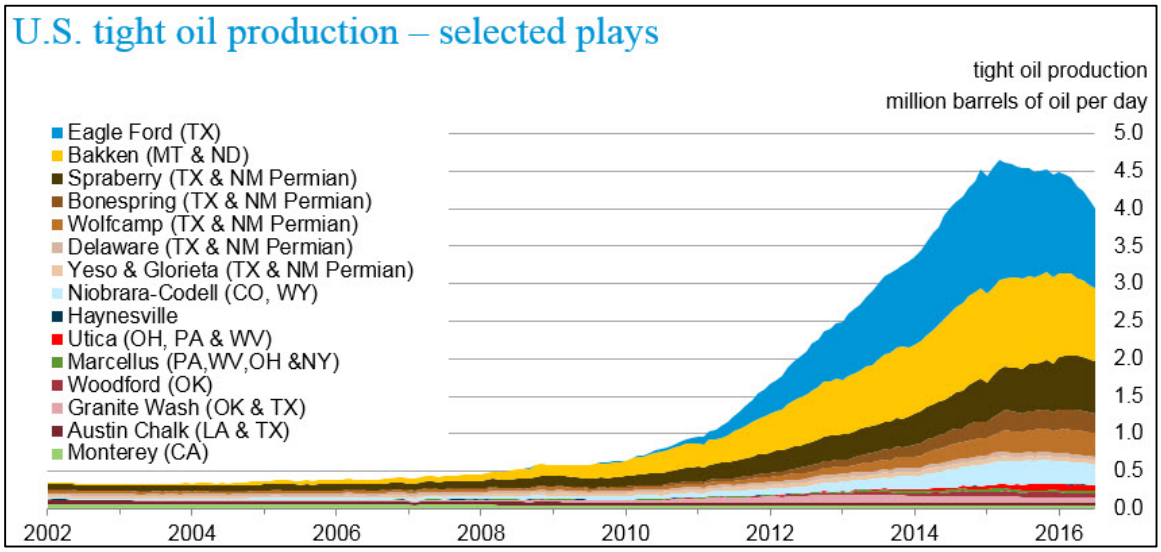


Figure 4.2: U.S. Energy Information Administration (EIA) official tight oil production data through July 2016. The figure shows current oil production of over 4.0 million barrels of oil per day from US tight oil plays. Tight oil in US is produced majorly from low-permeability shale formations but also includes sandstones and carbonates. Source: US Energy Information Administration (EIA) web-article [95].

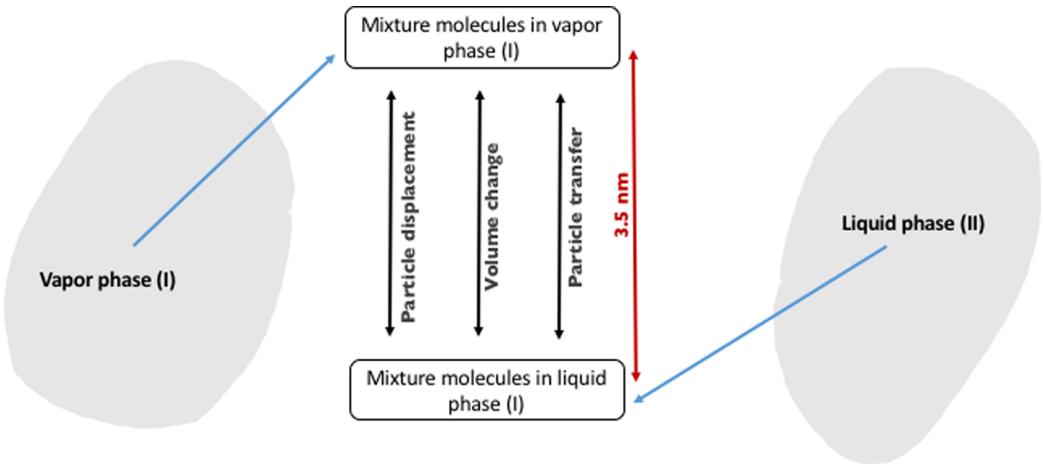


Figure 4.3: Gibbs Ensemble Monte Carlo simulations establish the equilibrium between two fluid phases by employing three kinds of move in the two regions - Region I, II. The two regions are taken from the two simulation boxes, each containing two different fluid phases. The three moves performed in the two regions are particle displacement, volume change, and particle transfer. The figure is redrawn from the work by Panagiotopoulos[82].

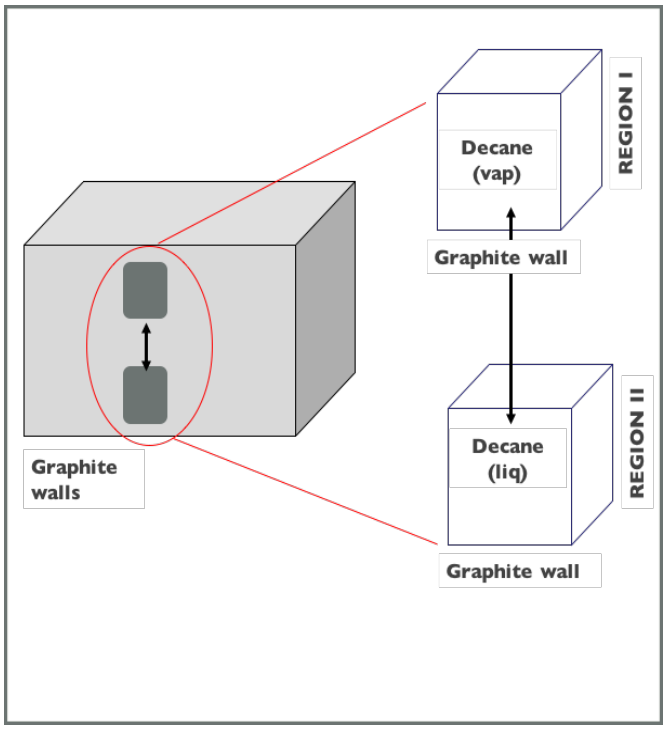


Figure 4.4: The Gibbs Ensemble Monte Carlo (GEMC) simulations were performed on pure decane and a binary mixture of decane and methane (90-10% molar ratio) confined by graphite walls. This figure shows a schematic of the GEMC simulation set-up performed for pure decane. The three kinds of moves in the GEMC simulations were performed in the two regions (Region I and Region II) bounded by graphite walls.

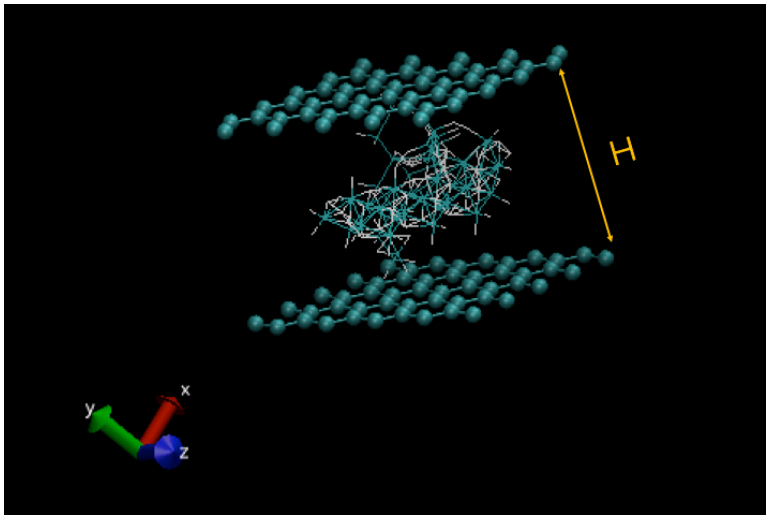


Figure 4.5: The molecular model showing a fluid mixture confined in a graphite slit pore. H is the normal distance between the graphite layers forming the pore, also known as pore width. H will correspond to the pore dimensions OF SBA-15 used in the experiments discussed in this chapter. H is also represented in the wall-fluid potential discussed later in the text.

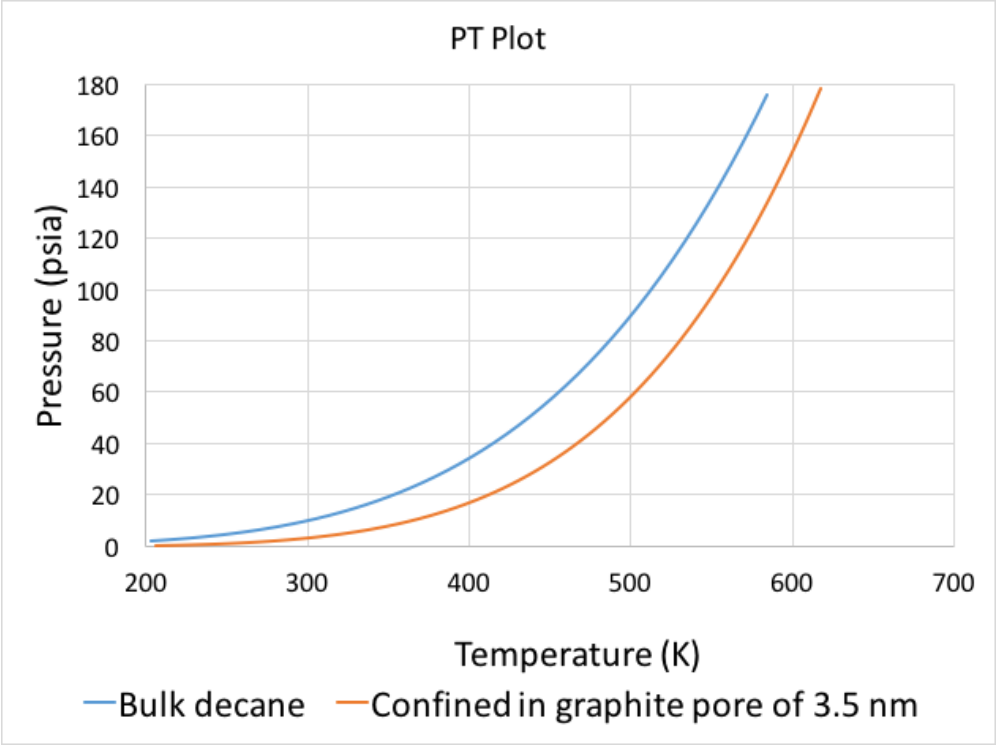


Figure 4.6: The PT plot for pure decane. Vapor pressure suppression is observed for decane confined in the slit pore made up of graphite.

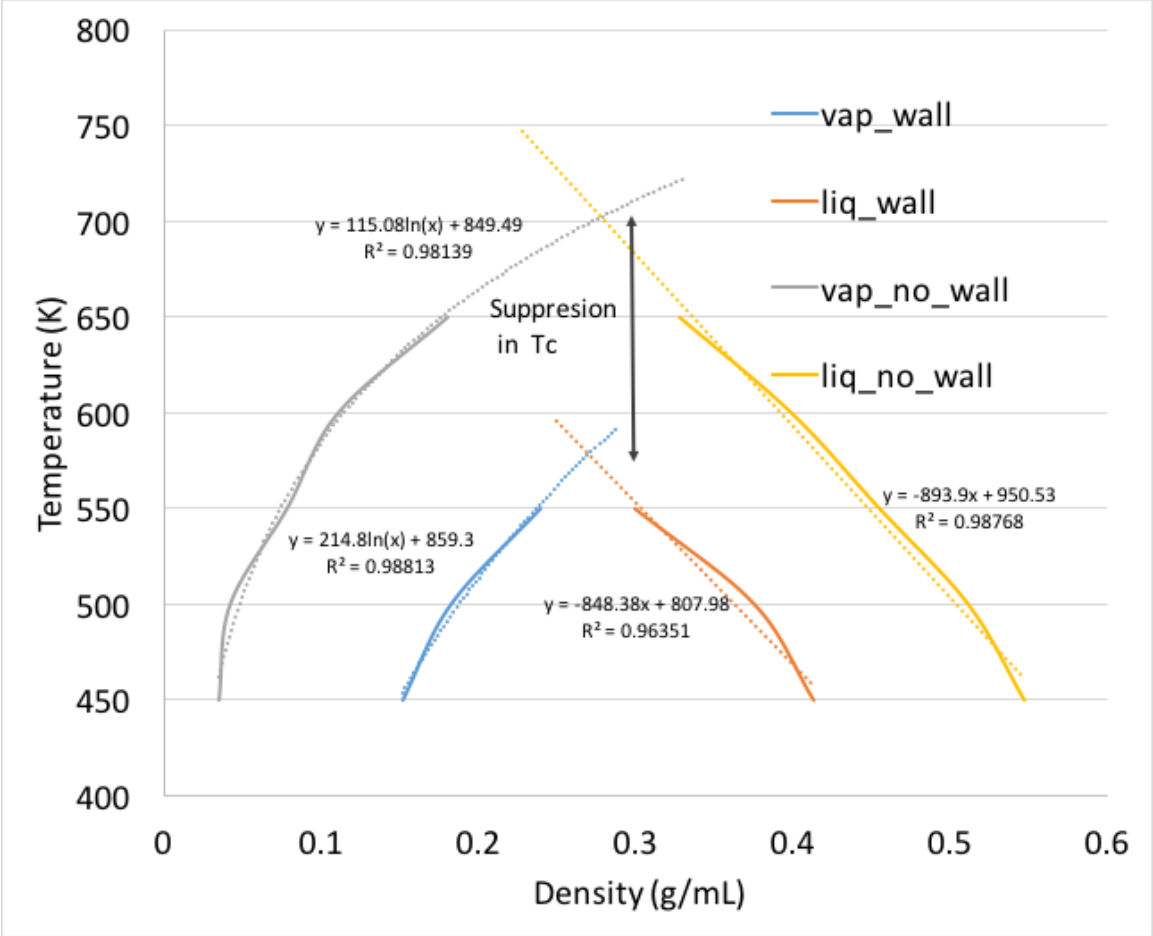


Figure 4.7: Temperature-density plot for pure decane. The densities from the near-critical region were extrapolated with good $R^2$ values to estimate the critical temperature of the decane in confined and bulk states. Suppression of approximately 125K or 225$^{o}$F is observed for the critical temperature of decane confined in nanometer scale pores. This is similar to the observations made by other researchers[80,91]. vap_wall and liq_wall in the legend refer to the use of Steele pore wall potential to account for pore wall-fluid interaction. vap_no_wall and liq_no_wall represent the bulk state when pore wall-fluid interactions were not included.

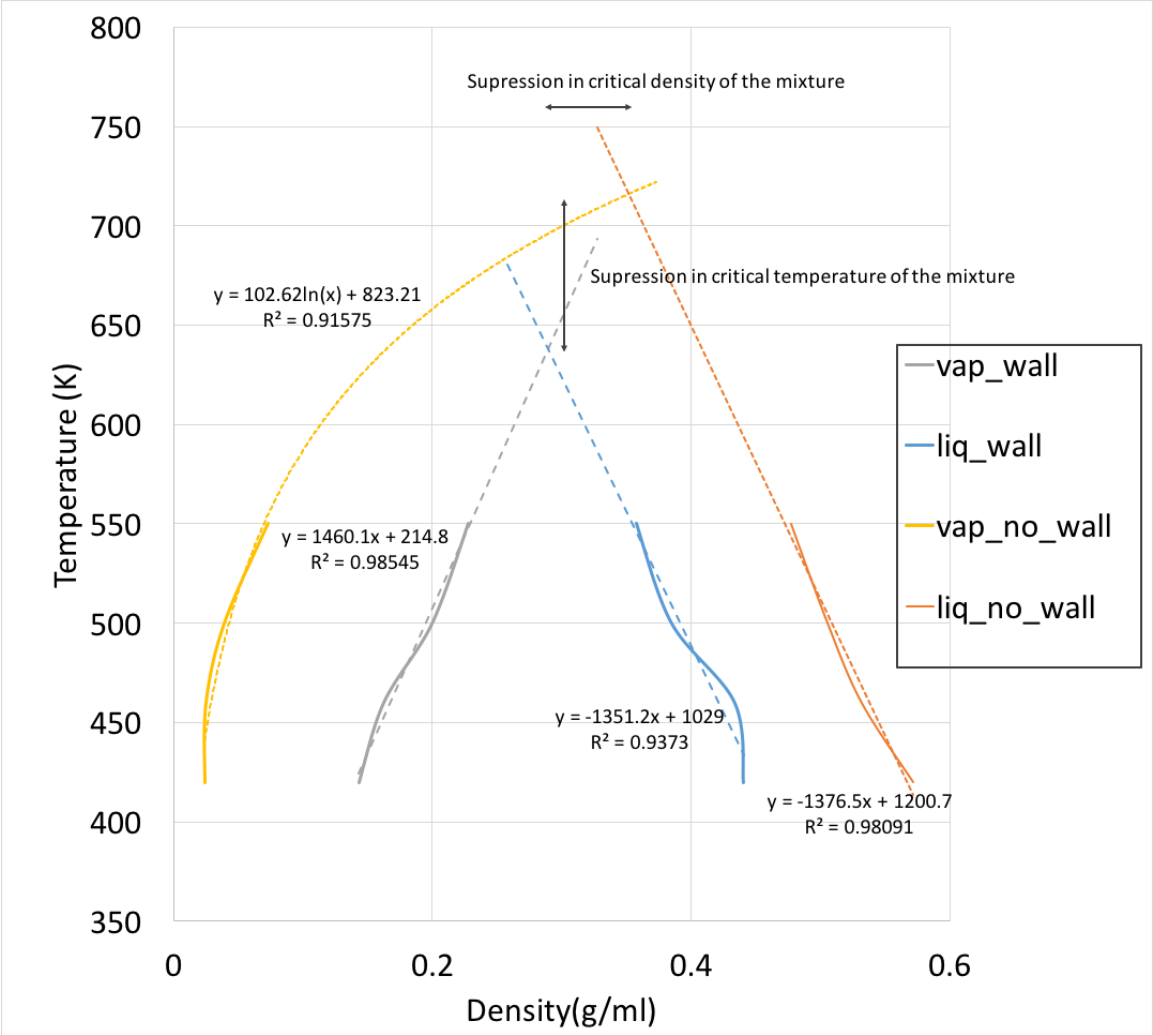


Figure 4.8: Temperature-density plot for a mixture of decane-methane (90-10% molar ratio). A critical temperature suppression of about 85K is observed for 90-10% molar ratio binary mixture of decane and methane. liq_wall and vap_wall in the legend refer to the use of Steele's pore wall potential to account for pore wall-fluid interaction. liq_no_wall and vap_no_wall represent the bulk state when pore wall-fluid interactions were not included. Suppression in the critical properties of the confined fluids is attributed to the pore wall-fluid interaction that becomes dominant at the nanometer scale.

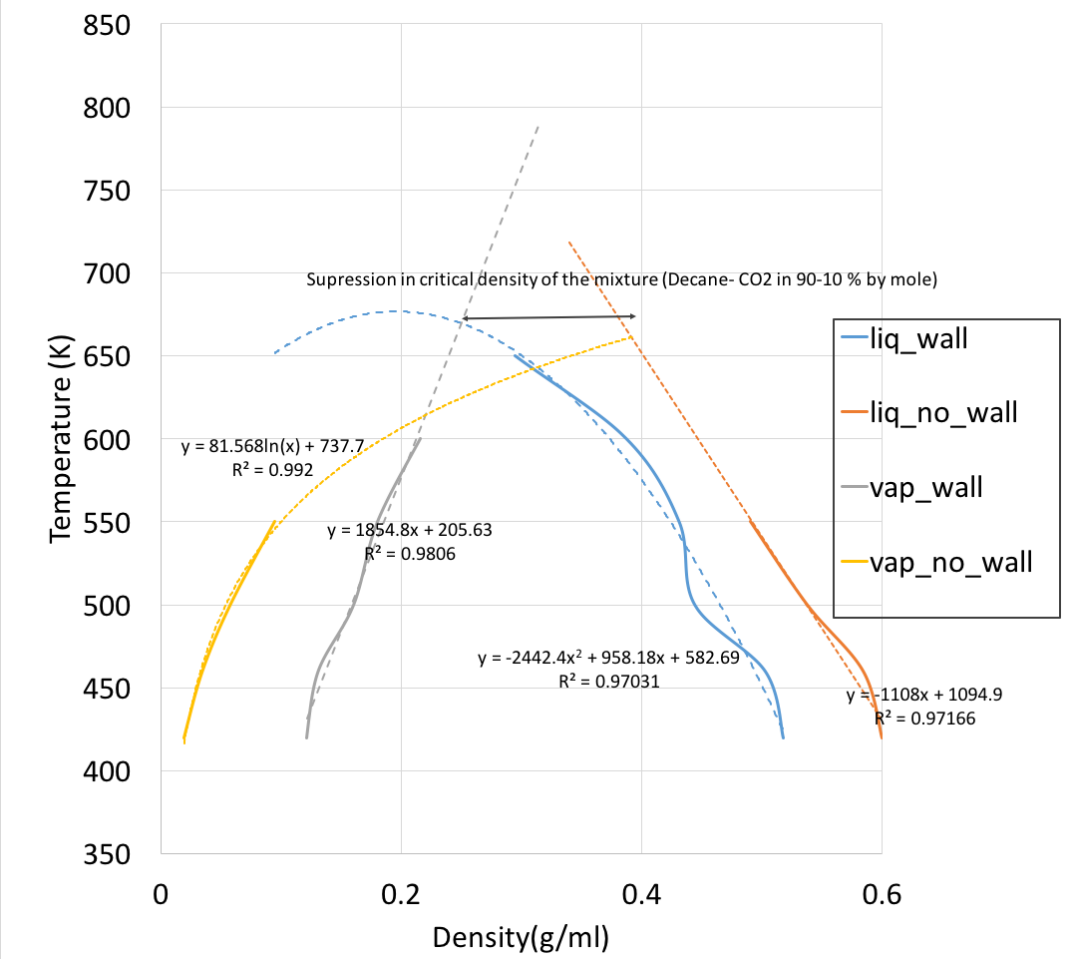


Figure 4.9: Temperature-density plot for a decane-$CO_2$ mixture of (90-10% molar ratio). The critical density is supressed by 0.15 g/mL in the confined binary mixture relative to the bulk critical density of 0.38 g/mL. liq_wall and vap_wall in the legend refer to the use of Steele's pore wall potential to account for pore wall–fluid interaction. liq_no_wall and vap_no_wall represent the bulk state when pore wall-fluid interactions were not included. Suppression of the critical density for the confined decane-$CO_2$ binary mixture is attributed to the pore wall–fluid interactions that become dominant at the nanometer scale.

# CHAPTER 5

# MOLECULAR INVESTIGATION OF ENHANCED GAS RECOVERY BY CARBON DIOXIDE SEQUESTRATION IN GAS-RICH SHALES

## 5.1 Introduction

The overall recovery factor from shale gas plays is only about 20%[37]. Gas bearing shales are sites for continuous gas accumulation rather than trapped gas in the conventional reservoirs, and different approaches (other than hydraulic fracturing) may be appropriate for increasing recovery. As demonstrated in previous chapters, residual kerogen present in these rocks changes the dynamics of gas storage and production. According to simple scaling laws, the surface area per unit volume is inversely proportional to the scale of the porosity in geometrically similar porous materials. Due to the nanoscale porosity of gas-rich kerogen, the surface area per unit volume is very high. Consequently, adsorption on kerogen surfaces may play an important role in gas retention. The net attractive interactions between gas molecules and kerogen surfaces may lead to adsorption of significant volumes of gas in kerogen. The nanometer scale pores in kerogen[73] add another level of complexity to gas storage and production and increases the challenges of estimating the retention of natural gas in organic-rich shales. The connected nanopores may form nanochannels, which could provide important fluid

flow pathways in the kerogen and contribute to fluid transport on longer scales within organic-rich shales. However, permeability scales as the square of the hydrodynamic pore diameter, and the permeability of a connected network of nanoscale pores would be very small. For much the same reason, the matrix permeability of shales formed from very small sediment particles is also very small. However, the fracture permeability in those clastic sediments may be much higher. The low permeability and the sorptive retention of gas are key reasons for low recovery from shale gas plays. Assuming that the gas molecules can diffuse out of the kerogen matrix through the walls of kerogen[96], there could be a significant amount of sorbed gas in the kerogen matrix that may be produced by replacing it with gas of higher sorption affinity for kerogen such as carbon dioxide. Sorption of carbon dioxide may drive desorption of methane that was originally adsorbed by the kerogen component of gas-rich shales at in-situ conditions[97]. Here we report a fundamental, molecular, pore scale investigation of carbon dioxide enhanced production technologies for shale gas plays.

## 5.2 Background of Carbon Dioxide Enhanced Production

In recent years, there have been many investigations of using carbon dioxide to enhance production from shale gas plays. One approach is to use carbon dioxide as an injection fluid, perhaps in a cyclic process (huff-n-puff technique). For huff-n-puff scenarios, some reservoir scale simulations indicate that increased recovery can be achieved[98,99,100,101,102]. Another approach is to use carbon dioxide as a hydraulic fracturing/refracturing fluid [103]. The carbon dioxide is pumped as a viscosified, foamed, or energized fluid to fracture the formation. Neat $CO_2$ is rarely used for primary stimulation because of its poor proppant carrying ability. Several field investigation[104,105]

have demonstrated increased production after fracturing/refracturing using carbon dioxide. Simulations also indicate that gas recovery can be increased in this manner [106].

In both of these approaches for using carbon dioxide for increasing gas recovery, at least some of the carbon dioxide will penetrate into the targeted formation and interact with its various organic and inorganic components. The purpose of the molecular dynamics (MD) simulations presented in this article was to obtain a better understanding of the effects of carbon dioxide on kerogen and natural gas (represented by methane) within shales under in-situ conditions. When carbon dioxide reaches the targeted formation at depth, it is already in the supercritical form (at pressure of 300 atmospheres and temperature of 400K). Supercritical carbon dioxide will be referred to as just carbon dioxide in the rest of this manuscript. In the subsurface, carbon dioxide will interact with various components of the rock. A shale can be broadly divided into the solid inorganic matrix, solid organic matter, and fluids. The inorganic matrix consists mostly of various minerals including clays, quartz, carbonates, clays (aluminosilicates), etc. Some of these minerals may interact chemically with carbon dioxide and adsorb it, particularly some of the clays. Adsorptive capacity can be reduced in the presence of water. However, the current work focuses on the interaction of carbon dioxide with the solid organic components that are mostly residual kerogen. Kerogen consists of organic matter that is usually embedded in the inorganic matrix of shales. The kerogen is classified into four main types as shown in the Figure 5.1 based on its atomic composition and origin. As kerogen-bearing sedimentary rock is progressively buried over geologic time, the kerogen undergoes chemical and physical alteration because of the increasing temperature and stress (a process known as catagenesis or maturation). As the maturity

of the kerogen increases, first oil, then wet gas, and finally dry gas (mainly methane with only small amounts of higher molecular mass hydrocarbons) are produced from the remaining kerogen. The kerogen can be classified in terms of both type and maturity (in the oil window or wet gas window or dry gas window).

The work reported here focused on a particular type of kerogen (type II) at a particular maturity (near the end of the oil window and the beginning of the wet-dry gas window). The kerogen model for this type II kerogen was taken from the work of Ungerer et al. (2015) and is shown by the red dot on the Van Krevelen diagram in Figure 5.1. The chemical formula of this kerogen model is $C_{242}H_{219}O_{13}N_5S_2$. The H/C and O/C ratios of this model unit are 0.905 and 0.054, respectively. Type II kerogen (kerogen with initially high H/C and H/O ratios, formed primarily from marine microorganisms) is known to be oil and/or gas prone in nature. This kerogen type is found in many productive gas-rich shale plays in the US and it is, therefore, a suitable medium for assessing the interaction of typical shale gas kerogen with carbon dioxide and methane.

The sorption of carbon dioxide and methane by organic-rich shale, individually as well as competitively, has been extensively studied experimentally and reported in the scientific literature[107,108]. However, the fundamental molecular level processes that control the kinetics and thermodynamics of methane and carbon dioxide sorption and desorption have not been investigated using realistic kerogen molecular models. All of the experimental studies reported so far have focused only on the sorption of gas by carbon (which accurately represents kerogen only at the end of the dry gas window) or on whole rock shale samples. A few studies have discussed the associated swelling of the carbon or the whole rock samples due to adsorption of gases[108–110].

The swelling of kerogen in our MD simulations is attributed to the combined effects of adsorption and absorption (referred to collectively as sorption), whereas previous work has focused on adsorption[108]. The change in volume of kerogen during desorption of methane and sorption of carbon dioxide may close or open fluid pathways and thus, plays a key role in determining the effective drainage of fluids in shales.

### 5.3 Kerogen Molecular Modeling

The molecular model for type II kerogen developed by Ungerer et al. (2015) was used with the General Amber Force Field (GAFF) developed by Wang et al. (2004) and implemented in LAMMPS (Large-scale Atomic/Molecular Massively Parallel Simulator [21]) to perform molecular dynamics (MD) simulations of kerogen, methane, and carbon dioxide system. Before performing simulations with complex multicomponent systems, the kerogen model was tested because the GAFF force field was different from that used by Ungerer et al. (2015). The General Amber Force Field (GAFF) force field was used to calculate the parameters for bonded as well as non-bonded interactions. The 12-6, Lennard-Jones (L-J) potential[85]

$$\emptyset(r)_{L-J} = 4\epsilon_{ij}\left[\left(\frac{\sigma_{ij}}{r_{ij}}\right)^{12} - \left(\frac{\sigma_{ij}}{r_{ij}}\right)^{6}\right] \tag{5.1}$$

was used to calculate the non-bonded molecular forces. Here, $\epsilon$ is the depth of the potential well, σ is the finite distance at which the inter-particle potential is zero, and r is the distance between the particles. The Lorentz-Berthelot classical mixing rule[86,87] was used to calculate the parameters for unlike atoms in the L-J potential.

$$\sigma_{ij} = \left(\sigma_{ii} + \sigma_{jj}\right)^2 \tag{5.2}$$

$$\epsilon_{ij} = \sqrt{\epsilon_{ii}\epsilon_{jj}} \tag{5.3}$$

Gasteiger-Marsili [66] charges were assigned to all of the atoms in the kerogen and gas molecules (methane and carbon dioxide) to calculate the Coulombic interactions

$$\emptyset(r)_{coulombic} = \frac{C\, q_1 q_2}{\epsilon r} \tag{5.4}$$

Here, $q_1$ and $q_2$ are the charges on interacting atoms, $\epsilon$ is the dielectric constant of the medium, and C is a constant. The final configurations were visualized using VMD (Visual Molecular Dynamics)[20].

Simulated annealing of the kerogen was performed to construct a molecular model that represents the native state (lowest conformational free energy state) of the kerogen. The Ungerer model for medium–high maturity kerogen, shown in Figure 5.2, has the atomic composition $C_{242}H_{219}O_{13}N_5S_2$ and a molecular mass of ~3465 daltons.

To conduct simulated annealing, 15 of these molecules were placed in a cubic box with periodic boundary conditions. MD simulations were performed in a canonical (NVT) ensemble for a 0.2 ns (in 2 million time steps) at a temperature of 2000K and density of 0.22 g/cc. In a canonical ensemble, the number of molecules, temperature, and volume of the system are kept constant. The system was then "annealed" using isobaric-isothermal (NPT) ensembles starting at 1000 atmospheres (≈ 100 MPa) and 1000K, and both the temperature and pressure were reduced in stages (as shown in Figure 5.3) until a final pressure of 300 atmospheres (≈ 30 MPa) and a final temperature of 300K (room temperature) were reached. To monitor the simulated annealing process, the kerogen density was calculated at each step, as shown in Figure 5.3. The density of the type II

kerogen after annealing was 1.18 g/cc at 300K and 300 atmospheres. This matches well with experimentally measured kerogen densities in the range of 1.18-1.23 g/cc reported by Stankiewicz et al. (1994)[111] and 1.2-1.25 g/cc cited by Okiongbo et al. (2005)[22]. The size of the time steps and the lengths of each annealing stage were carefully chosen to guarantee that the system evolved towards equilibrium during each stage.

Figure 5.4 shows the molecular system before and after simulated annealing to a temperature of 300K and a pressure of 300 atmospheres. The kerogen condenses and reaches a quasi-minimum free energy at a temperature of 300K and a pressure of 300 atmospheres. Figure 5.5 shows the radial pair distribution function (g(r)) at a temperature of 300K and a pressure of 300 atmospheres. The radial distribution function, g(r), gives the probability of finding a particle at a distance (r) from another particle, averaged over all of the particles in the system. The first two peaks in the radial pair distribution function correspond to the C-C aromatic and C-C aliphatic bond lengths (1.35 Å and 1.55 Å, respectively) in the simulations. The radial pair distribution function calculated in this work is in good agreement with the radial pair distribution function (calculated at 300K and 0.98 atmosphere) of Ungerer et al. (2015), who developed the original molecular structure model. To investigate the sorption of methane, carbon dioxide, and competitive sorption of methane and carbon dioxide under subsurface conditions, after the annealing, production runs (for measuring the volumetric swelling of kerogen and retention of methane and carbon dioxide) were performed. These production runs were performed at the reservoir temperature and pressure of 400 K and 300 atmospheres (the temperature and hydrostatic pressure at a depth of ≈3 km).

The annealed kerogen structure was cut into thin, planar sections to visualize the pore

structure (Figure 5.6). This revealed sub-nanometer scale pores in the kerogen matrix. These pores are difficult to visualize using electron microscopy since preparing such thin sections may change the molecular scale morphology of the kerogen. Storage of methane and/or carbon dioxide in these nanoscale pores may play an important role in retention/production of natural gas and carbon dioxide sequestration. Methane molecules trapped[112] in these sub-nanometer pores are considered to be part of the sorbed methane. There is a distribution of pore sizes with no clear distinction between methane sorbed by the kerogen matrix (methane in pores of about the same size as a methane molecule), methane sorbed on pore walls, and methane in pores that are large enough for some of the methane to behave like bulk methane under subsurface temperature and pressure conditions. A substantial fraction of the methane is sorbed strongly enough by the kerogen to prevent recovery under normal conditions. However, the kerogen has a higher affinity for carbon dioxide than for methane[107,108], and carbon dioxide may displace sorbed methane[97] .

### 5.4 Simulation of Kerogen, Methane, and Carbon Dioxide System

The Molecular Dynamic (MD) simulations were performed for the ternary kerogen, methane, and carbon dioxide system. The objective of the simulations was to calculate volumetric swelling of the kerogen in presence of gasses and diffusion coefficients of gases in the kerogen matrix: The following four scenarios were considered in the simulations to meet that objective.

a. Pure kerogen,
b. Kerogen with methane (35% of the total kerogen mass),
c. Kerogen with carbon dioxide (the same number of molecules of carbon dioxide as

molecules of methane in scenario b),

d. Kerogen with carbon dioxide and methane in a 3:1 molecular ratio (the same total number of molecules of carbon dioxide and methane as the number of molecules of methane in scenario b). At 400K and 300 atmospheres, this scenario nominally replicates in-situ conditions at a depth of approximately 3 km. The 3:1 ratio between carbon dioxide and methane was based on selective sorption capacities observed experimentally[107,108].

The MD simulations for all four scenarios were performed under a reasonable reservoir temperature (400K) and pressure conditions (300 atmospheres) at a depth of approximately 3km. The amount of methane gas relative to kerogen (35% wt.) used in the simulations was based on the adsorption isotherms for pure carbon and for shales, as documented by other researchers[107,108]. The initial configurations of the multicomponent systems in scenarios b, c, and d are similar. The initial configuration for scenario d is shown in Figure 5.7 as an example. Initially, the gas (carbon oxide and/or methane) was placed outside of the kerogen, and the gas molecules diffused into the kerogen and were sorbed by it during the subsequent MD simulations. The shale samples studied by Heller and Zoback (2014)[108] included shales from the Eagle Ford and Marcellus formations. The kerogen in both the Eagle Ford and Marcellus Shales is medium to high maturity type II[29,113], similar to the kerogen that is used in this study. The sorption of gases by kerogen during the MD simulations indicates that the interaction between kerogen and gases is not just a surface phenomenon (adsorption on kerogen surface or on pore walls made up of kerogen) but also involves internal matrix-gas interaction (absorption). The final configuration of the system after sorption of one or both of the gases is shown in Figure

5.8. The properties of interest – volumetric swelling and diffusion coefficients were calculated during the final production run using an NPT ensemble at in-situ conditions (400 K and 300 atmospheres).

In scenario a, the pure kerogen was simulated under in-situ subsurface conditions. This is followed by scenario b in which the kerogen is exposed to a fixed amount (750 molecules) of methane gas. Part of this gas was sorbed by the kerogen, and the kerogen swells as a result of the sorption. Previously, swelling of kerogen was attributed only to adsorption of gases[108] instead of a combination of adsorption and absorption, i.e. sorption. The volumetric swelling in each of the scenarios b, c, and d was determined by monitoring the change in volume of kerogen during the production runs (after the simulated annealing runs) with methane and/or carbon dioxide. The diffusion coefficients of the sorbed gases (carbon dioxide and methane) in the kerogen were calculated to investigate their preferential retention in the kerogen. The mean square displacement of the gas molecules inside the matrix of kerogen was recorded and diffusion coefficients were calculated from the slope of mean square displacement versus time plots (an example for the case of methane in scenario (b) is shown in Figure 5.9). The mean square displacement was calculated for the final 100,000 steps of the production run. A short time interval was used to ensure that the methane molecules that were tracked remained in the kerogen. The relationship between the mean square displacement and time is represented reasonably well by:

$$\langle r^2 \rangle = 6Dt \tag{5.5}$$

where $\langle r^2 \rangle$ is the mean square displacement, t is time, and D is the diffusion coefficient.

## 5.5 Results and Discussion

Table 5.1 shows the volume of the kerogen with and without sorbed gases (carbon dioxide and methane) at a pressure of 300 atmospheres and temperature of 400 K. The swelling ratio ($Q_v$) is defined as the ratio of the final volume of the swollen kerogen to the initial volume of the annealed kerogen. The swelling ratio of kerogen that has sorbed the same number of molecules (and therefore moles) of carbon dioxide and methane is larger for methane, even though both gases have approximately the same molecular sizes. The swelling ratio ($Q_v$) of kerogen with decane was also calculated to compare it with kerogen swelling ratios obtained from experiments conducted by other authors. The $Q_v$ for type II kerogen in the presence of decane at room temperature and pressure from MD simulations was calculated to be around 1.20. This decane swelling ratio matches closely with the swelling ratio for Draupne type II kerogen (from North Sea Draupne Formation) determined experimentally by Ertas D. et al. (2006). Draupne type II kerogen has a maturity similar to the that of the kerogen model used in this study[114].

The primary reason for the larger kerogen swelling ratio for methane as opposed to carbon dioxide can be attributed to the polar nature and linear shape of the carbon dioxide molecule. These features allow it to associate more strongly with kerogen and better fit into pre-existing pores and free volume. The increase in volume for a given amount of sorbed gas is higher if the mixing molecules (kerogen and methane in scenario b) have a low affinity for each other (increase in volume in scenario b is higher than that in scenario c). Therefore, kerogen swells more in the presence of methane than carbon dioxide per mole of sorbed gas. Scenario (d) could represent a field situation when a limited amount of carbon dioxide (roughly equal to or less than the gas-in-place) is

injected into a shale formation. In scenario (d), three quarters of the methane in scenario (b) has been replaced by equal moles of carbon dioxide. The final equilibrium state in scenario (d) represents in-situ kerogen with carbon dioxide and methane in 3:1 molar ratio. There was net volumetric shrinkage of the kerogen from scenario (b) to scenario (d). Therefore, if a volume of carbon dioxide – equal to or less than the gas-in-place (GIP) – is injected during a carbon dioxide enhanced gas recovery operation, there would possibly be a net shrinkage experienced by the kerogen. This is because kerogen primarily would shrink when part of the methane is replaced by an equal number of moles of carbon dioxide (going from scenario (b) to scenario (d)). However, if excess carbon dioxide is injected, the kerogen may swell leading to consequences such as permeability reduction, as seen in coalbed methane reservoirs. Also, the low permeability of shales should be considered during controlled CO2 injection. Due to low permeability to gases, shales may witness excess CO2 at the site of injection which may swell the kerogen. Kerogen shrinkage during enhanced gas recovery through controlled carbon dioxide injection would be smaller than the shrinkage in kerogen during the regular methane production by desorbing the gas. However, in the latter case, there would not be enhanced gas recovery by the process of exchange of sorbed methane with carbon dioxide. The volumetric strain was calculated for each of the scenarios and is tabulated in Table 5.2. Kerogen shrinkage or swelling may change the fluid pathways at the kerogen-mineral-grain boundaries. This will increase the permeability of the formation. This will also change the effective drainage volume available in the shale rocks. Higher permeability and effective drainage area is required for better recovery from shales.

The diffusion coefficients of each gas in the kerogen were calculated to investigate

preferential retention in kerogen. These are tabulated for each scenario in Table 5.2. Table 5.2 shows that the diffusion coefficient of methane in kerogen (scenario b) is an order of magnitude higher than for carbon dioxide (scenario c). In scenario (d), similar results were obtained, indicating that the interdiffusion coefficients of carbon dioxide and methane in kerogen are largely unaffected by each other. Slower diffusion of carbon dioxide in kerogen than methane indicates that carbon dioxide is strongly retained in the kerogen matrix. The methane diffusion coefficients match well with the methane diffusion coefficient determined by Ho et al. (2016)[115] who used the same Ungerer et al. (2015) kerogen model and a force field that is different from the force fields used by Ungerer and in this study.

## 5.6 Conclusions

Molecular dynamics simulations of carbon dioxide/methane/kerogen systems were performed with the objective of gaining a better understanding of the consequences of carbon dioxide injection into gas-bearing organic-rich shales. The higher adsorption capacity of kerogen for carbon dioxide than methane is well known. The MD simulations demonstrated that methane and carbon dioxide sorb in the matrix of kerogen and this increases (swells) its volume. However, the sorption of carbon dioxide will swell the kerogen to a lesser extent than swelling induced by sorption of an equal number of moles of methane. The MD simulations revealed that the sorbed carbon dioxide is more strongly retained by the medium maturity type II kerogen than is methane – at least under the reservoir temperature and pressure conditions. This preferential retention of carbon dioxide promotes its sequestration in shale gas reservoirs. Swelling in methane-poor reservoirs may impede permeability. Therefore, in the process of enhanced gas recovery

through carbon dioxide sequestration, the kerogen matrix may shrink if the injected carbon dioxide volume is roughly equal to or less than the gas-in-place (GIP). In such a case, operators may not worry about implications of swelling when pumping carbon dioxide into the shale reservoirs. The change in kerogen volume affects fluid flow pathways at the interface of kerogen and minerals. Net kerogen shrinkage in the case of controlled injection of carbon dioxide may open new fluid pathways at the kerogen-mineral-grain boundary and increase permeability that may lead to an improved recovery from shales. Interaction of carbon dioxide with the mineral matrix (parts of shales other than kerogen) and associated volumetric changes in the mineral matrix in presence of carbon dioxide should be studied to complete the full picture of carbon dioxide interaction with shales.

Table 5.1: Volumetric swelling of kerogen in the presence of carbon dioxide and methane at 300 atmospheres and 400 K. Kerogen swells more with methane than carbon dioxide on a per mole basis.

| System (scenario) | Final volume after annealing ($nm^3$) | $Q_v$ ($=\frac{swollen\ volume}{orignal\ volume}$) | Volumetric strain ($\Delta V/V$) w.r.t. scenario (a) |
|---|---|---|---|
| Pure kerogen (scenario a) | 76.71 | 1 | - |
| Kerogen with methane (scenario b) | 134.04 | 1.74 | 0.74 |
| Kerogen with carbon dioxide (scenario c) | 118.32 | 1.54 | 0.54 |
| Kerogen with methane & carbon dioxide (scenario d) | 118.75 | 1.54 | 0.54 |

Table 5.2: Interdiffusion carbon dioxide and methane coefficients in the swollen kerogen matrix. The methane diffusion coefficients molecules are an order of magnitude higher than the diffusion coefficients for the carbon dioxide molecules.

| System (scenario) | $D_{CO_2}$($m^2/s$) | $D_{CH_4}$($m^2/s$) |
|---|---|---|
| Kerogen with methane (scenario b) | - | $2*10^{-9}$ |
| Kerogen with carbon dioxide (scenario c) | $5*10^{-10}$ | - |
| Kerogen with methane & carbon dioxide (scenario d) | $7*10^{-10}$ | $2*10^{-9}$ |

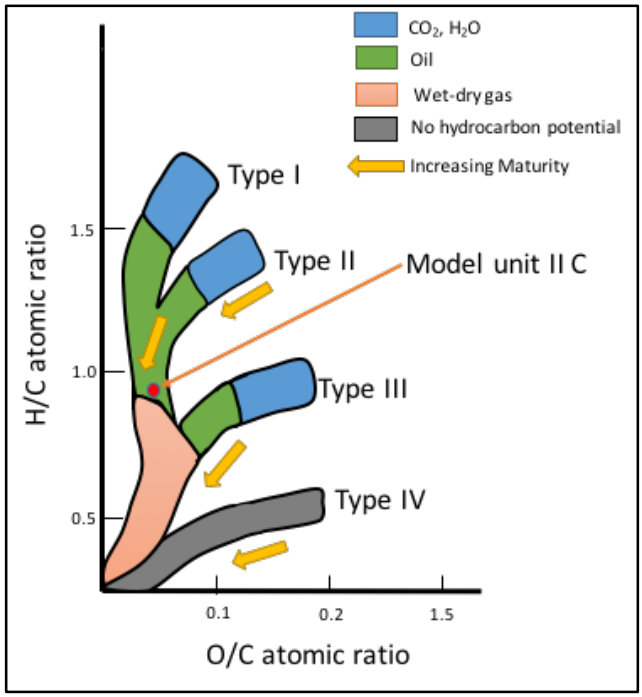


Figure 5.1. A Van Krevelen diagram, modified from McCarthy et al. (2011). Types I, II and III kerogen can generate oil and gas, and as they do, the maturity, which is often indicated by the atomic ratios of hydrogen to carbon (H/C) and oxygen to carbon (O/C), increase. Type IV kerogen, which is formed from charred organic matter and soot, has a high polyaromatic content. It produces no oil, but it may produce natural gas with a low yield. The model unit used for molecular dynamic simulations is shown by the red dot.

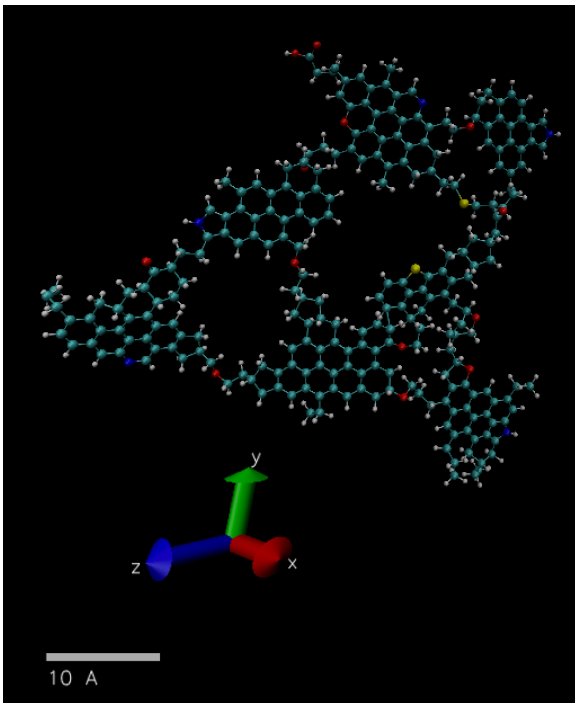


Figure 5.2. Molecular model of a single molecule of type II kerogen with medium to high maturity. The chemical formula of kerogen in this model is $C_{242}H_{219}O_{13}N_5S_2$. The model was developed by Ungerer et al. (2015). In this model, the carbon, hydrogen, oxygen, nitrogen, and sulfur atoms are represented in green, white, red, blue, and yellow colors.

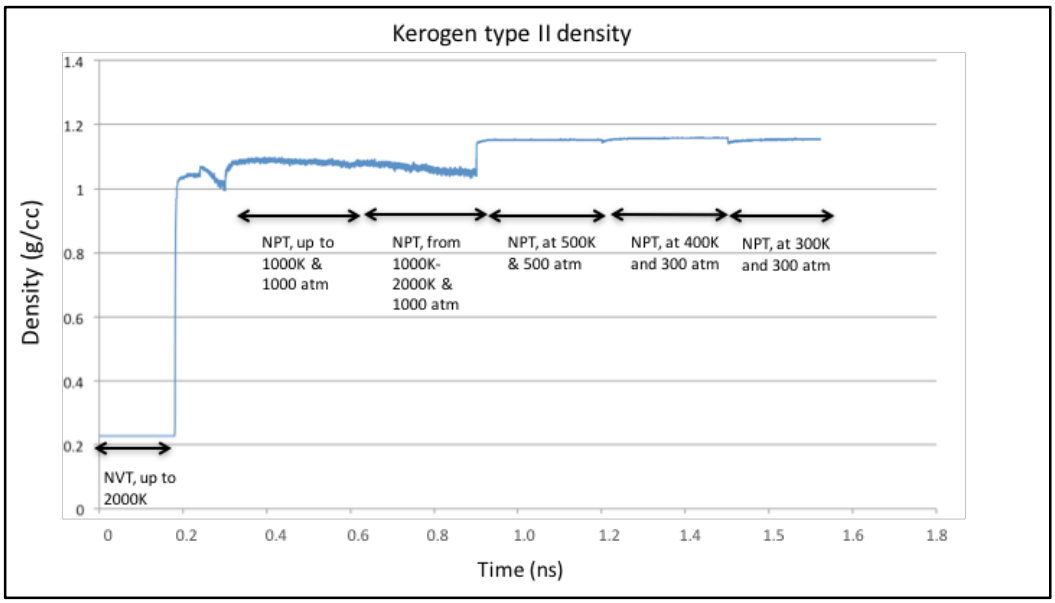


Figure 5.3. The variation in the density of the kerogen during simulated annealing. The density of the final annealed kerogen was 1.18g/cc.

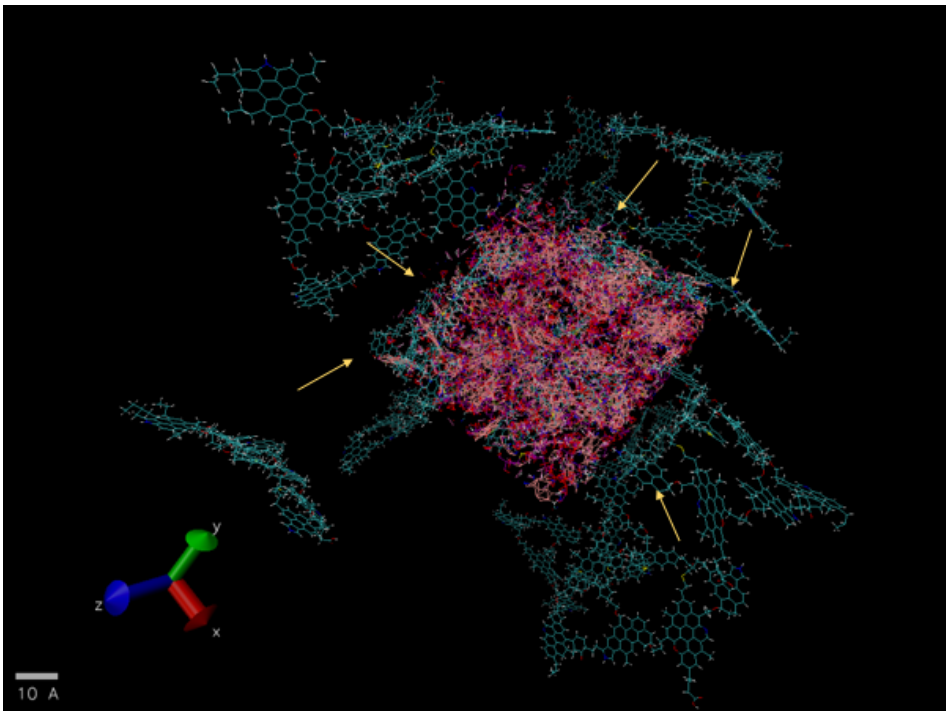


Figure 5.4: The configurations of kerogen molecules before and after simulated annealing to a temperature of 300K and a pressure of 300 atmospheres. The initial density (0.22 g/cc) of the system (with molecules in green) was increased to a final density of 1.18 g/cc (system with molecules in pink) as the system condenses (shown by the yellow arrows) at the end of simulated annealing. The simulated annealing brings the kerogen to a quasi-minimum free energy state without chemical alteration. Simulations of the sorption of methane and carbon dioxide were conducted at 400 K and 300 atmospheres using this molecular configuration of kerogen as the initial state.

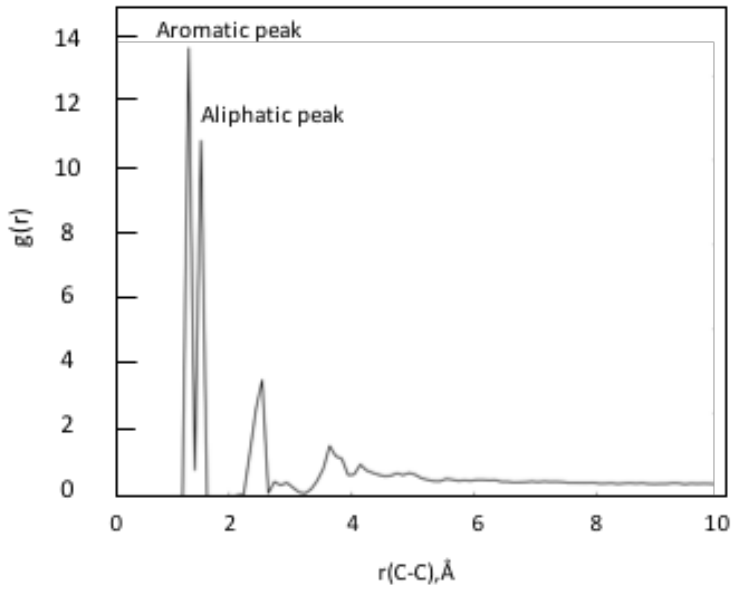


Figure 5.5: The radial pair distribution function of the simulated kerogen at a temperature of 300 K and a pressure of 300 atmospheres.

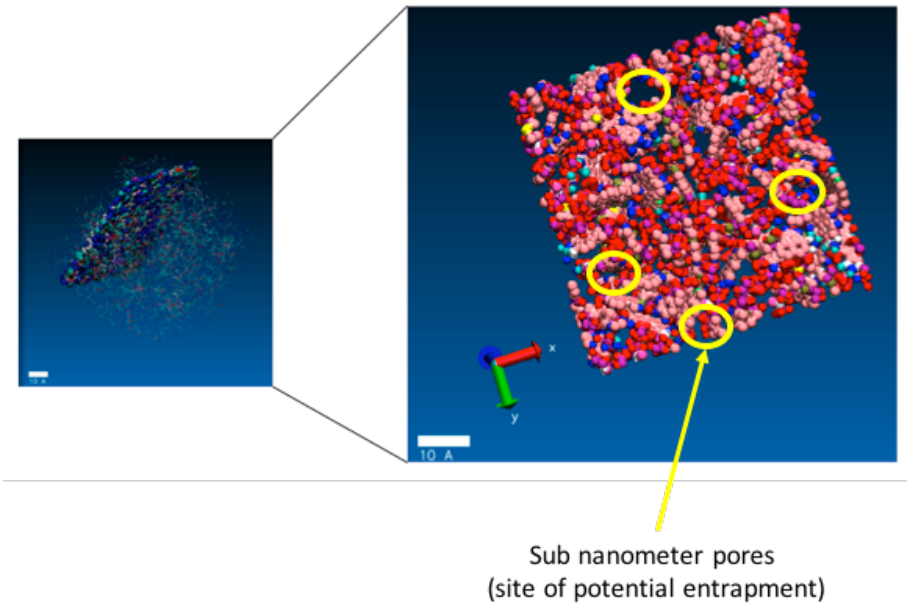


Figure 5.6: Planar thin sections of the kerogen model reveal sub-nanometer scale pores. Such pores are difficult to visualize through electron microscopy. These pores can become potential sites for entrapment of CO2 for the purpose of sequestration.

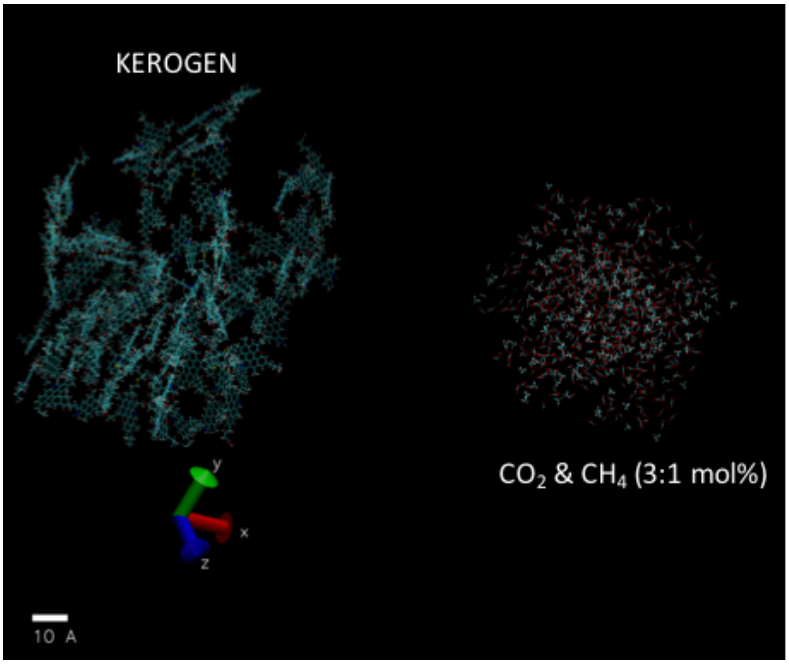


Figure 5.7: Initial configuration of kerogen and gas molecules. Initially the gas molecules were placed outside of the kerogen matrix. The gases may adsorb or absorb based on the interaction of each molecule with kerogen. The gas reservoir on the right contains both $CO_2$ and $CH_4$ molecules in red and green, respectively. The $CO_2$ and $CH_4$ molecules are in a 3:1 ratio with a total of 750 molecules.

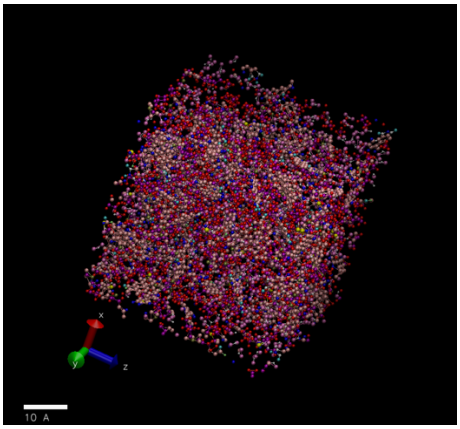


Figure 5.8: Final configuration of kerogen and gas molecules ($CO_2$ and $CH_4$). The gas molecules that were originally outside but in contact with the kerogen matrix have been sorbed in the kerogen matrix. The atoms H, O, N, C, S are shown in white, red, blue, cyan, and yellow in the molecular model.

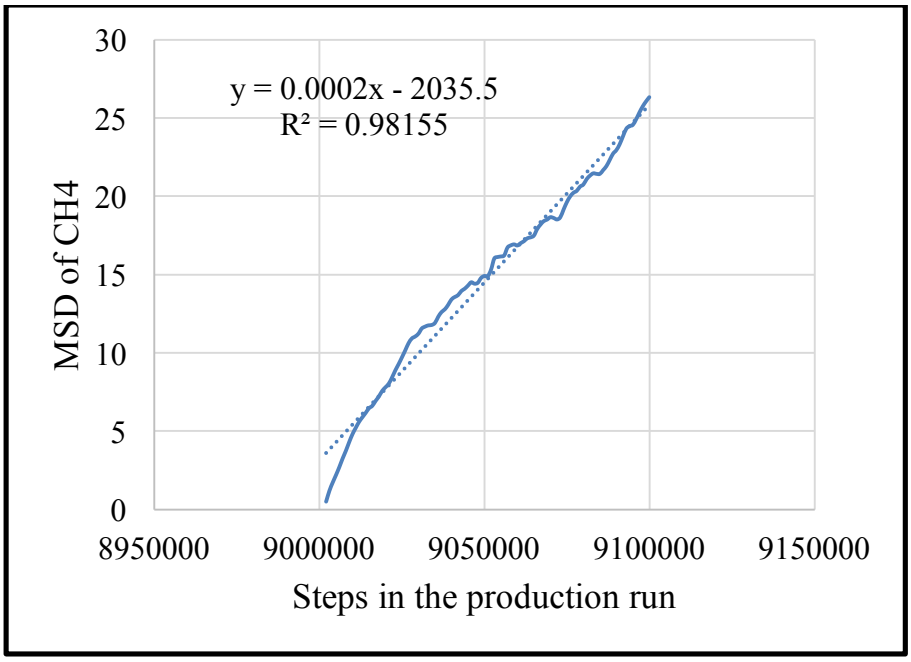


Figure 5.9: Plot of mean square displacement (MSD) in ($Angstroms^2$) versus time for methane starting at t = 9,000,000 time steps and ending at 9,100,000. The time is in units of molecular dynamics simulation time steps. The slope of the mean square displacement versus time relationship is the diffusion coefficient.

# CHAPTER 6

# CONCLUSIONS

Over the last decade or so, shales have played a key role in increasing oil and gas production in the United States. Shales contain organic matter known as kerogen. The dimensions of pores in shales holding hydrocarbons are believed to be on the order of nano meters. The fluids present in such small nanopores have different properties from those measured in bulk. Kerogen behaves as crosslinked polymer and preferentially absorbs different components of oil and swells in volume. Fluid saturation pressures at given temperatures – bubble points for oils and dew points for condensates in the nanopores, are affected by the pore walls in the vicinity of the fluid molecules and by the swelling behavior of the kerogen. In this dissertation, the effects of kerogen swelling and confinement of hydrocarbon fluids on bubble points of hydrocarbon liquids were studied using modeling and experimental techniques. The numerical representations included Molecular Dynamics simulations, and Gibbs Ensemble Monte Carlo simulations, Thermogravimetric analysis, and Differential Scanning Calorimetry were used in the experimental work. The experiments complimented the modeling results and confirmed the effect of kerogen swelling and confinement on the thermodynamic properties of analog formation hydrocarbon fluids. An approach of using carbon dioxide enhanced recovery was proposed for gas-rich shales as carbon dioxide helps to get sorbed methane

gas out from the kerogen matrix in shale. This will increase the recovery of gas from the gas-rich shales.

## 6.1 Original Contributions

The following original contributions in this dissertation account for the presence of nanopores and kerogen in shales and their influence on the thermodynamic properties. These original contributions are also the conclusions of this dissertation.

1. **Effect of retained oil-free oil equilibrium on the bubble point of oil from shales**

   It was found that the bubble point pressure of Eagle Ford oil is suppressed in the subsurface because of presence of kerogen in shales. The kerogen absorbs oil and increases (swells) in volume. The absorbed/retained oil composition is different from the free oil that did not penetrate into the kerogen matrix. The composition of an in-situ oil (the sum of the retained and free oil phases) should be considered when calculating the PVT properties of oils in shales. Due to the absorption by kerogen, the bubble points of in-situ oils in an example Eagle Ford shale are lowered by as much as 4150 to 16350 kPa at 400 K. This reduction depends on the expulsion efficiency, and the type and maturity of the kerogen.

2. **Effect of confinement of hydrocarbons on thermodynamic properties of oils**

   Shale is a nanoporous medium. The confinement of hydrocarbon fluids in these nanopores changes the thermodynamic properties of these fluids. The Gibbs Ensemble Monte Carlo simulations indicated that the critical density and critical temperature of a 90:10 decane-methane mixture were suppressed when confined in a 3.5 nm slit representing a nanopore.

3. **Experimental validation of the effect of kerogen and nanopores**

Experiments were designed using thermogravimetric analysis (TGA) and differential scanning calorimetry (DSC) to validate the effect of kerogen and nanopores (confinement) in shales. The bubble point temperature for decane and Clay Basin oil was reduced in the presence of kerogen and confinement. It was found that the presence of kerogen has a larger influence on the bubble point temperature than does confinement. The DSC experiments demonstrated a bubble point suppression of over $40^{o}$C when the oil was absorbed in kerogen. This suppression includes the effect of confinement and the effect of kerogen swelling (splitting of phase by absorbing oil components selectively).

4. **Carbon dioxide as possible solution for increasing gas recovery through its sequestration**

Carbon dioxide may have value as an injection fluid by replacing absorbed methane in the kerogen matrix. The diffusion coefficients of carbon dioxide gas are an order of magnitude smaller than for methane gas in a particular kerogen matrix. Thus, carbon dioxide has a higher tendency for retention in the kerogen matrix than methane gas. This can favor limited carbon dioxide sequestration in shales. If the volume of the injected carbon dioxide is less than the gas-in-place (GIP) during an enhanced gas recovery operation, there could be a net shrinkage in kerogen. A net shrinkage of kerogen (matrix volume) in the case of controlled injection of carbon dioxide may open new fluid pathways at the kerogen – mineral-grain boundary that may lead to an improved recovery from shales.

## REFERENCES


1. Swindell, G. S. Eagle Ford Shale -An Early Look at Ultimate Recovery. in *SPE Annual Technical Conference and Exhibition* (2012).

2. van Krevelen, D. W. *COAL : typology, chemistry, physics, constitution.* (Elsevier, 1961).

3. Tissot, B. P. & Welte, D. H. *Petroleum Formation and Occurrence*. (Springer-Verlag, 1984)

4. Vandenbroucke, M. & Largeau, C. Kerogen origin, evolution and structure. *Org. Geochem.* **38,** 719–833 (2007).

5. Sandvik, E. I., Young, W. A. & Curry, D. J. Expulsion from hydrocarbon sources: the role of organic absorption. *Org. Geochem.* **19,** 77–87 (1992).

6. Ertas, D., Kelemen, S. R. & Halsey, T. C. Petroleum Expulsion Part 1. Theory of Kerogen Swelling in Multicomponent Solvents. (2006). doi:10.1021/EF058024K

7. Pathak, M., Deo, M. D., Panja, P. & Levey, R. A. The Effect of Kerogen-Hydrocarbons Interaction on the PVT Properties in Liquid Rich Shale Plays. in *SPE/CSUR Unconventional Resources Conference* (Society of Petroleum Engineers, 2015). doi:10.2118/175905-MS

8. Miknis, F. P., Turner, T. F., Berdan, G. L. & Conn, P. J. Formation of soluble products from thermal decomposition of Colorado and Kentucky oil shales. *Energy & Fuels* **1,** 477–483 (1987).

9. Curiale, J. A. & Curtis, J. B. Organic geochemical applications to the exploration for source-rock reservoirs - A review. *J. Unconv. Oil Gas Resour.* **13,** 1–31 (2016).

10. Larsen, J. W. & Li, S. Changes in the Macromolecular Structure of a Type I Kerogen during Maturation. *Energy & Fuels* **11,** 897–901 (1997).

11. Larsen, J. W. & Li, S. Solvent Swelling Studies of Green River Kerogen. *Energy*

*& Fuels* **8,** 932–936 (1994).

12. Larsen, J. W. & Li, S. An initial comparison of the interactions of Type I and III kerogens with organic liquids. *Org. Geochem.* **26,** 305–309 (1997).

13. Hruljova, J., Savest, N., Oja, V. & Suuberg, E. M. Kukersite oil shale kerogen solvent swelling in binary mixtures. *Fuel* **105,** 77–82 (2013).

14. Ballice, L. Solvent swelling studies of Göynük (Kerogen Type-I) and Beypazarı oil shales (Kerogen Type-II). *Fuel* **82,** 1317–1321 (2003).

15. Savest, N., Oja, V., Kaevand, T. & Lille, Ü. Interaction of Estonian kukersite with organic solvents: A volumetric swelling and molecular simulation study. *Fuel* **86,** 17–21 (2007).

16. Ungerer, P., Collell, J. & Yiannourakou, M. Molecular Modeling of the Volumetric and Thermodynamic Properties of Kerogen: Influence of Organic Type and Maturity. *Energy & Fuels* **29,** 91–105 (2015).

17. Wang, J., Wolf, R. M., Caldwell, J. W., Kollman, P. A. & Case, D. A. Development and testing of a general amber force field. *J. Comput. Chem.* **25,** 1157–74 (2004).

18. Kelemen, S. R. *et al.* Direct Characterization of Kerogen by X-ray and Solid-State 13C Nuclear Magnetic Resonance Methods. *Energy & Fuels* **21,** 1548–1561 (2007).

19. Martínez, L., Andrade, R., Birgin, E. G. & Martínez, J. M. Packmol: A Package for Building Initial Configurations for Molecular Dynamics Simulations. (2009). doi:10.1002/jcc.21224

20. Humphrey, W., Dalke, A. & Schulten, K. VMD: visual molecular dynamics. *J. Mol. Graph.* **14,** 33–8, 27–8 (1996).

21. Plimpton, S. Fast Parallel Algorithms for Short-Range Molecular Dynamics. *J. Comput. Phys.* **117,** 1–19 (1995).

22. Okiongbo, K. S., Aplin, A. C. & Larter, S. R. Changes in Type II Kerogen Density as a Function of Maturity: Evidence from the Kimmeridge Clay Formation. *Energy & Fuels* **19,** 2495–2499 (2005).

23. Flory, P. J. *Principles of polymer chemistry.* (Cornell University Press, 1953).

24. Robinson, D. B. & Peng, D.-Y. *The characterization of the heptanes and heavier fractions for the GPA Peng-Robinson programs*. (Gas Processors Association, 1978).

25. Walters, C. C., Freund, H., Kelemen, S. R., Ertas, M. D. & Symington, W. Method for Predicting Petroleum Expulsion. (2013).

26. Whitson, C. H. & Sunjerga, S. PVT in Liquid-Rich Shale Reservoirs. in *SPE Annual Technical Conference and Exhibition* (Society of Petroleum Engineers, 2012). doi:10.2118/155499-MS

27. Lee, B. I. & Kesler, M. G. Generalized thermodynamic correlation based on three-parameter corresponding states. *AIChE J.* **21,** 510–527 (1975).

28. Di Primio, R., Dieckmann, V. & Mills, N. PVT and phase behaviour analysis in petroleum exploration. *Org. Geochem.* **29,** 207–222 (1998).

29. Romero, M. A. Subsurface and Outcrop Organic Geochemistry of the Eagle Ford Shale (Cenomanian-Coniacian) in West, Southwest, Central, and East Texas. (University of Oklahoma, 2014).

30. Pathak, M., Deo, M., Craig, J. & Levey, R. Geologic Controls on Production of Shale Play Resources: Case of Eagle Ford, Bakken and Niobrara. in *Proceedings of the 2nd Unconventional Resources Technology Conference* (American Association of Petroleum Geologists, 2014). doi:10.15530/urtec-2014-1922781

31. Hackley, P. C. & Cardott, B. J. Application of organic petrography in North American shale petroleum systems: A review. *Int. J. Coal Geol.* **163,** 8–51 (2016).

32. Edman, J. D. & Pitman, J. K. Geochemistry of Eagle Ford group source rocks and oils from the first shot field area, Texas. in *Gulf Coast Association of Geological Societies 60th Annual Convention* 217–234 (Gulf Coast Association of Geological Socities, 2010).

33. Cardneaux, A. P. Mapping of the Oil Window in the Eagle Ford Shale Play of Southwest Texas using Thermal Modeling and Log Overlay Analysis. (University of Mississippi, 2012). at <http://etd.lsu.edu/docs/available/etd-07112012-122340/unrestricted/Cardneaux_Thesis.pdf>

34. Ritter, U. Solubility of petroleum compounds in kerogen. *Org. Geochem.* **34,** 319–326 (2003).

35. Ritter, U. Fractionation of petroleum during expulsion from kerogen. *J. Geochemical Explor.* **78–79,** 417–420 (2003).

36. McCarthy, K. *et al.* Basic Petroleum Geochemistry for Source Rock Evaluation. *Oilf. Rev.* **23,** 32–43 (2011).

37. U.S. Energy Information. *Technically Recoverable Shale Oil and Shale Gas Resources : An Assessment of 137 Shale Formations in 41 Countries Outside the*

*United States*. *U.S. Energy Information Administration* (2013).

38. Brunauer, S., Emmett, P. H. & Teller, E. Adsorption of Gases in Multimolecular Layers. **407,** 309–319 (1936).

39. Barrett, P. E., Joyner, L. G. & Halenda, P. P. The Determination of Pore Volume and Area Distributions in Porous Substances. I. Computations from Nitrogen Isotherms. *J. Am. Chem. Soc.,* **73,** 373–380 (1951).

40. Oja, V., Yanchilin, A., Kan, T. & Strezov, V. Thermo-swelling behavior of Kukersite oil shale. *J. Therm. Anal. Calorim.* **119,** 1163–1169 (2014).

41. Hruljova, J., Savest, N., Yanchilin, A., Oja, V. & Suuberg, E. M. Solvent Swelling Of Kukersite Oil Shale Macromolecular Organic Matter In Binary Mixtures: Impact Of Specifically Interacting Solvents. *Oil Shale* **31,** 365–376 (2014).

42. Green, T. K., Kovac, J. & Larsen, J. W. A rapid and convenient method for measuring the swelling of coals by solvents. *Fuel* **63,** 935–938 (1984).

43. Larsen, J. W. & Flores, C. I. Kerogen chemistry 5. Anhydride formation in, solvent swelling of, and loss of organics on demineralization of Kimmeridge shales. *Fuel Process. Technol.* **89,** 314–321 (2008).

44. Pinto, F., Gulyurtlu, I., Lobo, L. S. & Cabrita, I. Effect of coal pre-treatment with swelling solvents on coal liquefaction. *Fuel* **78,** 629–634 (1999).

45. Sert, M. *et al.* Effect of solvent swelling on pyrolysis of kerogen (type-I) isolated from Göynük oil shale (Turkey). *J. Anal. Appl. Pyrolysis* **84,** 31–38 (2009).

46. SONG, L., XUE, H., LU, S. & TIAN, S. The Research Progress on the Occurrence Mechanism of Detained Hydrocarbon. *Acta Geol. Sin. - English Ed.* **89,** 164–165 (2015).

47. Raji, M., Gröcke, D. R., Greenwell, C. & Cornford, C. Pyrolysis, porosity and productivity in unconventional mudstone reservoirs: Free and Adsorbed Oil. in *3rd Unconventional Resources Technology Conference, San Antonio* (2015).

48. Pankaj, T. Oil Shale Pyrolysis: Benchscale Experimental Studies and Modeling. (University of Utah, 2012).

49. Daw, J. E. *Measurement of Specific Heat Capacity Using Differential Scanning Calorimeter*. *Idaho National Laboratory* (2008).

50. *ISO 11357-1:2016(en), Plastics — Differential scanning calorimetry (DSC) — Part 1: General principles*. (2016). at <https://www.iso.org/obp/ui/#iso:std:iso:11357:-1:ed-3:v1:en>

51. Höhne, G., Hemminger, W. F. & Flammersheim, H. J. *Differential Scanning Calorimetry*. (Springer Berlin Heidelberg, 2013). at <https://books.google.co.in/books?id=0mzmCAAAQBAJ>

52. Collell, J. *et al.* Molecular Simulation of Bulk Organic Matter in Type II Shales in the Middle of the Oil Formation Window. *Energy & Fuels* **28,** 7457–7466 (2014).

53. Jin, Z. & Firoozabadi, A. Flow of methane in shale nanopores at low and high pressure by molecular dynamics simulations. *J. Chem. Phys.* **143,** 104315 (2015).

54. Kilk, K. *et al.* SOLVENT SWELLING OF DICTYONEMA OIL SHALE. *Oil Shale* **27,** 26–36 (2010).

55. Zarragoicoechea, G. J. & Kuz, V. A. Critical shift of a confined fluid in a nanopore. *Fluid Phase Equilib.* **220,** 7–9 (2004).

56. Wu, Q. Investigation of fluids flow behavior in nano-scale channels by using optic imaging system. (2014).

57. Wang, L. *et al.* SPE 169581 Experimental Study and Modeling of the Effect of Nanoconfinement on Hydrocarbon Phase Behavior in Unconventional Reservoirs. in *SPE Western North American and Rocky Mountain Joint Regional Meeting* (2014). doi:10.2118/169581-MS

58. Singh, S. K., Sinha, A., Deo, G. & Singh, J. K. Vapor− liquid phase coexistence, critical properties, and surface tension of confined alkanes. *J. Phys. Chem. C* **113,** 7170–7180 (2009).

59. Sheng, L., Hadi, N. & Lutkenhaus, J. L. Effect of Confinement on the Bubble Points of Hydrocarbons in Nanoporous Media. *AIChE J.* **0,** (2016).

60. Pitakbunkate, T., Balbuena, P. B., Texas, a, Moridis, G. J. & National, L. B. Effect of Confinement on PVT Properties of Hydrocarbons in Shale. 1–16 (2014). doi:10.2118/170685-PA

61. Gelb, L. D., Gubbins, K. E., Radhakrishnan, R. & Sliwinska-Bartkowiak, M. Phase separation in confined systems. *Reports Prog. Phys.* **62,** 1573–1659 (1999).

62. Dong, X., Liu, H., Hou, J., Wu, K. & Chen, Z. Phase Equilibria of Confined Fluids in Nanopores of Tight and Shale Rocks Considering the Effect of Capillary Pressure and Adsorption Film. *Ind. Eng. Chem. Res.* **55,** 798–811 (2016).

63. Barsotti, E., Tan, S. P., Saraji, S., Piri, M. & Chen, J.-H. A review on capillary condensation in nanoporous media: Implications for hydrocarbon recovery from tight reservoirs. *Fuel* **184,** 344–361 (2016).

64. Carlson, T. Modeling van der Waals forces in graphite Structure of Graphene.

65. Jewett, A. I., Zhuang, Z. & Shea, J.-E. Moltemplate a Coarse-Grained Model Assembly Tool. *Biophys. J.* **104,** 169a (2013).

66. Gasteiger, J. & Marsili, M. Iterative partial equalization of orbital electronegativity—a rapid access to atomic charges. *Tetrahedron* **36,** 3219–3228 (1980).

67. Hanwell, M. D. *et al.* Avogadro: an advanced semantic chemical editor, visualization, and analysis platform. *J. Cheminform.* **4,** 17 (2012).

68. Case, D. A. *et al.* The Amber biomolecular simulation programs. *J. Comput. Chem.* **26,** 1668–1688 (2005).

69. Pathak, M., Deo, M., Craig, J. & Levey, R. Geologic Controls on Production of Shale Play Resources: Case of Eagle Ford, Bakken and Niobrara. in *Proceedings of the 2nd Unconventional Resources Technology Conference* (American Association of Petroleum Geologists, 2014). doi:10.15530/urtec-2014-1922781

70. Sheng, J. J. Enhanced oil recovery in shale reservoirs by gas injection. *J. Nat. Gas Sci. Eng.* **22,** 252–259 (2015).

71. Pathak, M., Deo, M. D., Panja, P. & Levey, R. A. The Effect of Kerogen-Hydrocarbons Interaction on the PVT Properties in Liquid Rich Shale Plays. in *SPE/CSUR Unconventional Resources Conference* (Society of Petroleum Engineers, 2015). doi:10.2118/175905-MS

72. Pathak, M., Pawar, G., Huang, H. & Deo, M. D. Carbon Dioxide Sequestration and Hydrocarbons Recovery in the Gas Rich Shales: An Insight from the Molecular Dynamics Simulations. in *Carbon Management Technology Conference* (Carbon Management Technology Conference, 2015). doi:10.7122/439481-MS

73. Nagarajan, N. R., Honarpour, M. M. & Arasteh, F. Critical Role of Rock and Fluid - Impact on Reservoir Performance on Unconventional Shale Reservoirs. in *Unconventional Resources Technology Conference, Denver, Colorado, 12-14 August 2013* 1905–1910 (Society of Exploration Geophysicists, American Association of Petroleum Geologists, Society of Petroleum Engineers, 2013). doi:10.1190/urtec2013-194

74. Devegowda, D., Sapmanee, K., Civan, F. & Sigal, R. Phase behavior of gas condensates in shales due to pore proximity effects: Implications for transport reserves and well productivity. *SPE Annu. Tech. Conf. Exhib.* 1–22 (2012). doi:10.2118/160099-MS

75. Haider, B. A. Impact of Capillary Pressure and Critical Properties Shift Due To

Confinement on Hydrocarbon Production. (Stanford University, 2015).

76. Ma, Y., Chen, J.-H. & Jamili, A. Adsorption and Capillary Condensation in Heterogeneous Nanoporous Shales. in *Unconventional Resources Technology Conference (URTeC)* (2016). doi:10.15530-urtec-2016-2432657

77. Firincioglu, T. Bubble point suppression in unconventional liquids rich reservoirs and its impact on oil production. (Colorado School of Mines).

78. Nagy, S. & Siemek, J. Confined Phase Envelope of Gas-Condensate Systems in Shale Rocks. *Arch. Min. Sci.* **59,** 1005–1022 (2014).

79. Jin, Z. & Firoozabadi, A. Thermodynamic Modeling of Phase Behavior in Shale Media. *Soc. Pet. Eng. J.* 190 (2016). doi:10.2118/176015-PA

80. Xiong, X., Devegowda, D., Civan, F. & Sigal, R. F. Compositional Modeling of Liquid-Rich Shales Considering Adsorption, Non-Darcy Flow Effects and Pore Proximity Effects on Phase Behavior. in *Unconventional Resources Technology Conference (URTeC)* (Society of Petroleum Engineers (SPE) , 2013).

81. Panagiotopoulos, A. Z. Adsorption and capillary condensation of fluids in cylindrical pores by Monte Carlo simulation in the Gibbs ensemble. *Mol. Phys.* **62,** 701–719 (1987).

82. Panagiotopoulos, A. Z. Direct Determination of Fluid-Phase Equilibria by Simulation in the Gibbs Ensemble - a Review. *Mol. Simul.* **9,** 1–23 (1992).

83. Sliwinska-Bartkowiak, M. *et al.* Phase Transitions in Pores: Experimental and Simulation Studies of Melting and Freezing. *Langmuir* **15,** 6060–6069 (1999).

84. Lastoskie, C., Gubbins, K. E. & Quirke, N. Pore size heterogeneity and the carbon slit pore: a density functional theory model. *Langmuir* **9,** 2693–2702 (1993).

85. Jones, J. E. On the Determination of Molecular Fields. II. From the Equation of State of a Gas. *Proc. R. Soc. A Math. Phys. Eng. Sci.* **106,** 463–477 (1924).

86. Berthelot D. C. R. No Title. *Hebd. Seanc. Acad. Sci., Paris* **126,** 1703. (1898).

87. Lorentz, H. A. Ueber die Anwendung des Satzes vom Virial in der kinetischen Theorie der Gase. *Ann. Phys.* **248,** 127–136 (1881).

88. Steele, W. A. The physical interaction of gases with crystalline solids. *Surf. Sci.* **36,** 317–352 (1973).

89. Steele, W. A. *The interaction of gases with solid surfaces*. (Pergamon Press, 1974). at

<https://books.google.com/books/about/The_interaction_of_gases_with_solid_surf.html?id=9BROAQAAIAAJ>

90. Martin, M. G. & Siepmann, J. I. Transferable Potentials for Phase Equilibria. 1. United-Atom Description of n-Alkanes. *J. Phys. Chem. B 1998,* **102,** 2569–2577 (1998).

91. Singh, S. K., Saha, A. K. & Singh, J. K. Molecular Simulation Study of Vapor−Liquid Critical Properties of a Simple Fluid in Attractive Slit Pores: Crossover from 3D to 2D. *J. Phys. Chem. B* **114,** 4283–4292 (2010).

92. Antoine, C. Tensions des vapeurs: nouvelle relation entre les tensions et les temperatures. Tensions de diverses vapeurs. *Compt. Rend.* **107,** 681–684 (1888).

93. Thomson, G. W. The Antoine Equation for Vapor-pressure Data. *Chem. Rev.* **38,** 1–39 (1946).

94. Poling, B. E., Prausnitz, J. M. & O'Connell, J. P. *The Properties of Gases and Liquids*. (McGraw-Hill Education). at <https://www.amazon.com/Properties-Gases-Liquids-Bruce-Poling/dp/0070116822>

95. Shale in the Unites States. (2016). at <https://www.eia.gov/energy_in_brief/article/shale_in_the_united_states.cfm>

96. Etminan, S. R., Javadpour, F., Maini, B. B. & Chen, Z. Measurement of gas storage processes in shale and of the molecular diffusion coefficient in kerogen. *Int. J. Coal Geol.* **123,** 10–19 (2014).

97. Chandler, D. L. Realistic molecular model of kerogen's nanostructure. (2016). at <http://phys.org/news/2016-02-nanopores-oil-gas-kerogen.html>

98. Al-Hasami, A., Ren, S. & Tohidi, B. CO2 Injection for Enhanced Gas Recovery and Geo-Storage: Reservoir Simulation and Economics. in *SPE Europec/EAGE Annual Conference* (Society of Petroleum Engineers, 2005). doi:10.2118/94129-MS

99. Jikich, S. A., Smith, D. H., Sams, W. N. & Bromhal, G. S. Enhanced Gas Recovery (EGR) with Carbon Dioxide Sequestration: A Simulation Study of Effects of Injection Strategy and Operational Parameters. in *SPE Eastern Regional Meeting* (Society of Petroleum Engineers, 2003). doi:10.2118/84813-MS

100. Khan, C., Amin, R. & Madden, G. Effects of CO2 and acid gas injection on enhanced gas recovery and storage. *J. Pet. Explor. Prod. Technol.* **3,** 55–60 (2013).

101. Khan, C., Amin, R. & Madden, G. Carbon dioxide injection for enhanced gas recovery and storage (reservoir simulation). *Egypt. J. Pet.* **22,** 225–240 (2013).

102. Oldenburg, C. M. & Benson, S. M. CO2 Injection for Enhanced Gas Production and Carbon Sequestration. in *SPE International Petroleum Conference and Exhibition* (Society of Petroleum Engineers, 2002).

103. Pathak, M., Panja, P., Huang, H. & Deo, M. Enhanced Recovery in Shales: Molecular Investigation of $CO_2$ Energized Fluid for Re-Fracturing Shale Formations. in *Unconventional Resources Technology Conferenc* (Unconventional Resources Technology Conference, 2016).

104. Burke, L. H., Nevison, G. W. & Peters, W. E. Improved Unconventional Gas Recovery With Energized Fracturing Fluids: Montney Example. in *SPE Eastern Regional Meeting* (Society of Petroleum Engineers, 2011). doi:10.2118/149344-MS

105. Reynolds, M., Bachman, R., Buendia, J. & Peters, W. The Full Montney - A Critical Review of Well Performance by Production Analysis of Over 2,000 Montney Multi-Stage Fractured Horizontal Gas Wells. in *SPE/CSUR Unconventional Resources Conference* (Society of Petroleum Engineers, 2015). doi:10.2118/175948-MS

106. Eshkalak, M. O., Al-shalabi, E. W., Sanaei, A. & Aybar, U. Journal of Natural Gas Science and Engineering Simulation study on the CO 2 -driven enhanced gas recovery with sequestration versus the re-fracturing treatment of horizontal wells in the U . S . unconventional shale reservoirs. *J. Nat. Gas Sci. Eng.* **21,** 1015–1024 (2014).

107. Charoensuppanimit, P., Mohammad, S. A. & Gasem, K. A. M. Measurements and Modeling of Gas Adsorption on Shales. *Energy & Fuels* **30,** 2309–2319 (2016).

108. Heller, R. & Zoback, M. Adsorption of methane and carbon dioxide on gas shale and pure mineral samples. *J. Unconv. OIL GAS Resour.* **8,** 14–24 (2014).

109. Kowalczyk, P., Furmaniak, S., Gauden, P. A. & Terzyk, A. P. Carbon Dioxide Adsorption-Induced Deformation of Microporous Carbons. *J. Phys. Chem. C* **114,** 5126–5133 (2010).

110. Yang, S., Wu, W., Xu, J., Ji, D. & Chen, Z. Volume Effects on Methane-Shale Adsorption under Reservoir Conditions. in *SPE EUROPEC/EAGE, 78th EAGE Conference and Exhibition* (Society of Petroleum Engineers, 2016).

111. Stankiewicz, B. A., Kruge, M. A., Crelling, J. C. & Salmon, G. L. Density Gradient Centrifugation: Application to the Separation of Macerals of Type I, II, and III Sedimentary Organic Matter. *Energy & Fuels* **8,** 1513–1521 (1994).

112. Bousige, C. *et al.* Realistic molecular model of kerogen's nanostructure. *Nat. Mater.* **15,** 576–582 (2016).

113. Nyahay, R., Leone, J., Smith, L. B., Martin, J. P. & Jarvie, D. J. Update on Regional Assessment of Gas Potential in the Devonian Marcellus and Ordovician Utica Shales of New York. in *AAPG Eastern Section Meeting* (AAPG Search and Discovery Article #10136, 2007). at <http://www.searchanddiscovery.com/documents/2007/07101nyahay/index.htm?q=%25252Btex>

114. Nykky, A. Pores, porosity and pore size distribution of some Draupne Formation and Colorado Group shales and kerogens. (Newcastle University, 2014). at <https://theses.ncl.ac.uk/dspace/handle/10443/2418>

115. Ho, T. A., Criscenti, L. J. & Wang, Y. Nanostructural control of methane release in kerogen and its implications to wellbore production decline. *Sci. Rep.* **6,** 28053 (2016).